

FINITE ELEMENT MODELING OF REINFORCED CONCRETE
STRUCTURAL WALLS

by

Muhammet Fethi Güllü

B.S., Civil Engineering, Istanbul Technical University, 2009

Submitted to the Institute for Graduate Studies in
Science and Engineering in partial fulfillment of
the requirements for the degree of
Master of Science

Graduate Program in Civil Engineering

Boğaziçi University

2013

FINITE ELEMENT MODELING OF REINFORCED CONCRETE
STRUCTURAL WALLS

APPROVED BY:

Assist. Prof. Kutay Orakçal
(Thesis Supervisor)

Assist. Prof. C. Can Aydıner

Assist. Prof. Serdar Selamet

DATE OF APPROVAL: 21.08.2013

To my family,

ACKNOWLEDGEMENTS

I would like to express my sincere gratitude to my thesis supervisor Assistant Prof. Kutay Orakçal for his invaluable guidance and help during the preparation of this thesis. I would like to acknowledge his patience and his positive approach during the impasse moments of my studies.

I would like to express my special thanks to my colleague Arif Emir Örendil for his help on preparation of the model code.

I would also like to express my thanks to my colleague Tarık Tufan for his support during the preparation of this thesis.

Most of all, I would like to express my special thanks to my parents for the endless support and encouragement they have given me throughout my whole life.

ABSTRACT

FINITE ELEMENT MODELING OF REINFORCED CONCRETE STRUCTURAL WALLS

This study was conducted to propose a two dimensional finite element model to obtain the inelastic response of reinforced concrete (RC) structural walls under generalized reversed-cyclic, in-plane loading conditions. The proposed model in this study incorporates a fixed crack angle modeling approach, which is suitable for reversed cyclic loading conditions and a feasible candidate for two dimensional finite element modeling methodology. The main purpose of this study is to capture a reasonable prediction of unexpected shear yielding and nonlinear shear deformations in slender walls. The analytical model was shown to capture, with reasonable accuracy, overall behavioral attributes of RC structural walls, including cyclic lateral load versus shear distortion, lateral stiffness, strength and ductility. Nonlinear force-deformation response of the analytical model also represents cyclic response properties; including stiffness degradation, plastic (residual) displacements, and pinching behavior. The proposed finite element model was implemented into Matlab and analyses were performed using a drift-controlled nonlinear analysis solution strategy. Comparison of the analytical and experimental model results was conducted and reasonably well results were obtained for slender walls. For checking the sensitivity of the analytical model results to modeling parameters, parametric sensitivity studies were conducted. Modeling parameters related to the number of model elements, axial force level, web reinforcement ratio and wall slenderness ratio were changed to demonstrate the sensitivity of the proposed model to important response parameters.

ÖZET

BETONARME PERDE DUVARLARIN SONLU ELEMENLAR İLE MODELLEMESİ

Bu çalışmanın amacı, betonarme perde duvarların düzlem içi tersinir tekrarlanır yükler altında doğrusal olmayan davranışını elde etmeyi hedefleyen iki boyutlu bir sonlu eleman modeli sunmaktır. Bu çalışmada sunulan model, tersinir tekrarlanır yük koşullarına uyumlu olan ve iki boyutlu sonlu eleman modellemesi için uygun bir seçenek olan sabit çatlak açısı modelleme yaklaşımını içermektedir. Bu çalışmadaki asıl amaç narin perdelerin beklenmeyen kesme akması ve doğrusal olmayan kayma deformasyonu için deneysel gözlemlerle uyumlu sonuçlara ulaşmaktır. Analitik modelin, tekrarlanır yanal yükler altında doğrusal olmayan kesme davranışı, yanal rijitlik, dayanım ve süneklik gibi önemli davranışsal özellikleri makul hassasiyetle temsil edebildiği görülmüştür. Analitik modelin doğrusal olmayan yük-deplasman davranış tahminlerinde rijitlik kaybı, plastik (kalıcı) deplasman, ve daralma gibi davranış unsurları da gözlemlenebilmiştir. Sunulan sonlu eleman modelinin formülasyonu Matlab ortamında kodlanmış, deplasman kontrollü bir doğrusal olmayan çözüm stratejisi kullanılarak analizler yürütülmüştür. Narin perdeler için analitik model sonuçları deneysel sonuçlarla karşılaştırılmış, davranış tahminlerinde makul doğruluk payı içeren sonuçlara ulaşılmıştır. Analitik model sonuçlarının önemli modelleme parametrelerine duyarlılığını ölçmek için ayrıca parametrik analizler yapılmış, model sonuçlarının kullanılan eleman sayısı, eksenel yük seviyesi, gövde donatı oranı ve perde narinlik oranı gibi önemli davranış parametreleri ile değişimi incelenmiştir.

TABLE OF CONTENTS

ACKNOWLEDGEMENTS.....	iv
ABSTRACT.....	v
ÖZET	vi
TABLE OF CONTENTS.....	vii
LIST OF FIGURES	ix
LIST OF TABLES.....	xv
LIST OF SYMBOLS.....	xvi
LIST OF ACRONYMS/ABBREVIATIONS	xix
1. INTRODUCTION	1
1.1. General.....	1
1.2. Literature Review	2
1.2.1. Flexural Modeling	2
1.2.2. Constitutive Modeling of RC Panel Behavior for Finite Element Modeling.....	7
1.2.3. Modeling of Shear-Flexure Interaction in RC Walls	10
1.2.4. Experimental Studies on Shear-Flexure Interaction in RC Walls	12
1.3. Research Significance.....	13
1.4. Objectives and Scope.....	14
1.5. Thesis Outline.....	14
2. CONSTITUTIVE MODEL DESCRIPTION.....	16
2.1. Overview	16
2.2. Panel Model.....	17
2.3. Material Constitutive Models	20

2.3.1.	Constitutive Model for Reinforcement.....	20
2.3.2.	Constitutive Model for Concrete	21
2.3.3.	Compression Softening of Concrete.....	22
2.3.4.	Tension Stiffening Effect on Concrete and Reinforcing Steel	22
2.3.5.	Biaxial Damage on Concrete.....	23
2.3.6.	Shear Aggregate Interlock.....	23
3.	FINITE ELEMENT MODEL DESCRIPTION	26
3.1.	4 Nodes, 8 Degree of Freedom Rectangular Element (Mesh).....	26
3.2.	Finite Element Model Stiffness Assembly	31
3.3.	Internal Force Vector Assembly	34
3.4.	Support Conditions and Constraints	37
3.5.	Nonlinear Analysis Solution Strategy	40
4.	EXPERIMENTAL CALIBRATION AND VALIDATION OF THE MODEL	45
4.1.	Description of Experimental Program	45
4.2.	Model Calibration.....	54
4.3.	Model Results and Comparison with Experimental Results of Specimen RW2	58
4.4.	Parametric Sensitivity Studies	68
4.5.	Discussion of Results.....	75
5.	SUMMARY AND CONCLUSIONS	77
5.1.	Overview	77
5.2.	Conclusions	78
5.3.	Recommendations for Future Studies.....	79
	REFERENCES	81

LIST OF FIGURES

Figure 1.1. Three-Vertical-Line-Element Model (TVLEM) (Kabeyasawa <i>et al.</i> , 1983).	3
Figure 1.2. Axial-Element-in-Series Model (AESM) (Vulcano and Bertero, 1986).....	4
Figure 1.3. Multiple-Vertical-Line-Element Model (MVLEM) (Vulcano <i>et al.</i> , 1988).	5
Figure 1.4. Modification of the TVLEM to PWME (Kabeyasawa <i>et al.</i> , 1997).	6
Figure 1.5. MVLEM (Orakcal <i>et al.</i> , 2004).	7
Figure 2.1. Uncracked behavior of concrete in the Fixed Strut Angle Model (Orakcal <i>et al.</i> , 2012).....	18
Figure 2.2. Behavior of concrete after formation of first crack in the Fixed Strut Angle Model (Orakcal <i>et al.</i> , 2012).	19
Figure 2.3. Behavior of concrete after formation of second crack in the Fixed Strut Angle Model (Orakcal <i>et al.</i> , 2012).	20
Figure 2.4. Hysteretic constitutive model for reinforcing steel (Menegotto and Pinto, 1973).....	20
Figure 2.5. Hysteretic constitutive model for concrete (Chang and Mander, 1994).	21

Figure 2.6. Compression softening effects implemented in the panel model (Ulugtekin, 2010).....	22
Figure 2.7. Shear-friction mechanism along a crack (ACI-318M, 2008).	24
Figure 3.1. Local nodes and DOFs in a rectangular element.	27
Figure 3.2. Normalized coordinates of a rectangular element.	27
Figure 3.3. Tangent stiffness (elasticity) matrix calculation path.....	29
Figure 3.4. Numbering of nodes and elements in a sample model.....	32
Figure 3.5. Superposition of stiffness matrixes.	32
Figure 3.6. Numbering technique used for the FEM of a rectangular wall.	33
Figure 3.7. Global and local DOFs in a structural wall model.	33
Figure 3.8. Stress vector calculation path.	34
Figure 3.9. Numeration of internal forces for a mesh.....	35
Figure 3.10. Superposition of internal force vectors.	36
Figure 3.11. Global and local DOFs in a structural wall model.	37
Figure 3.12. Support conditions in the FEM.	38

Figure 3.13. Conversion of DOFs after the assignment of body constraint.	38
Figure 3.14. Representation of the nonlinear analysis solution strategy for a single degree of freedom system (Clarke and Hancock, 1990).	44
Figure 3.15. Iterative strategy and residual displacements (Clarke and Hancock, 1990).	44
Figure 4.1. RC wall specimen tested by Thomsen and Wallace (1995).	46
Figure 4.2. Profile view of specimen RW2 showing placement of reinforcement (Thomsen and Wallace, 1995).	46
Figure 4.3. Cross-sectional view of the test specimen RW2 (Thomsen and Wallace, 1995).	47
Figure 4.4. Measured concrete stress-strain relationship for RW2 (Thomsen and Wallace, 1995).	48
Figure 4.5. Measured reinforcement stress-strain relationship for #3, #2 and 4.76 mm annealed wire (Thomsen and Wallace, 1995).	49
Figure 4.6. Schematic of the test setup (Thomsen and Wallace, 1995).	50
Figure 4.7. A photograph of the test setup (Thomsen and Wallace, 1995).	50
Figure 4.8. A photograph of load transfer assembly (Thomsen and Wallace, 1995). ...	51

Figure 4.9. Instrumentation on RW2.	52
Figure 4.10. A photograph of instrumentation used to measure pedestal movement (Thomsen and Wallace, 1995).	52
Figure 4.11. A photograph wire potentiometers used to measure shear deformations (Thomsen and Wallace, 1995).	53
Figure 4.12. Lateral drift history for specimen RW2.	53
Figure 4.13. Geometric calibration for specimen RW2.	54
Figure 4.14. Constitutive material model for reinforcing steel and parameters for calibration (Orakcal, 2004).	56
Figure 4.15. Constitutive material model for concrete and parameters for calibration (Orakcal, 2004).	56
Figure 4.16. Comparison of the confinement models.	57
Figure 4.17. Comparison of applied and corrected drift histories for specimen RW2. ..	59
Figure 4.18. Comparison of the measured and calculated lateral load vs. displacement responses for wall specimen RW2.	60
Figure 4.19. Comparison of the measured and predicted lateral displacement profiles..	61

Figure 4.20. Comparison of measured and predicted lateral displacement and rotation time histories at the first story level.	62
Figure 4.21. Comparison of the average concrete strain profiles along wall length at small drift levels.....	63
Figure 4.22. Comparison of the average concrete strain profiles along wall length at large drift levels.....	63
Figure 4.23. Comparison of the vertical strain histories at the north boundary of the wall at base level.	64
Figure 4.24. Comparison of the vertical strain histories at the south boundary of the wall at base level.	65
Figure 4.25. Comparison of measured and predicted lateral load vs. first story shear deformation responses.....	66
Figure 4.26. Comparison of measured and predicted lateral load vs. second story shear deformation responses.....	67
Figure 4.27. Comparison of analytical lateral load vs. story shear deformation responses.	68
Figure 4.28. Analytical lateral load vs. top displacement responses for different n values.	69

Figure 4.29. Analytical vertical strain histories at the boundary of the wall at base level for different n values.	70
Figure 4.30. Analytical lateral load vs. top displacement responses for different wall aspect ratios.	71
Figure 4.31. Analytical lateral load vs. top displacement responses for different wall aspect ratios.	71
Figure 4.32. Analytical lateral load vs. top displacement responses for different axial load levels.	72
Figure 4.33. Analytical lateral load vs. top displacement responses for different web reinforcement ratios.	73
Figure 4.34. Effect of web reinforcement ratio to shear deformations along first story.	74
Figure 4.35. Effect of web reinforcement ratio to shear deformations along second story.....	74

LIST OF TABLES

Table 4.1. Calibrated constitutive parameters for concrete.	57
Table 4.2. Calibrated constitutive parameter for reinforcing steel.	58
Table 4.3. Lateral displacement values at peak drift points for specimen RW2.	59

LIST OF SYMBOLS

a_1 and a_2	Experimentally determined parameters that represent the degradation of the curvature within subsequent cycles
A_g	Gross concrete cross-section area
A_{vf}	Shear friction reinforcing steel bar cross-sectional area
b	Steel strain hardening ratio
[B]	Transformation matrix from displacement to deformation
$\{b_n\}$	Vector of zero except the degree of freedom load applied
{D}	Global displacement vector
d_b	Bar diameter
defx	Deformation of mesh in x direction
defy	Deformation of mesh in y direction
defxy	Shear deformation of mesh in y direction
defyx	Shear deformation of mesh in x direction
d_i	Nodal displacement
$\{d\}_i$	Tangent displacement vector
E_0	Slope of elastic asymptote (Modulus of Elasticity)
E_1	Slope of yield asymptote
[E]	Elasticity matrix
E_c	Elastic modulus for concrete
f_c'	Peak concrete compressive strength
{f}	Local internal force vector of one mesh
{F}	Global internal force vector
$\{F\}_i$	Reference vector
$\{F_{ext}\}$	External force vector
$\{F_{unb}\}$	Unbalanced force vector
f_t	Peak concrete tensile stress
f_y	Yield strength of the bare reinforcing steel bars
[G]	Strain matrix
[k]	Local stiffness matrix of one mesh

$[K]$	Global stiffness matrix
$[K_t]_i$	Global tangent stiffness matrix
h	Height of mesh
m	Mesh number in horizontal direction
n	Mesh number in vertical direction
N_i	Shape function for finite element model
P_{ax}	Axial load at top level of rectangular wall
P_{lat}	Lateral load
r	Parameter defining shape of monotonic stress-strain curve for concrete
R_0	The value assigned to the parameter R for initial (or monotonic) loading
t	Thickness of mesh
$[T]$	Transformation matrix for body constraint
u	Generic displacement of mesh in x direction
v	Generic displacement of mesh in y direction
V_n	Shear force on the crack surface
w	Width of mesh
ε_0	Strain at the point of intersection of the two asymptotes
ε_1	Principal strain in direction 1
ε_2	Principal strain in direction 2
ε_c'	Strain at peak compressive strain
ε_{cr}	Concrete cracking strain
ε_r	Strain at the point of strain reversal
ε_t	Monotonic strain at peak concrete tensile stress
ε_x	Normal strain in x direction
ε_y	Normal strain in y direction
$\varepsilon_{x'}$	Arbitrary strain transformed to x' direction
$\varepsilon_{y'}$	Arbitrary strain transformed to y' direction
γ_{xy}	Shear strain
σ_0	Stress at the point of intersection of the two asymptotes
σ_{c1}	Concrete stress in principal direction 1
σ_{c2}	Concrete stress in principal direction 2

σ_r	Stress at the point of strain reversal
σ_{cx}	Concrete normal stress in x direction
σ_{cy}	Concrete normal stress in y direction
$\sigma_{cx'}$	Concrete stress in x' direction
$\sigma_{cy'}$	Concrete stress in y' direction
σ_x	Normal stress in x direction
σ_y	Normal stress in y direction
τ_{cxy}	Concrete shear stress
τ_{xy}	Shear stress
θ_{cr}	Concrete Crack direction or Fixed Strut Angle
θ_{crA}	Concrete Crack direction A or Fixed Strut Angle A
θ_{crB}	Concrete Crack direction B or Fixed Strut Angle B
μ	Friction coefficient
α	Angle between shear friction reinforcement and shear plane
ξ	Normalized local coordinates of a mesh in x direction
η	Normalized local coordinates of a mesh in y direction
$\Delta\lambda$	The initial load increment
$\Delta\delta_n$	The initial displacement increment
$\Delta\delta$	Displacement increment
$\Delta\delta_R$	Residual displacement increment

LIST OF ACRONYMS/ABBREVIATIONS

ACI	American Concrete Institute
DOF	Degree of freedom
FEM	Finite element model
FSAM	Fixed strut angle model
LVDT	Linear variable differential transducers
RW	Rectangular wall

1. INTRODUCTION

1.1. General

Reinforced concrete (RC) structural walls are commonly used because of their significant contribution in resisting lateral actions imposed on building structures, including earthquake effects and wind loads. Presence of structural walls has considerable impact on strength and stiffness characteristics, as well as the deformation capacity of structures. They substantially improve the performance of buildings in resisting earthquake ground motions. The effectiveness of structural walls makes it important to understand and characterize their hysteretic behavior when subjected to earthquake actions. Therefore, there have been numerous analytical and experimental studies to investigate the behavior of RC walls. Experimental studies have been conducted to characterize the behavior of existing walls while analytical studies are essential for response prediction of new walls as well as for improving design provisions. In order to comprehend the hysteretic behavior of RC walls, both experimental investigations and analytical modeling studies are deemed essential.

There are various computer programs for the analysis of structural systems, almost all of which incorporate significant defects due to not representing important behavioral characteristics associated with the nonlinear hysteretic behavior of RC structural walls. With implementation of the performance-based analysis and design approaches in modern design codes, detailed modeling of the nonlinear behavior of walls has gained much more importance. While representing the linear elastic behavior of walls is not a significant challenge in design, there is still a considerable need for reliable analytical modeling approaches for robust simulation of the nonlinear hysteretic behavior of walls. In theory, analytical modeling of the inelastic response of RC walls can be conducted by using either microscopic (e.g., finite element) or macroscopic (e.g., plastic hinge or fiber) modeling approaches. Microscopic modeling approaches are typically not used in performance-based design applications, due to complexities in their implementation and calibration, as well as interpretation of the results. A widely-known and commonly-used finite element modeling

approach for nonlinear analysis and design of structural walls is still not available. On the other hand, macroscopic modeling approaches available in the literature, with the so-called fiber models being the most common, are generally sufficient for modeling of uncoupled shear and flexural responses in a wall. However, typical macroscopic modeling approaches fail to reliably capture the nonlinear shear response characteristics in walls, and shear-flexure interaction effects that have been observed experimentally for even slender walls. Although consideration of nonlinear shear behavior is typically deemed important for response prediction of squat (low-rise) walls; unexpected shear yielding behavior, nonlinear shear deformations, and nonlinear shear-flexure interaction effects have also been observed experimentally for slender walls that have been designed to yield in flexure and are expected to show almost linear elastic shear behavior. Hence, there is still a need for robust modeling methodologies, using meso-scale approaches, which can capture such behavioral attributes in RC structural walls.

Based on these shortcomings, in this study, a relatively simple yet robust finite element model formulation is developed for simulating the in-plane behavior of RC structural walls under reversed cyclic loading conditions; one which considers nonlinear flexural and shear responses, as well as their interaction throughout the loading history. The proposed finite element model formulation is implemented in Matlab, together with a nonlinear analysis solution strategy. The model is calibrated and validated against experimental results obtained for a relatively slender RC wall specimen tested previously. Model response predictions are evaluated and sensitivity of the model results to important response parameters are investigated, for assessment of the capabilities of the model, as well as for identifying potential model improvements.

1.2. Literature Review

1.2.1. Flexural Modeling

Well designed and detailed walls are expected yield in flexure before shear capacity is reached, and dissipate hysteretic energy due to nonlinear flexural deformations associated with yielding of longitudinal reinforcement. Therefore, most of the modeling approaches available in the literature for RC walls are intended to simulate nonlinear

flexural behavior. The simplest and most widely-used model for structural walls consists of a linear elastic line element, with nonlinear rotational springs at each end for representing the flexural behavior at the critical regions where nonlinear deformations are expected. For an improved characterization of nonlinear wall behavior, Kabeyasawa *et al.* (1983) first conducted a full-scale test on a seven story RC frame-wall building in Tsubaka, Japan and based on this test results proposed a new macroscopic Three-Vertical-Line-Element Model (TVLEM). This model incorporated three vertical line elements with two rigid beams at both ends, outside vertical elements representing the axial stiffness of the boundary regions; and three springs representing the web of the wall, one vertical, one horizontal and one rotational (Figure 1.1). Two hysteric models were defined for the behavior of the springs. An axial-stiffness-hysteresis model (ASHM) was used for the vertical line elements while the origin-oriented-hysteresis model (OOHM) was used for the rotational and horizontal springs.

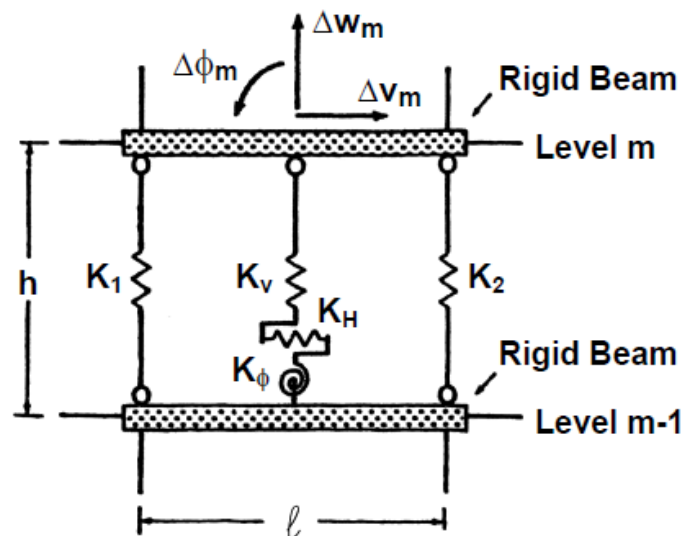


Figure 1.1. Three-Vertical-Line-Element Model (TVLEM) (Kabeyasawa *et al.*, 1983).

After development of this model, Vulcano and Bertero (1986) modified the TVLEM formulation by replacing the axial-stiffness-hysteresis model (ASHM) with the two-axial-element-in-series model (AESM) (Figure 1.2). The main purpose of this modification on the TVLEM was to capture the actual hysteretic behavior of the materials and their interaction (yielding and hardening of the steel, concrete cracking, contact stress, bond

degradation etc.). While the AESM gave reasonable results for the flexural behavior of a wall, the OOHM was found to be insufficient for representing inelastic shear behavior. Overall, the modified TVLEM adequately represented the inelastic flexural behavior of a wall, but failed to simulate its inelastic shear behavior.

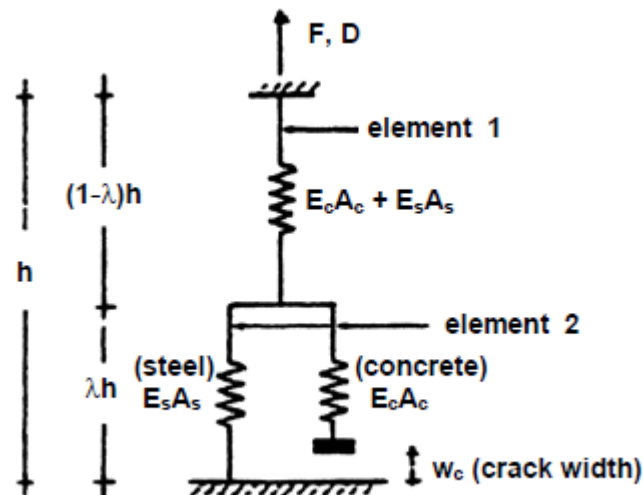


Figure 1.2. Axial-Element-in-Series Model (AESM) (Vulcano and Bertero, 1986).

Vulcano, Bertero and Colotti (1988), first proposed the so-called Multi-Component-Parallel Model (MCPM, also known as Multiple-Vertical-Line Element Model MVLEM), for obtaining more accurate results for the flexural behavior of a RC structural wall. This model had two outside vertical elements for the boundary regions, and more than two interior vertical elements for the web, in order to represent the axial-flexural behavior of a wall (Figure 1.3). The hysteretic behavior of all vertical line elements was described by the AESM. Simulation of the nonlinear shear response was done using a horizontal shear spring, similar to the TVLEM. Hysteretic behavior of this spring was described by the OOHM. The authors also modified the AESM by improving the uncracked part of the axial behavior for concrete. In this model, the hysteretic behavior of the materials were adopted. The stress-strain relationship proposed by Menegotto and Pinto (1973) was adopted for steel. The stress-strain relationship proposed by Colotti and Vulcano (1987) was implemented for uncracked concrete, whereas the stress-strain relationship proposed by Bolong *et al.* (1980) was adopted cracked concrete. The constitutive material models

adopted, together with the inclusion of tension stiffening effects using the AESM resulted in reliable predictions for the flexural behavior of the RC structural walls. However, the model was again insufficient in simulating the nonlinear shear behavior.

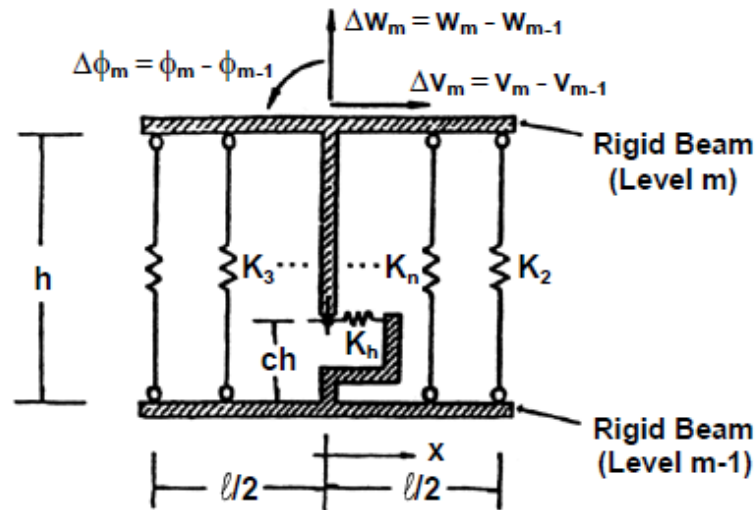


Figure 1.3. Multiple-Vertical-Line-Element Model (MVLEM) (Vulcano *et al.*, 1988).

Due to complexity in modeling of material behavior, additional studies were conducted to simplify the material models implemented in the MVLEM without impairing the accuracy of the results. Fischinger *et al.* (1990), proposed simplified models for the vertical and horizontal springs of the model and proposed a modified MVLEM formulation. However, the new formulation incorporated uncertainties in calibration of the material model parameters of material models. In the same year, Fajfar and Fischinger (1990) improved the hysteretic material model formulations to minimize the uncertainties in the assumed parameters. After development of this theory, Fischinger, Vidic and Fajfar (1992) conducted analytical studies and proved that the modified-MVLEM provided good response predictions for coupled RC walls. The importance of confinement effects and nonlinear shear behavior in wall response were emphasized in this study.

In 1997, Kabeyasawa modified the original Three-Vertical-Line-Element-Model (TVLEM) formulation to the so-called Panel-Wall Macro Element (PWME). The aim of this modification was to improve the shear behavior of RC structural walls for both

monotonic and cyclic loading. In this model formulation, the centerline element in the TVLEM including horizontal, vertical and rotational springs, was replaced by a two dimensional panel element (Figure 1.4), intended to represent the nonlinear shear behavior of the wall. Reasonable response predictions were obtained using this model; however, simulation of nonlinear shear behavior was deemed to be subject to improvement.

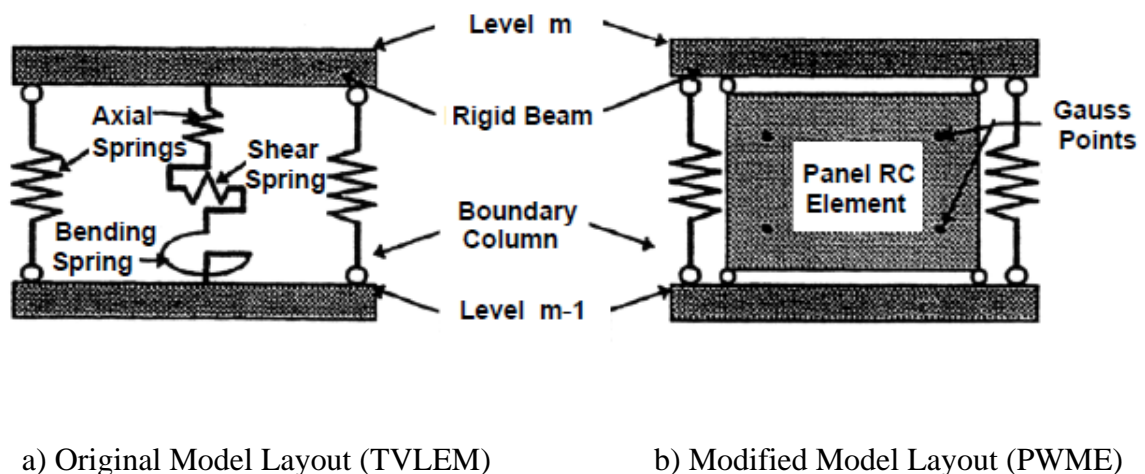
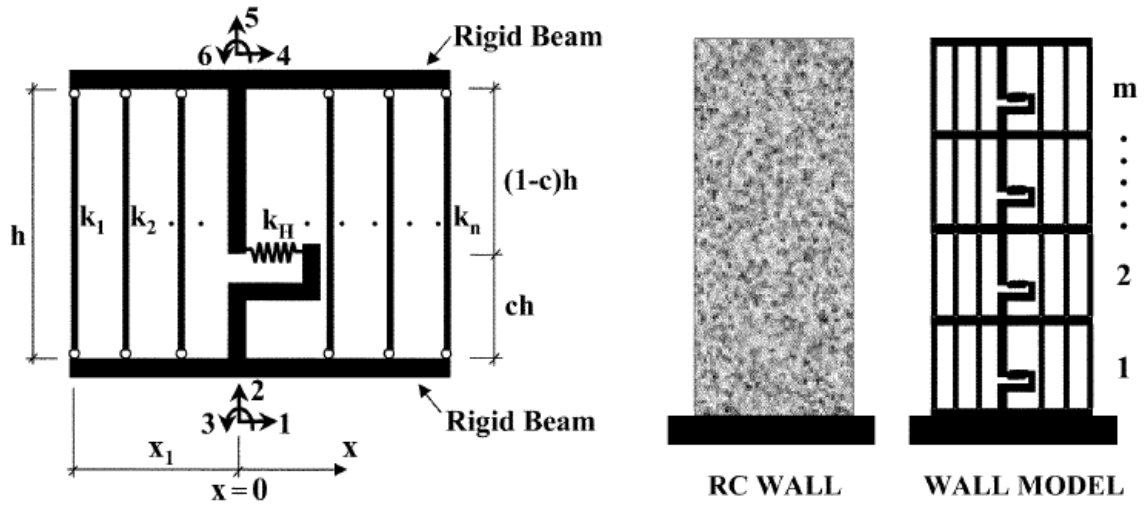


Figure 1.4. Modification of the TVLEM to PWME (Kabeyasawa *et al.*, 1997).

A more recent study was conducted by Orakcal *et al.* (2004) in order to improve the constitutive material models in the MVLEM. The improved model formulation included important material characteristics and behavioral response features (e.g., neutral axis migration, tension-stiffening, progressive gap closure, and nonlinear shear behavior). The model was calibrated and extensively validated against experimental data. At the end of this study, accurate response predictions were obtained for the cyclic behavior of RC structural walls governed by flexural deformations. However, the shear and flexural responses were still uncoupled in the formulation, indicating that the model was incapable of simulating shear-flexure interaction effects in RC walls.



a) MVLEM element

b) Model of a wall

Figure 1.5. MVLEM (Orakcal *et al.*, 2004).

1.2.2. Constitutive Modeling of RC Panel Behavior for Finite Element Modeling

In finite element modeling approaches, constitutive modeling of the in-plane stress-strain behavior of the model elements under a two-dimensional state of stress, becomes essential. Therefore, studies were conducted to develop constitutive modeling approaches for RC membrane (panel elements), which were complemented with RC panel tests. In this context, Mitchell and Collins (1974) first proposed the so-called Diagonal Compression Field Theory (DCFT), in order to represent the monotonic load vs. deformation behavior of RC panels. Vecchio and Collins (1986) then conducted a comprehensive test program on numerous RC panel specimens and introduced the well-known Modified Compression Field Theory (MCFT). In the MCFT formulation, while the main features of the DCFT (e.g., coinciding principal strain and stress directions, perfect bond) were maintained, several behavioral parameters were added (e.g., compression softening, tension stiffening, and shear transfer along crack surfaces). Negligence of dowel action in reinforcing bars and not being suitable for hysteretic loading were the main shortcoming of this theory.

Another constitutive modeling approach for RC panels was introduced by Mau and Hsu (1986, 1987), based on equilibrium, compatibility, and material stress-strain

relationships. In this study, boundaries among different failure modes were identified, and cracked concrete was treated as a new material working along diagonal compression strut directions. Based on this study, Hsu (1988) introduced a new constitutive modeling approach called the Softened Truss Model (STM). By using tension stiffening relationships for cracked concrete, this approach was developed for solving nonlinear shear and torsion problems.

In 1989, an experimental research program was conducted at the Kajima Institute of Construction Technology, in which reversed-cyclic tests were carried out on numerous RC panel specimens. As a result of this study, a nonlinear constitutive modeling strategy was introduced by Ohmori *et al.* (1989). This approach, which incorporated improved stress-strain models for the materials, was apparently the cyclic version of MCFT.

Based on experimental results obtained for cyclic testing of three panel specimens, Stevens *et al.* (1991) proposed another hysteretic constitutive modeling approach for RC panels. In this approach, considering the deviation between principal strain and stress direction was proposed for the first time. The model was calibrated for the panel specimens tested during the experimental program, and reasonable response predictions were obtained for their observed nonlinear shear behavior.

Another important panel model formulation was developed by Pang and Hsu, (1995), who proposed the Rotating Angle Softened Truss Model (RA-STM). which was the improved version of the Softened Truss Model (Hsu, 1988). In this new constitutive model, compression softening and tension stiffening were represented by new parameters. In addition to these features, kinking effect, which represents the softening effect on reinforcing bars caused by dowel action, was taken into account in the model formulation. After the development of the RA-STM, Pang and Hsu (1996) proposed a new constitutive panel model called the Fixed Angle Softened Truss Model (FA-STM). In this modeling approach, unlike the MCFT or RA-STM, it was assumed that the direction of the cracks coincide with the fixed angle following the principal directions of the applied stresses.

Vecchio (2002) introduced a new theory called the Disturbed Stress Field Model (DSFM) to represent the constitutive behavior of RC panels. Within the scope of this

theory, the crack directions in the panel were assumed to coincide with the principal stress directions and principal stress directions deviated from principal strain directions by a fixed “lag” angle. In 2003, another cyclic version of the Modified Compression Field Theory was proposed by Vecchio and Palermo (2003). In this study, new constitutive material relationships were introduced. Response simulation studies were conducted by implementing the model formulation into nonlinear finite element analysis platform and comparing model results with experimental results obtained for RC walls.

Hsu and Zhu (2002) proposed another constitutive panel model called the Softened Membrane Model (SMM). Consideration of Poisson’s effects was the major improvement of this model formulation over the FA-STM. Results of this study revealed that the influence of the kinking effect on the response, which had been discussed in development of the FA-STM, was negligible. In 2005, new experimental program was conducted in order to develop improved hysteretic material models for RC panels. As a result of these experiments, a new model, which is the cyclic version of the SMM, was proposed by Mansour and Hsu (Mansour and Hsu, 2005). This model formulation incorporated new cyclic constitutive relationships both for concrete and reinforcing steel.

A new constitutive panel model was proposed by Gérin and Adebar (2009). In this model, principal strain directions were assumed to coincide with principal stress directions, whereas the crack directions were considered to be fixed. In this model formulation, new hysteretic multi-linear stress-strain relationships for reinforcing steel and concrete were implemented, and an empirical relationship was proposed for representing compression softening effects.

A recent constitutive model for RC panels, named the Fixed Strut Angle Model (FSAM), was proposed for simulating the cyclic shear behavior of reinforced concrete panel elements (Ulugtekin, 2010, Orakcal *et al.*, 2012). In this model formulation, the main assumption was that crack directions in concrete do not rotate, as observed consistently in reinforced concrete panel and wall tests, and coincide with principal stress directions in concrete. Model predictions were compared with results of cyclic tests on RC panel specimens and the model was observed to accurately predict the shear response characteristics of panel elements; including cyclic shear stress vs. shear strain behavior,

shear stress capacity, shear stiffness, cyclic stiffness degradation, pinching, ductility, and failure mode. Due to accuracy and relatively simple formulation, the model was deemed to be a feasible candidate for implementation into two-dimensional finite-element analysis.

1.2.3. Modeling of Shear-Flexure Interaction in RC Walls

There are numerous analytical models in the literature for simulating the flexural response of RC walls, based on uniaxial stress vs. strain relationships for the materials. However, they do not consider shear-flexure interaction effects, which were observed experimentally for not only low-rise and shear-controlled walls, but also for slender walls whose behavior are expected to be governed by flexural deformations. The majority of analytical modeling approaches presented in the literature typically neglect or underestimate the influence of the shear-flexure interaction on the response of slender or medium-rise walls.

However, Petrangali *et al.* (1999) proposed a new model formulation, which was the pioneer of the fiber-based shear-flexure interaction models. Implementation of a constitutive RC panel element into a fiber-based model has since become the widely-used approach to capture the influence of shear-flexure interaction on the response of RC walls. In 2006, a study was conducted as part of a Pacific Earthquake Engineering Research (PEER) projects and a similar approach was used in developing an analytical model to represent the observed coupling between flexural and shear response components in RC walls (Orakcal *et al.*, 2006). In this study, it was discussed that experimental results showed interaction between shear and flexural deformations even for slender walls exists. Within the scope of the study, the Multiple-Vertical-Line-Element Model (MVLEM) was modified to consider the influence of shear-flexure interaction, by assigning a shear spring for each uniaxial element. With this new approach to the MVLEM, each line element was treated as a RC panel element with membrane actions for capturing coupled shear and flexural responses. A rotating-angle modeling approach (essentially the rotating-angle softened-truss model, RA-STM) was used to represent the constitutive panel behavior. The constitutive material model for concrete was modified to adopt behavior under biaxial stresses. One of the main shortcomings of this model was that the shear-flexure interaction

modeling approach was limited to monotonic loading, because of the monotonic formulation of RA-STM.

Other and simpler approaches are proposed for representation of shear-flexure interaction behavior in RC walls. An empirical modeling approach was developed by Beyer *et al.* (2011). In this approach, the ratio between flexural and shear deformations in a wall is defined empirically based on wall geometry, axial strain, and crack angle. Lack of the reliance on test data made this approach restricted. Although this methodology has been shown to produce reasonable estimation of the ratio between shear and flexural deformations for walls controlled by flexure, despite with significant dispersion, the approach is limited due to its reliance on test data (i.e., interpolation and extrapolation without an underlying behavior-based model). In the same year, a strut-and-tie (truss) modeling approach was introduced by Panagiotou *et al.* (2011), as an alternative method to capture shear-flexure interaction. In this approach, the interaction between shear and flexural responses is accounted for by reducing the concrete compressive strut capacity as a function of transverse tensile strain. However, due to overlapping areas of vertical, horizontal, and diagonal concrete struts in the model, achieving accurate displacement responses over a broad range of response amplitudes is a challenge, which is a known issue with strut-and-tie models.

In a recent study conducted by Kolozvari *et al.* (2012) a new analytical model formulation was proposed for capturing the shear-flexure interaction in medium-rise RC walls under reversed-cyclic loading. The proposed analytical model incorporated RC panel behavior, described by Fixed-Strut-Angle panel model (FSAM) into the Multiple Vertical Line Element Model (MVLEM). Analytical model was compared with experimental results obtained for medium-rise walls, for experimental verification of the model. Comparison of the analytical and experimental results showed that the analytical model was able to capture coupling of nonlinear shear and flexural deformations in walls. Although reasonably accurate predictions were obtained, the analytical model results were found to be sensitive to modeling parameters representing shear aggregate interlock effects and dowel action, and the model was unable to capture the sliding shear behavior at the base of walls. The model was found to be subject to improvement upon calibration with

various wall geometries, and use of more refined constitutive modeling approaches for shear aggregate interlock and dowel action.

1.2.4. Experimental Studies on Shear-Flexure Interaction in RC Walls

There are numerous experimental studies in the literature on investigating the lateral load behavior RC structural walls. However, experimental studies that focus on characterizing the nonlinear shear behavior and coupling of shear and flexural responses in walls, for modeling purposes, are relatively few. Only the experimental studies relevant to the scope of this study are summarized here. Orakcal and Wallace (2006) conducted an analytical study to experimentally-validate the MVLEM (Orakcal *et al.*, 2004) for relatively slender structural walls. For experimental validation of the model, test results obtained for two, approximately quarter-scale wall specimens tested by Thomsen and Wallace (1995); one specimen with a rectangular cross section (Specimen RW2) and another specimen with a T-shaped cross section (Specimen TW2) were used. The walls were 3.66 m tall and 102 mm thick, with web and flange lengths of 1.22 m. The walls were relatively slender, with an aspect ratio of 3. Design of the specimens was based on a prototype building, with strength requirements satisfying the UBC94, and detailing requirements following a displacement-based evaluation. Test measurements were processed to allow for a direct comparison of the predicted and measured flexural responses. Responses were compared at various locations on the walls. Results obtained with the analytical model for rectangular walls compared favorably with experimental responses for flexural capacity, stiffness, and deformability, although some significant variation was noted for local compression strains. For T-shaped walls, the agreement between model and experimental results was reasonably good, although the model was unable to capture the variation of the longitudinal strains along the flange.

An experimental program was conducted at the University of California Los Angeles (UCLA) Structural/Earthquake Engineering Research Laboratory (SEERL) in order to assess the performance low-rise lightly-reinforced RC wall piers and spandrels in existing buildings that had been built between the 1950s and 1970s (Orakcal *et al.*, 2009). In order to evaluate and rehabilitate these types of walls, cyclic lateral load tests were conducted in the laboratory. Test results were compared with ACI-318-05 provisions and FEMA 356

recommendations on walls to evaluate the reliability of the documents for rehabilitation of existing buildings. Observations indicated that the amount of boundary reinforcement provided, presence of axial load, and the location of a weakened plane joint on the wall were the most important factors in the assessment of nominal shear strength. The test results were compared with predictions of a monotonic shear-flexure interaction model (Massone *et al.*, 2009) for RC walls. Model results indicated that variation in the assumed transverse normal stress or strain distribution produced important response variations. The use of the average experimentally recorded transverse normal strain data or a calibrated analytical expression resulted in better predictions of shear strength and lateral load-displacement behavior, as did incorporating a rotational spring at wall ends to model extension of longitudinal reinforcing bars within the pedestals.

The cyclic shear-flexure interaction modeling approach developed by Kolozvari *et al.* (2012) model was validated by comparing the model predictions with experimental results obtained by Tran and Wallace (2012). The experimental study was conducted to provide insight into the nonlinear cyclic response of moderate-aspect ratio cantilever structural walls. Constant axial load and reversed cyclic loading were applied to five large-scale structural walls. Primary test variables were wall aspect ratio, wall axial stress, and wall shear stress. The test results indicate that significant lateral strength loss occurred at approximately 3.0% for all tests; however, various failure modes were observed. The contribution of nonlinear shear deformations to wall top lateral displacement varied between roughly 15% and 50%, for walls with aspect ratios of 2.0 and 1.5, respectively.

1.3. Research Significance

In recent years, performance-based analysis and design methodologies for RC buildings have gained significance. Use of performance-based modeling and assessment procedures for RC frame systems have typically provided reliable results, while important behavioral issues related to modeling of RC structural walls are still unknown. To conduct reliable performance analyses for walls, coupling between their nonlinear axial, flexural and shear responses should be well-defined under reversed cyclic loading conditions. In performance-based design practice, RC structural walls are typically modeled using commercial finite element analysis software, which do not represent important behavioral

characteristics with sufficient detail, or using macroscopic fiber models consisting of multiple vertical line elements for flexure and horizontal springs for shear, in which flexural and shear responses are uncoupled. A commonly-used finite element modeling approach for nonlinear analysis of structural walls is still not available, and there is a need for simple yet reliable modeling methodologies that can capture important response characteristics of RC structural walls.

1.4. Objectives and Scope

The aim of this study is to develop a relatively simple yet robust finite element model formulation for simulating the nonlinear behavior of RC structural walls under reversed cyclic loading conditions. The proposed modeling methodology is capable of representing nonlinear flexural and shear responses, and their interaction throughout the loading history. The model incorporates a fixed crack angle modeling approach, which is suitable for reversed cyclic loading conditions and feasible for implementation into a two dimensional finite element analysis platform.

Within the scope of this study, formulation of the proposed finite element modeling approach and the assembly procedure to obtain the global stiffness matrix and internal force vector are implemented in Matlab, together with a nonlinear analysis solution strategy. The model is calibrated and validated against experimental results obtained for a relatively slender RC wall specimen. Model response predictions are evaluated for assessment of the model capabilities and limitations. Sensitivity of the model results to important response parameters are also investigated.

1.5. Thesis Outline

This thesis summarizes the findings of analytical studies conducted on development of a new nonlinear finite element modeling approach for simulating the coupled nonlinear flexural and shear responses in RC structural walls. Development of the two-dimensional finite element modeling approach based on the implemented constitutive panel behavior is described, and response predictions obtained using the finite element model are compared with experimental results for evaluation of model capabilities and shortcomings. In

Chapter 1, an introduction and a literature review, as well as the objectives and scope of this study were provided. Description of the implemented constitutive panel model and material stress-strain relationships are presented in Chapter 2. A detailed description of the finite element model formulation, involving stiffness assembly, internal force vector assembly, support conditions, constraints, nonlinear analysis solution strategy, is provided in Chapter 3. Chapter 4 presents information on experimental calibration of the model and detailed comparison of the model results with test results obtained from the literature for a relatively slender RC structural wall, as well as results of the parametric sensitivity studies conducted. Finally, concluding remarks and recommendations for future studies are presented in Chapter 5.

2. CONSTITUTIVE MODEL DESCRIPTION

2.1. Overview

Two dimensional finite element modeling of RC structural walls requires a constitutive RC panel element to simulate the constitutive behavioral features of RC structural walls (e.g. hysteretic material behavior, compression softening, tension stiffening, hysteretic biaxial damage, and shear transfer across cracks). In this chapter, properties of the constitutive RC panel element and the material constitutive relationships adopted in the finite element model formulation are described,

The constitutive panel model selected for implementation into the two dimensional finite element model is the Fixed Strut Angle Model (FSAM) proposed by Ulugtekin (2010). The FSAM is a feasible candidate for implementation into a two dimensional finite element analysis formulation. Formulation of the FSAM is based on interpretation of previously-developed RC panel models, as well as results of RC panel tests available in the literature. In this section, the formulation and important characteristics of the FSAM are summarized. Detailed information on the FSAM is provided in the thesis by Ulugtekin (2010).

In the first version of the Fixed Strut Angle Model proposed by Ulugtekin (2010), effects of shear aggregate interlock and dowel action on the response of RC panels were neglected. However, the zero shear stress assumption along the crack directions resulted in significant overestimation of sliding shear strains along cracks. Hence, a simple friction-based constitutive model was adopted to represent shear aggregate interlock effects and implemented into the panel model formulation by Orakcal *et al.* (2012). In this study, the Fixed Strut Angle Model with the modification proposed to represent shear aggregate interlock effects (Orakcal *et al.*, 2012), which is described in detail in the following section, has been implemented as a constitutive panel model. Implementation of dowel

action, that is the shear stresses developing perpendicular to the longitudinal direction of the reinforcing steel bars, has also been neglected in the present implementation.

2.2. Panel Model

In the constitutive panel model implemented, as it was typically assumed in other RC panel elements available in the literature, assumptions of perfect bond between concrete and reinforcing steel and no dowel action on reinforcing bars are valid. The perfect bond assumption provides the advantage of having the same strain fields on concrete and reinforcing steel, while dowel action effects (shear stresses perpendicular to the longitudinal direction of the reinforcing steel) are typically negligible in the shear behavior of RC members. For the hysteretic constitutive modeling of reinforcing steel bars, uniaxial directions along the rebar directions were used, whereas for the constitutive modeling of concrete stress-strain behavior, biaxial relations along the fixed strut (crack) directions were incorporated.

A rotating strut approach, similar to the Modified Compression Field Theory (Vecchio and Collins, 1986) and the Rotating Angle Strut and Tie Model (Pang and Hsu, 1995) were used for simulation of the biaxial stress-strain behavior of uncracked concrete. For the uncracked loading stages of the RC panel, the hysteretic behavior of concrete was assumed to be monotonic, which is for small strains prior to cracking. At this stage, the principal strains directions obtained from the applied strain field were assumed to coincide with principal stress directions in concrete. The constitutive material model for concrete is therefore applied along the principal strain directions (Figure 2.1).

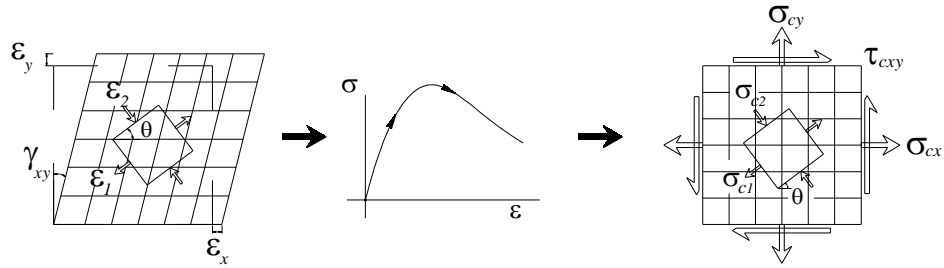


Figure 2.1. Uncracked behavior of concrete in the Fixed Strut Angle Model (Orakcal *et al.*, 2012).

When the principal tensile strain first exceeds the monotonic cracking strain value of concrete, the first crack forms in the RC panel model, in perpendicular direction to the principal tensile strain. Formation of the first crack means that for subsequent loading, the first "Fixed Strut" direction, which is parallel to the first crack, is assigned. For further stages of loading, principal stress directions in concrete coincide with the first crack directions (parallel and perpendicular), while principal strain directions continue to rotate with the applied strain field. Since the first crack direction coincides with principal stress directions in concrete, zero shear stress (zero shear aggregate interlock) develops along the crack, which is an inherent assumption in the original FSAM formulation.

After formation of the first crack, the hysteretic stress-strain relationship for concrete is used in directions parallel and perpendicular to the fixed strut. Calculation of these principal stresses in concrete is only possible with transformation of the strain field into directions parallel or perpendicular to the fixed strut, rather than the principal strain directions. After calculation of the strains parallel and perpendicular to the fixed strut direction, concrete stress values are determined by using the uniaxial constitutive model adopted for concrete. Calculated stresses in parallel and perpendicular directions to the fixed strut are reduced by biaxial compression softening and biaxial damage parameters, which are described in detail in the following section. The hysteretic uniaxial constitutive material model implemented for reinforcing steel (also described in the following section) is applied along the orthogonal rebar directions to calculate the stresses in reinforcing steel. Superposition of stresses developing in concrete and reinforcing steel (using reinforcing

steel area ratios) provides the resultant averages stresses on the panel element. Behavior of concrete in the FSAM after formation of the first crack is illustrated in Figure 2.2.

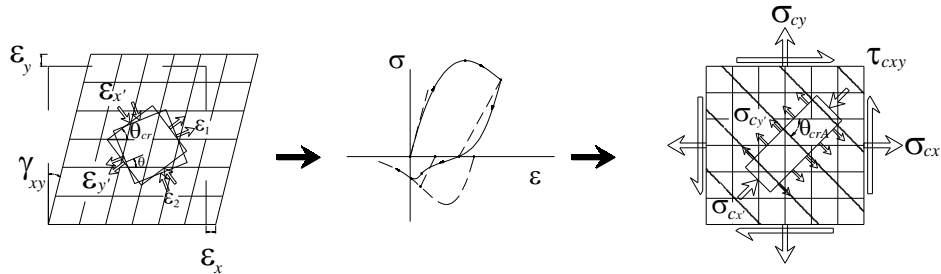


Figure 2.2. Behavior of concrete after formation of first crack in the Fixed Strut Angle Model (Orakcal *et al.*, 2012).

Until the formation of the second crack, the constitutive behavior proceeds in the form of a single fixed strut mechanism. When the tensile strain along the first strut direction exceeds the cyclic cracking strain of concrete, the second crack is formed. The second crack is formed perpendicular to the first crack because of the zero shear stress assumption along the crack directions. The first and second cracks in the panel element are therefore orthogonal. Examples of this “orthogonal crack” modeling approach are common in the literature. Formation of the second crack perpendicular to the first fixed strut implies formation of the second “fixed strut”. Depending on the loading direction, these fixed struts work under tension or compression. For subsequent loading stages, principal stress directions in concrete are fixed along the fixed strut directions, whereas principal strain values are free to rotate. In order to determine the principal stresses in concrete, the applied strain field is transformed into strain components in the fixed strut directions instead of principal strain directions. Calculated strain values parallel to the two fixed strut directions are used in the uniaxial constitutive model for concrete to obtain the principal stresses in concrete, and the concrete stresses are reduced by compression softening and biaxial damage parameters. Again, the constitutive material model for reinforcing steel is applied along the orthogonal rebar directions and superposition of stresses developing in concrete and reinforcing steel gives the resultant averages stresses on the panel element. Behavior of concrete in the FSAM after formation of the second crack is shown in Figure 2.3.

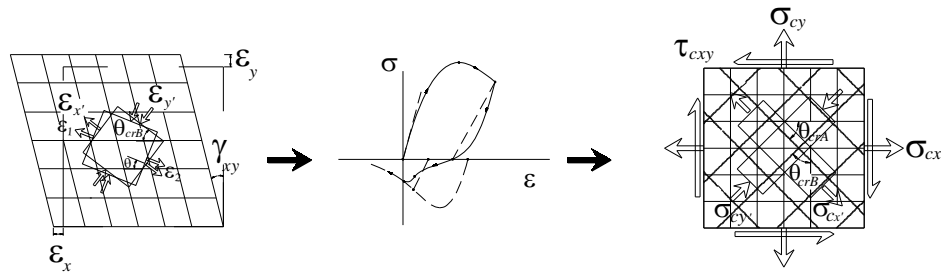


Figure 2.3. Behavior of concrete after formation of second crack in the Fixed Strut Angle Model (Orakcal *et al.*, 2012).

2.3. Material Constitutive Models

2.3.1. Constitutive Model for Reinforcement

The implemented constitutive hysteretic material model for reinforcing steel is the well-known nonlinear hysteretic relationship of Menegotto and Pinto (1973), extended by Filippou *et al.* (1983) to represent isotropic strain hardening. This constitutive model, although simple in formulation, has been shown to accurately represent experimental results on reinforcing steel bars. The constitutive model represents the so-called Bauschinger's effect, by including cyclic degradation of stiffness along the unloading and reloading curves. A description of the constitutive model is depicted in Figure 2.4.

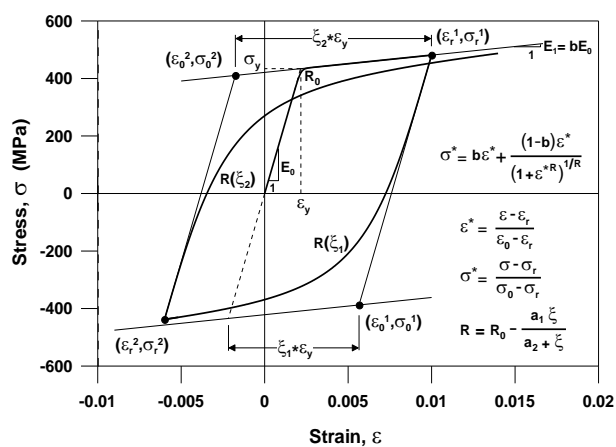


Figure 2.4. Hysteretic constitutive model for reinforcing steel (Menegotto and Pinto, 1973).

2.3.2. Constitutive Model for Concrete

The implemented stress-strain behavior for concrete is the uniaxial hysteretic constitutive model proposed by Chang and Mander (1994) (Figure 2.5). The Chang and Mander model has been shown to provide accurate representation of the experimental results presented by various researchers. Mander *et al.* (1988) calibrated the model for unconfined and confined concrete in cyclic compression. Experimental validation studies against test results reported by Gopalaratman and Shah (1985) and Yankelevsky and Reinhardt (1987) have shown that the model provides reliable results for unconfined and confined concrete under cyclic tension and compression.

This constitutive model implemented for concrete was modified by adding compression softening (defined by Vechio and Collins, 1993), hysteretic biaxial damage (defined by Mansour *et al.*, 2002) and tension stiffening effects (defined by Belarbi and Hsu, 1994) into the formulation. The aim of these modifications was to simulate the behavioral features of concrete under biaxial loading conditions.

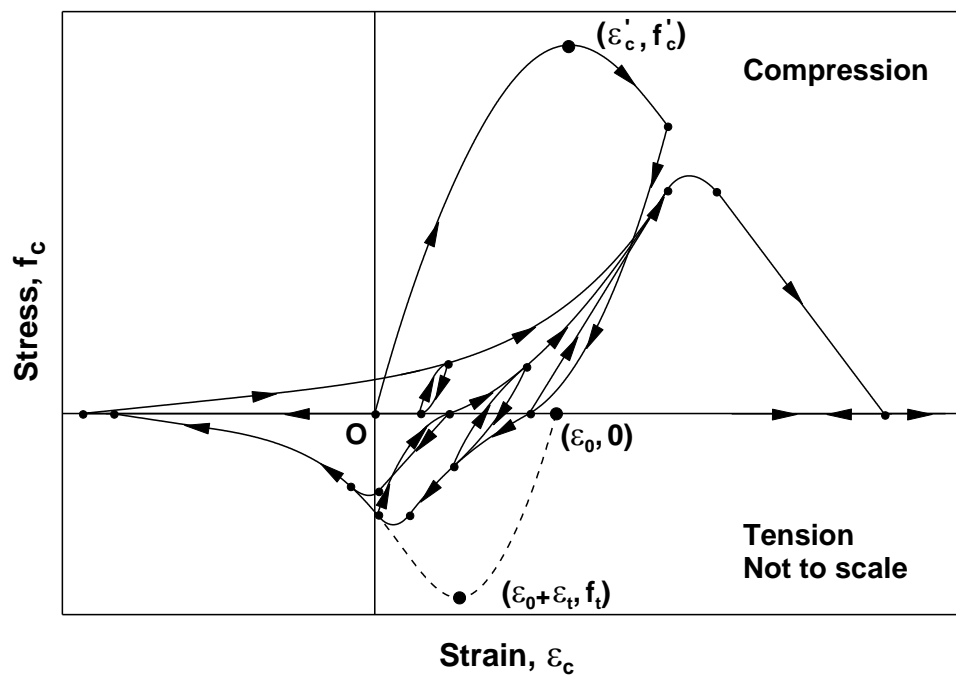


Figure 2.5. Hysteretic constitutive model for concrete (Chang and Mander, 1994).

2.3.3. Compression Softening of Concrete

Consideration of the so-called compression softening effects is important in modeling of RC panel elements. This effect has been experimentally observed by many researchers (e.g., Vecchio and Collins, 1986), and constitutive models were proposed to represent it. The compression softening effect, stemming from the tensile strains perpendicular to crack directions, is typically simulated by reduction in the compressive stresses in concrete in the principal directions (Figure 2.6).

The compression softening relationship proposed by Vecchio and Collins (1993) was implemented into Fixed Strut Angle constitutive panel model formulation. Although more complicated models are available for the representing compression softening effects, this relationship was found to provide reasonably accurate predictions of experimentally-observed behavior, despite its simplicity.

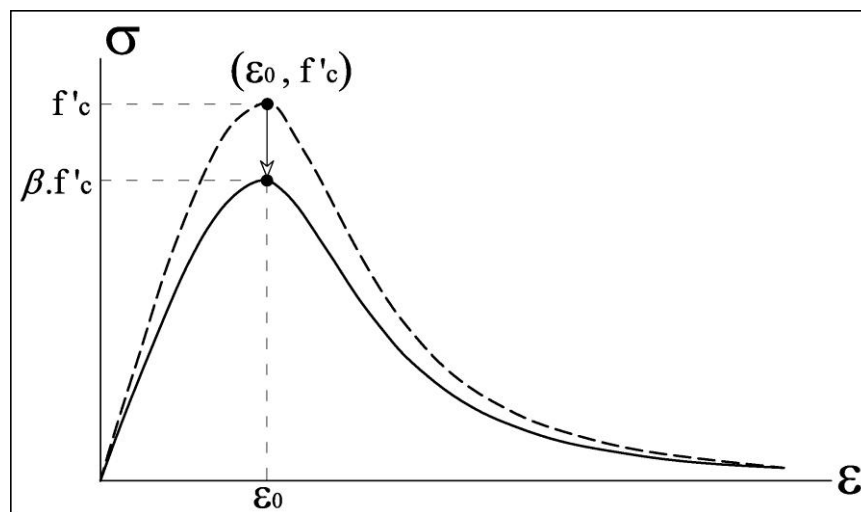


Figure 2.6. Compression softening effects implemented in the panel model (Ulugtekin, 2010).

2.3.4. Tension Stiffening Effect on Concrete and Reinforcing Steel

Tension stiffening effect is named after the contribution of cracked concrete to the tensile resistance of a RC member. The post-cracking stiffness, yield capacity and shear

behavior of the RC members have been shown to be influenced by the tension stiffening effect. The tension stiffening relationship proposed by Belarbi and Hsu (1994) was incorporated in the formulation of the constitutive panel model. This relationship considers two effects simultaneously. The first of these effects is the consideration of an average (smeared) tensile stress-strain curve for cracked concrete; while the other is the replacement of stress-strain curve for bare steel bars with an average (smeared) stress-strain curve for steel bars stiffened by concrete between cracks.

2.3.5. Biaxial Damage on Concrete

A RC panel element, when subjected to membrane actions (biaxial loading) experiences damage on concrete, which is simulated via a damage coefficient in modeling the constitutive behavior of concrete within the panel element. This biaxial damage phenomenon physically reflects as softening in the compressive stress-strain behavior of concrete along one direction, depending on the maximum value of the previously-applied compressive strain in the perpendicular direction. The biaxial damage behavior is therefore loading-history-dependent and is not observed under monotonic loading. In terms of constitutive modeling, the damage coefficient, similar to the compression softening coefficient, is typically applied as a reducing multiplier to compressive stresses in concrete.

There are two empirical models available in literature for the damage coefficient; one by Stevens (1987), and the other by Mansour and Hsu (2002). The biaxial damage relationship proposed by Mansour and Hsu (2002) was implemented into the formulation of constitutive Fixed Strut Angle panel model used in this study.

2.3.6. Shear Aggregate Interlock

The original formulation of the Fixed Strut Angle constitutive panel model described in this chapter was developed by Ulugtekin (2010). However, shear aggregate interlock effects were neglected in the original formulation. Orakcal *et al.* (2012) implemented a simple friction-based elasto-plastic shear aggregate interlock model into the panel model formulation. In this study, the main modification to the constitutive panel model is incorporation of the contribution of reinforcing steel in the shear aggregate interlock

model. The yield capacity of the friction-based aggregate interlock model was modified based on ACI 318M-08 provisions, to consider the influence of reinforcing steel in the shear-friction capacity.

The proposed cyclic shear aggregate interlock model starts with linear loading/unloading behavior, relating the sliding shear strain along a crack to the shear stress, via a simple linear elastic relationship between the sliding shear strain and the resultant shear stress along the crack surface. When the contribution of reinforcing steel to the shear stress is not considered, the shear stress is restrained to zero value when the concrete normal stress perpendicular to the crack is tensile (crack open); and is bounded via the product of a friction coefficient and the concrete normal stress perpendicular to the crack, when the concrete normal stress is compressive (crack closed). When the contribution of reinforcing steel on the aggregate interlock capacity is considered, as was done in this study, the interlock shear capacity (V_n) along a crack is calculated using Equation 2.1 when the reinforcement is perpendicular to the crack, and Equation 2.2 when the reinforcement is inclined with respect to the crack:

$$V_n = \mu(A_{vf}f_y + N) \quad (2.1)$$

$$V_n = \mu \sin \alpha (A_{vf}f_y + N) + \cos \alpha (A_{vf}f_y + N) \quad (2.2)$$

where μ is a friction coefficient, $A_{vf}f_y$ is the axial force corresponding to tensile yielding in reinforcing steel due to sliding shear along the crack surface, N is the axial force in concrete perpendicular to the crack, and α is the angle between the reinforcement and the crack plane (Figure 2.7).

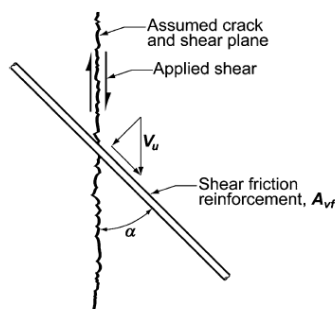


Figure 2.7. Shear-friction mechanism along a crack (ACI-318M, 2008).

The linear unloading/reloading slope of the shear stress vs. sliding strain relationship was taken as a fraction of the concrete elastic modulus (a value $0.4E_c$ was adopted, representing the elastic shear modulus of concrete), and a value of 1.1 was assumed for the friction coefficient. Under constant compressive stress in concrete perpendicular to the crack, this model yields an elasto–plastic aggregate interlock behaviour under cyclic loading, similar to the cyclic stress–strain behaviour of reinforcing steel. It must be mentioned that the friction coefficient needs to be further calibrated with experimental data on panel or wall specimens experiencing sliding shear failures along cracks.

3. FINITE ELEMENT MODEL DESCRIPTION

Civil and mechanical engineers manipulate the finite element modeling approach to analyze structures under loads. In this process, First, structural models are subdivided into reasonable number of elements, each of which is characterized by a force-deformation relationship. Second, the elements are assembled together through a well-defined procedure, which is the local equilibrium at each node. Finally, unknown displacements or forces are solved using the resulting equations.

This chapter presents a description of the two-dimensional finite element modeling methodology developed in this study for response simulation of RC structural walls. Four node, eight degree of freedom finite elements were used for modeling of a local element in this study. Assembly of the local stiffness matrixes as well as the internal force vector of these local elements (mesh elements) are described in the following sections. Implementation of support conditions and constraints for modeling of walls are also described and the adopted nonlinear analysis solution strategy is summarized.

3.1. 4 Nodes, 8 Degree of Freedom Rectangular Element (Mesh)

A rectangular two-dimensional finite element modeling approach has been adopted modeling of RC structural walls. The two-dimensional rectangular element works as a membrane element, meaning four node elements were formulated in two dimensional space. Membrane elements have two degree of freedoms (DOFs) for each node, in vertical and horizontal directions and do not incorporate any rotational DOFs. The main idea in the formulation of membrane element is that it is valid for in-plane conditions, implying that only in-plane stiffness is considered and only in-plane loads are admissible.

In the formulation of the rectangular element (mesh element), each local DOF is numbered as shown in Figure 3.1.

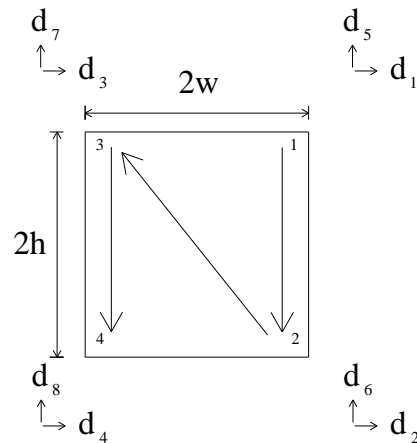


Figure 3.1. Local nodes and DOFs in a rectangular element.

In a rectangular FEM element, strains can be calculated using shape functions (Figure 3.2), based on the displacement values along the nodal degrees of freedom.

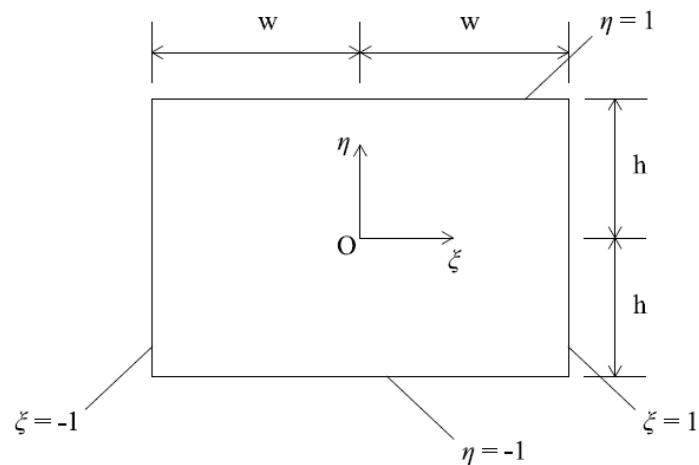


Figure 3.2. Normalized coordinates of a rectangular element.

Using the known displacements along the DOFs, (Figure 3.1), which are obtained by solving equilibrium equations at the four nodes of the rectangular element, and the shape functions presented in Equations 3.1 to 3.4, displacement values along horizontal and vertical directions at any point of rectangular element can be obtained (Equation 3.5).

$$N_1 = \frac{1}{4}(1+\xi)(1+\eta) \quad (3.1)$$

$$N_2 = \frac{1}{4}(1+\xi)(1-\eta) \quad (3.2)$$

$$N_3 = \frac{1}{4}(1-\xi)(1+\eta) \quad (3.3)$$

$$N_4 = \frac{1}{4}(1-\xi)(1-\eta) \quad (3.4)$$

$$\begin{Bmatrix} \mathbf{u} \\ \mathbf{v} \end{Bmatrix} = \begin{bmatrix} N_1 & N_2 & N_3 & N_4 & 0 & 0 & 0 & 0 \\ 0 & 0 & 0 & 0 & N_1 & N_2 & N_3 & N_4 \end{bmatrix} \begin{Bmatrix} d_1 \\ d_2 \\ d_3 \\ d_4 \\ d_5 \\ d_6 \\ d_7 \\ d_8 \end{Bmatrix} \quad (3.5)$$

However, in this study, strain and stress values are only calculated at the center of each rectangular element, corresponding to $\xi = \eta = 0$, for the sake of simplicity. Derivation of the zero normalized coordinates is described in Equations 3.6 and 3.7.

$$\xi = \frac{x}{w} = \frac{0}{w} = 0 \quad (3.6)$$

$$\eta = \frac{y}{h} = \frac{0}{h} = 0 \quad (3.7)$$

At the beginning of analysis for a load step, by using the initial displacements at the nodes of a structural wall model, initial displacements of each node are calculated. After calculation of the eight displacement values for each model element, deformations of each element are calculated by using the transformation matrix [B] (Equation 3.8).

$$\begin{Bmatrix} \text{defx} \\ \text{defy} \\ \text{defyx} \\ \text{defxy} \end{Bmatrix} = \begin{bmatrix} \frac{1}{2} & \frac{1}{2} & -\frac{1}{2} & -\frac{1}{2} & 0 & 0 & 0 & 0 \\ 0 & 0 & 0 & 0 & \frac{1}{2} & -\frac{1}{2} & \frac{1}{2} & -\frac{1}{2} \\ \frac{1}{2} & -\frac{1}{2} & \frac{1}{2} & -\frac{1}{2} & 0 & 0 & 0 & 0 \\ 0 & 0 & 0 & 0 & \frac{1}{2} & \frac{1}{2} & -\frac{1}{2} & -\frac{1}{2} \end{bmatrix} \begin{Bmatrix} d_1 \\ d_2 \\ d_3 \\ d_4 \\ d_5 \\ d_6 \\ d_7 \\ d_8 \end{Bmatrix} \quad (3.8)$$

Then, local deformation matrixes (deformation matrix of each model element) are used for the calculation of local strain values in each element.

$$\varepsilon_x = \frac{\text{defx}}{2w} \quad (3.9)$$

$$\varepsilon_y = \frac{\text{defy}}{2h} \quad (3.10)$$

$$\gamma_{xy} = \frac{\text{defyx}}{2h} + \frac{\text{defxy}}{2w} \quad (3.11)$$

Next step is the calculation of the local stiffness matrixes for each element. The Fixed Strut Angle constitutive model (Ulugtekin, 2010) implemented in the FEM formulation is used for the calculation of tangent stiffness (elasticity) matrices for each model element. All strain values are used as input values for the constitutive panel model. By using these input values, tangent stiffness matrices are obtained as output values, as illustrated in Figure 3.3.

$$\begin{Bmatrix} \varepsilon_x \\ \varepsilon_y \\ \gamma_{xy} \end{Bmatrix} \rightarrow \text{Fixed Strut Angle Panel Model (FSAM)} \rightarrow \begin{bmatrix} E_{11} & E_{12} & E_{13} \\ E_{21} & E_{22} & E_{23} \\ E_{31} & E_{32} & E_{33} \end{bmatrix}$$

Figure 3.3. Tangent stiffness (elasticity) matrix calculation path.

At this point the aim is obtaining the local stiffness matrices for the model elements, which are further assembled to generate global tangent stiffness matrix for the structural wall model. Each local stiffness matrix can be obtained using the tangent stiffness matrix and the geometric properties of each element. In definition of the FEM approach, this operation is performed by integration of the product of transpose of strain matrix $[G]^T$, the elasticity matrix $[E]$, and the strain matrix $[G]$. It is important to mention that unlike the calculation of the strain and stress values, during the volume integration in given in Equation 3.12, normalized coordinates $\xi = \frac{x}{w}, \eta = \frac{y}{h}$ cannot be assumed to be constant because both ξ and η are dependent on x and y , respectively.

$$[k] = \int_V [G]^T [E] [G] dV = \int_V [G]^T [E] [G] dx dy dz \quad (3.12)$$

The integral Equation 3.12 is used to calculate the 8×8 stiffness matrix $[k]$ for each model element. Each element of the matrix can be calculated as:

$$k_{11} = \frac{t}{3} \left(E_{11} \beta + E_{33} \frac{1}{\beta} \right) \quad (3.13)$$

$$k_{21} = \frac{t}{3} \left(E_{11} \frac{\beta}{2} - E_{33} \frac{1}{\beta} \right) \quad (3.14)$$

$$k_{31} = \frac{t}{3} \left(-E_{11} \beta + E_{33} \frac{1}{2\beta} \right) \quad (3.14)$$

$$k_{41} = \frac{t}{3} \left(-E_{11} \frac{\beta}{2} - E_{33} \frac{1}{2\beta} \right) \quad (3.16)$$

$$k_{51} = \frac{t}{4} (E_{12} + E_{33}) \quad (3.17)$$

$$k_{61} = \frac{t}{4} (-E_{12} + E_{33}) \quad (3.18)$$

$$k_{71} = \frac{t}{4} (E_{12} - E_{33}) \quad (3.19)$$

$$k_{81} = \frac{t}{4} (-E_{12} - E_{33}) \quad (3.20)$$

$$k_{55} = \frac{t}{3} \left(E_{22} \frac{1}{\beta} + E_{33} \beta \right) \quad (3.21)$$

$$k_{65} = \frac{t}{3} \left(-E_{22} \frac{1}{\beta} + E_{33} \frac{\beta}{2} \right) \quad (3.22)$$

$$k_{75} = \frac{t}{3} \left(E_{22} \frac{1}{2\beta} - E_{33} \beta \right) \quad (3.23)$$

$$k_{85} = \frac{t}{3} \left(-E_{22} \frac{1}{2\beta} - E_{33} \frac{\beta}{2} \right) \quad (3.24)$$

where $\beta = \frac{h}{w}$, t is the thickness of the membrane element and E values are scalar values taken from the elasticity matrix. Using the equations above, the 8×8 local stiffness matrix for each element can be calculated as the matrix defined in Equation 3.25.

$$[k] = \begin{bmatrix} k_{11} & k_{21} & k_{31} & k_{41} & k_{51} & k_{61} & k_{71} & k_{81} \\ k_{21} & k_{11} & k_{41} & k_{31} & k_{71} & k_{81} & k_{51} & k_{61} \\ k_{31} & k_{41} & k_{11} & k_{21} & k_{61} & k_{51} & k_{81} & k_{71} \\ k_{41} & k_{31} & k_{21} & k_{11} & k_{81} & k_{71} & k_{61} & k_{51} \\ k_{51} & k_{71} & k_{61} & k_{81} & k_{55} & k_{65} & k_{75} & k_{85} \\ k_{61} & k_{81} & k_{51} & k_{71} & k_{65} & k_{55} & k_{85} & k_{65} \\ k_{71} & k_{51} & k_{81} & k_{61} & k_{75} & k_{85} & k_{55} & k_{65} \\ k_{81} & k_{61} & k_{71} & k_{51} & k_{85} & k_{75} & k_{65} & k_{55} \end{bmatrix} \quad (3.25)$$

The local stiffness matrix $[k]$ of each model element was calculated by following the described procedure. The next step in modeling is the assembly of these local stiffness matrices, which is described in the following section.

3.2. Finite Element Model Stiffness Assembly

In this section, details on the assembly of local stiffness matrixes are provided. Determining the local stiffness matrix for each model element is the first step to the assembly. The next step is assembling of all local stiffness matrices to develop the global stiffness matrix for the wall model. As a general example for the assembly of the local stiffness matrices, a sample model is illustrated in Figure 3.4. After the numbering of the

nodes and elements, the global stiffness matrix assembly is performed as shown in Figure 3.5.

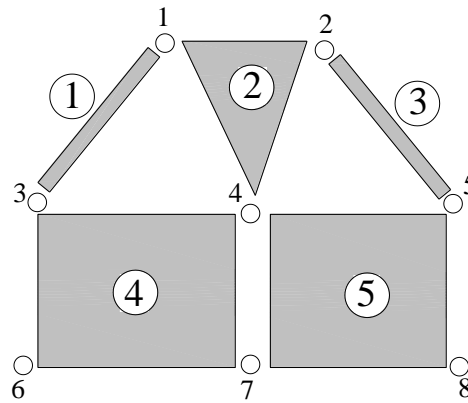


Figure 3.4. Numbering of nodes and elements in a sample model.

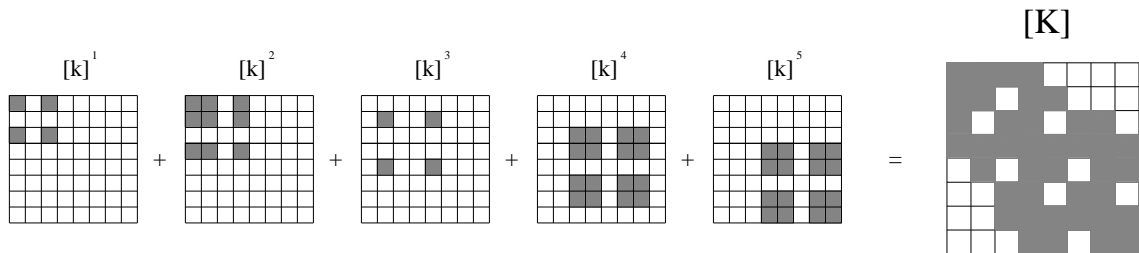


Figure 3.5. Superposition of stiffness matrixes.

The presented sample is a very general case for the assembly strategy, which is essential to comprehend the logic of assembly. There are five elements included in the sample model and each of the element stiffness matrices are shown in Figure 3.5. The assembly is performed via superposition on the overlapping boxes (terms) within the global stiffness matrix. As shown in the example shown in Figure 3.6 for a rectangular wall model, the wall is subdivided into model elements and the elements are first numbered for the assembly operation.

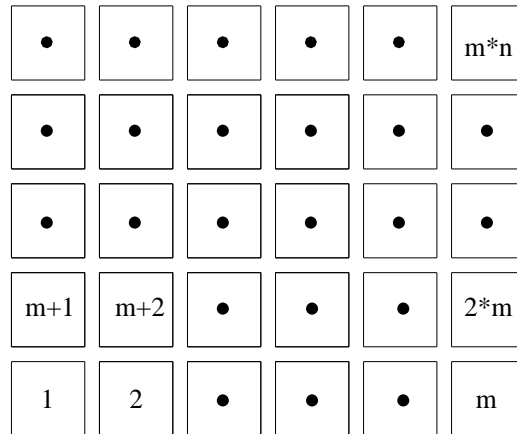


Figure 3.6. Numbering technique used for the FEM of a rectangular wall.

After numbering of each model element, the overlapping terms of the 8×8 local stiffness matrices are superimposed with each other for generating the global stiffness matrix of the model. In order to explain the superposition strategy, generation of the global stiffness matrix of a wall model with four model elements is illustrated. The global DOFs of the wall model are first numbered (Figure 3.7), which defines the order of the terms in the global displacement vector and global stiffness matrix.

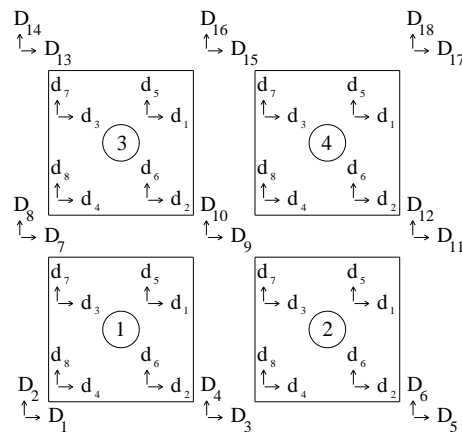


Figure 3.7. Global and local DOFs in a structural wall model.

In Figure 3.7, DOF numbers displayed inside the model elements are local DOFs and DOF numbers displayed outside the elements are global DOFs. Global stiffness matrix of

this sample model is calculated by superimposing the local stiffness terms at overlapping locations within the global stiffness matrix. Equation 3.26 is an example for calculation of one of the terms in the global stiffness matrix. Superscripts in Equation 3.26 indicate the model element numbers while subscripts indicate the local stiffness term index for each model element.

$$[\mathbf{K}]_{99} = [\mathbf{k}]_{11}^1 + [\mathbf{k}]_{33}^2 + [\mathbf{k}]_{22}^3 + [\mathbf{k}]_{44}^4 \quad (3.26)$$

Each term in the global stiffness matrix of the wall model is calculated by the same procedure used in Equation 3.26. For this sample, there exist 18 global DOFs, implying that the global stiffness matrix will be an 18×18 matrix, with 324 terms.

3.3. Internal Force Vector Assembly

In this section, definitions of the local internal force vectors and the assembly procedure to obtain the global internal force vector are presented in detail. Knowing the average strain values for each model element, the average stresses in each element can be calculated using the constitutive Fixed Strut Angle panel model (Figure 3.8).

$$\left\{ \begin{array}{c} \varepsilon_x \\ \varepsilon_y \\ \gamma_{xy} \end{array} \right\} \rightarrow \text{Fixed Strut Angle Panel Model (FSAM)} \rightarrow \left\{ \begin{array}{c} \sigma_x \\ \sigma_y \\ \tau_{xy} \end{array} \right\}$$

Figure 3.8. Stress vector calculation path.

Stress values are multiplied with thickness and half of vertical or horizontal width and superimposed to obtain the internal force vector for each element. Numbering of the internal force vector components, which is similar to the local displacement numbering scheme is illustrated in Figure 3.9.

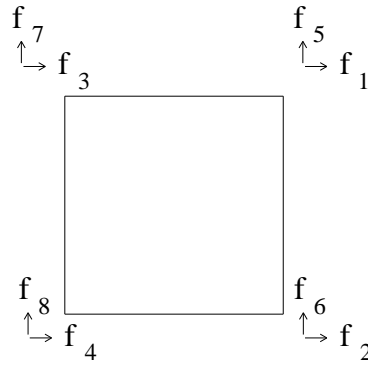


Figure 3.9. Numeration of internal forces for a mesh.

The adopted numbering scheme and the obtained stress values can be used in combination to calculate the terms of the internal force vector for each model element. Calculation of the internal force values along each nodal DOF is performed using equilibrium, as depicted in Equations 3.27 to 3.34.

$$f_1 = \sigma_x \times h \times t + \tau_{xy} \times w \times t \quad (3.27)$$

$$f_2 = \sigma_x \times h \times t - \tau_{xy} \times w \times t \quad (3.28)$$

$$f_3 = -\sigma_x \times h \times t + \tau_{xy} \times w \times t \quad (3.29)$$

$$f_4 = -\sigma_x \times h \times t - \tau_{xy} \times w \times t \quad (3.30)$$

$$f_5 = \sigma_y \times w \times t + \tau_{xy} \times h \times t \quad (3.31)$$

$$f_6 = -\sigma_y \times w \times t + \tau_{xy} \times h \times t \quad (3.32)$$

$$f_7 = \sigma_y \times w \times t - \tau_{xy} \times h \times t \quad (3.33)$$

$$f_8 = -\sigma_y \times w \times t - \tau_{xy} \times h \times t \quad (3.34)$$

Each model element undergoes the same procedure to obtain internal force values. The local internal force vectors are then superimposed in order to obtain the global internal force vector for the wall model. For the sample assembly shown in Figure 3.4, the internal force vector assembly would be performed as shown in Figure 3.10. As described for the calculation of the terms in the global stiffness matrix, overlapping internal forces values in the global force vector are superimposed.

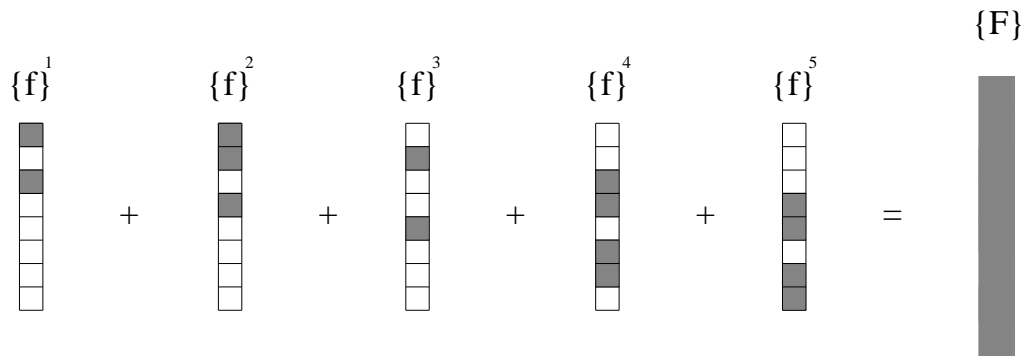


Figure 3.10. Superposition of internal force vectors.

As shown with the example RC structural wall is subdivided into meshes and all meshes have been enumerated (Figure 3.6) for the assembly operation. After the numeration of each mesh, the intersection of 8×1 local internal force vectors with each other is superimposed to generate global internal force vector. In order to explain the superposition strategy, generation of global internal force vector of a RC structural wall with four meshes is developed. Global DOFs are enumerated, which provides global force vector (Figure 3.11).

For the sample illustrated in Figure 3.6, the overlapping terms of the 8×1 local internal force vectors *are* superimposed with each other for generating the global internal force vector of the model. In order to explain the superposition strategy, generation of the internal force vector of a wall model with four model elements is illustrated. The global DOFs of the wall model define the order of the terms in the global force vector for the wall model.

In Figure 3.11, DOF numbers displayed inside the model elements are local DOFs and DOF numbers displayed outside the elements are global DOFs. The global internal force vector of this sample model is calculated by superimposing the local internal force vector terms at overlapping locations within the global force vector. Equation 3.35 is an example for calculation of one of the terms in the global internal force vector. Superscripts in Equation 3.35 indicate the model element numbers while subscripts indicate the local internal force vector index for each model element.

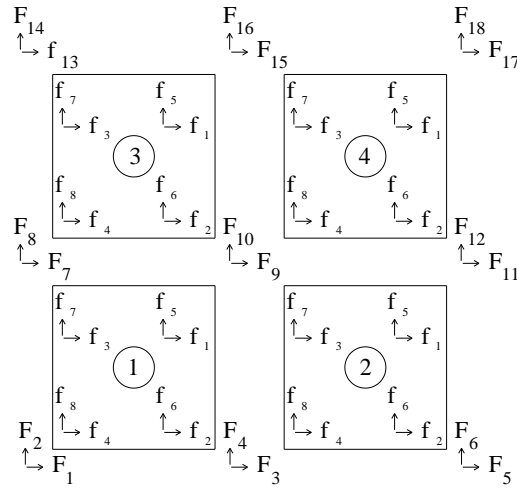


Figure 3.11. Global and local DOFs in a structural wall model.

$$\{F\}_{91} = \{f\}_{11}^1 + \{f\}_{31}^2 + \{f\}_{21}^3 + \{f\}_{41}^4 \quad (3.35)$$

Each term in the global internal force vector of the wall model is calculated by the same procedure used in Equation 3.35. For this sample, there exist 18 global DOFs, implying that the global internal force vector will be an 18×1 vector.

3.4. Support Conditions and Constraints

At the supports of a RC wall, the displacements are zero. This kinematic condition is incorporated into the finite element model of the wall, via enforcing zero displacement along the DOFs of the model at the supports (Figure 3.12), and solving the equilibrium equation by partitioning. Through this procedure, the reaction forces at the supports are calculated from the equilibrium equation, using the known (zero) displacement values along the DOFs at the supports.

In addition, in order to simulate the test conditions for which the wall model was experimentally validated, enforcement of constraint conditions along selected DOFs may be necessary. For example, during loading tests, rigid beams are typically connected to the top of RC wall specimens, in order to transmit the vertical and lateral loads applied externally by hydraulic actuators to the wall specimen.

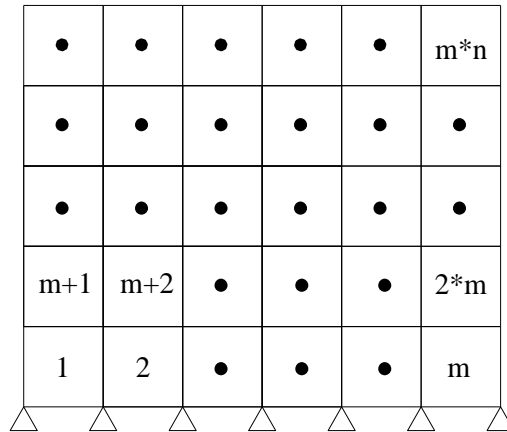


Figure 3.12. Support conditions in the FEM.

Since the wall specimen that was used for experimental validation of the model in the current study was connected to steel load transfer beam at the top, which behaved like a rigid body, a body constraint was defined along the top DOFs of the FEM of the wall specimen (Figure 3.13).

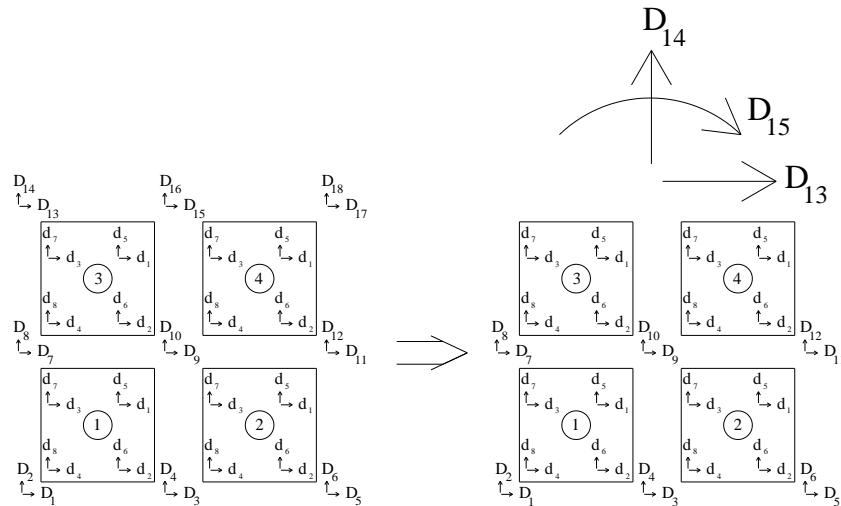


Figure 3.13. Conversion of DOFs after the assignment of body constraint.

Body constraint is implemented in the model formulation using a displacement transformation matrix [T]. The body constraint condition enforces equal horizontal displacement in the horizontal direction while relating vertical displacements to a global

rotational displacement at the top of the a wall through the plane-sections-remain-plane condition. The aim of implementing the body constraint in the model is representation of a rigid load transfer beam possibly connected to the top of a RC wall specimen during testing. The transformation matrix defined for a sample wall model wall with four model elements is given in Equation 3.36. Derivation of the global stiffness matrix, the global internal force vector, and the displacement vector of the wall model after assignment of the body constraint are given in Equations 3.37 to 3.40. Equation 3.40 gives the result of the production of the transpose of the transformation matrix [T] with both sides of Equation 3.37. It must be mentioned that this wall model assembly with only four model elements is merely a simple example aimed to demonstrate the general formulation of the FEM, and that more model elements are typically required for a reliable model assembly.

$$[T]_{18 \times 15} = \begin{bmatrix}
 1 & 0 & 0 & 0 & 0 & 0 & 0 & 0 & 0 & 0 & 0 & 0 & 0 & 0 & 0 & 0 & 0 & 0 \\
 0 & 1 & 0 & 0 & 0 & 0 & 0 & 0 & 0 & 0 & 0 & 0 & 0 & 0 & 0 & 0 & 0 & 0 \\
 0 & 0 & 1 & 0 & 0 & 0 & 0 & 0 & 0 & 0 & 0 & 0 & 0 & 0 & 0 & 0 & 0 & 0 \\
 0 & 0 & 0 & 1 & 0 & 0 & 0 & 0 & 0 & 0 & 0 & 0 & 0 & 0 & 0 & 0 & 0 & 0 \\
 0 & 0 & 0 & 0 & 1 & 0 & 0 & 0 & 0 & 0 & 0 & 0 & 0 & 0 & 0 & 0 & 0 & 0 \\
 0 & 0 & 0 & 0 & 0 & 1 & 0 & 0 & 0 & 0 & 0 & 0 & 0 & 0 & 0 & 0 & 0 & 0 \\
 0 & 0 & 0 & 0 & 0 & 0 & 1 & 0 & 0 & 0 & 0 & 0 & 0 & 0 & 0 & 0 & 0 & 0 \\
 0 & 0 & 0 & 0 & 0 & 0 & 0 & 1 & 0 & 0 & 0 & 0 & 0 & 0 & 0 & 0 & 0 & 0 \\
 0 & 0 & 0 & 0 & 0 & 0 & 0 & 0 & 1 & 0 & 0 & 0 & 0 & 0 & 0 & 0 & 0 & 0 \\
 0 & 0 & 0 & 0 & 0 & 0 & 0 & 0 & 0 & 1 & 0 & 0 & 0 & 0 & 0 & 0 & 0 & 0 \\
 0 & 0 & 0 & 0 & 0 & 0 & 0 & 0 & 0 & 0 & 1 & 0 & 0 & 0 & 0 & 0 & 0 & 0 \\
 0 & 0 & 0 & 0 & 0 & 0 & 0 & 0 & 0 & 0 & 0 & 1 & 0 & 0 & 0 & 0 & 0 & 0 \\
 0 & 0 & 0 & 0 & 0 & 0 & 0 & 0 & 0 & 0 & 0 & 0 & 1 & 0 & 0 & 0 & 0 & 0 \\
 0 & 0 & 0 & 0 & 0 & 0 & 0 & 0 & 0 & 0 & 0 & 0 & 0 & 1 & 0 & 0 & 0 & 0 \\
 0 & 0 & 0 & 0 & 0 & 0 & 0 & 0 & 0 & 0 & 0 & 0 & 0 & 0 & 1 & 0 & 0 & 0 \\
 0 & 0 & 0 & 0 & 0 & 0 & 0 & 0 & 0 & 0 & 0 & 0 & 0 & 0 & 0 & 1 & 2b & 0 \\
 0 & 0 & 0 & 0 & 0 & 0 & 0 & 0 & 0 & 0 & 0 & 0 & 0 & 0 & 0 & 0 & 1 & -2b \\
 0 & 0 & 0 & 0 & 0 & 0 & 0 & 0 & 0 & 0 & 0 & 0 & 0 & 0 & 0 & 0 & 1 & 0 \\
 0 & 0 & 0 & 0 & 0 & 0 & 0 & 0 & 0 & 0 & 0 & 0 & 0 & 0 & 0 & 0 & 1 & 0 \\
 0 & 0 & 0 & 0 & 0 & 0 & 0 & 0 & 0 & 0 & 0 & 0 & 0 & 0 & 0 & 0 & 1 & 0 \\
 0 & 0 & 0 & 0 & 0 & 0 & 0 & 0 & 0 & 0 & 0 & 0 & 0 & 0 & 0 & 0 & 1 & 2b
 \end{bmatrix} \quad (3.36)$$

$$[K]_{18 \times 18} \times \{D\}_{18 \times 1} = \{F_{\text{unb}}\}_{18 \times 1} \quad (3.37)$$

$$[K]_{18 \times 18} \times [T]_{18 \times 15} \times \{D\}_{15 \times 1} = \{F_{\text{unb}}\}_{18 \times 1} \quad (3.38)$$

$$[T]^T_{18 \times 15} \times [K]_{18 \times 18} \times [T]_{18 \times 15} \times \{D\}_{15 \times 1} = [T]^T_{18 \times 15} \times \{F_{\text{unb}}\}_{18 \times 1} \quad (3.39)$$

$$\begin{aligned}
& [T]_{18 \times 15}^T \times [K]_{18 \times 18} \times [T]_{18 \times 15} \times \{D\}_{15 \times 1} = [T]_{18 \times 15}^T \times \{F_{\text{unb}}\}_{18 \times 1} \\
& \quad \downarrow \qquad \qquad \qquad \downarrow \\
& [K]_{15 \times 15} \qquad \qquad \times \{D\}_{15 \times 1} = \qquad \qquad \{F_{\text{unb}}\}_{15 \times 1}
\end{aligned} \tag{3.40}$$

3.5. Nonlinear Analysis Solution Strategy

After assembly of the model elements for derivation of the global stiffness matrix and the internal force vector, and implementation of support conditions and constraints, a displacement-controlled nonlinear analysis solution strategy (Clarke and Hancock, 1990; Simons and Powell, 1982) was adopted for conducting displacement-controlled hysteretic lateral load analysis of RC walls using the proposed FEM. A displacement-controlled solution strategy was preferred in order to be able to correlate model results with results of drift-controlled lateral load tests conducted on RC wall specimens. Details of the selected nonlinear analysis solution strategy are presented in this section. The applied strategy consists of two main stages; load incrementation and equilibrium stages. For subsequent discussions, the load incrementation stage is denoted by "i" while the equilibrium stage is denoted by "j". During the incrementation stage, the target displacements imposed on the model are incremented, whereas during the equilibrium stage, iterations are performed on the model displacements, in order to reach equilibrium between the internal and external forces, within a specified tolerance.

For the first incrementation stage, the initial tangent stiffness matrix $[K_I]_i$ at the start of each load step is calculated using the geometric and material properties of the wall model. The next step in this stage is the definition of the reference load vector $\{F_I\}_i$. This reference vector depends on the normalized external load vector. For example if the load is applied along the the last DOF of the model, $\{F_I\}_i$ is defined as expressed in equation 3.41.

$$\{F_I\}_i = \begin{Bmatrix} 0 \\ 0 \\ \vdots \\ 1 \end{Bmatrix} \tag{3.41}$$

The so-called tangent displacement vector is then computed as defined in Equation 3.42.

$$\{\delta_I\}_i = \text{inv}[K_I]_i \{F_I\}_i \quad (3.42)$$

The computed tangent displacement vector is only for determination of the direction of the displacements in the analytical model. The magnitude of the components in the tangent displacement vector is not significant. Based on the imposed displacements applied in a controlled manner on the model, the reference displacement vector $\{b_n\}$ is also defined. $\{b_n\}$ is a vector of zeros except at the specific DOF, along which the displacement is controlled. For example if the imposed displacement on the model is controlled along the last DOF, $\{b_n\}$ takes the form shown in Equation 3.43.

$$\{b_n\} = \begin{Bmatrix} 0 \\ 0 \\ \vdots \\ 1 \end{Bmatrix} \quad (3.43)$$

After definition of the reference displacement vector $\{b_n\}$, the initial load increment $\Delta\lambda_i^{j=1}$ can be calculated as expressed in Equation 3.44.

$$\Delta\lambda_i^{j=1} = \frac{-\Delta\delta_n}{\{b_n\}^T \{\delta_I\}_i} \quad (3.44)$$

After calculation of initial load increment, the corresponding initial displacement increment can be calculated as:

$$\{\Delta\delta\}_i^{j=1} = \Delta\lambda_i^{j=1} \{\delta_I\}_i \quad (3.45)$$

and the total displacements and load level updated from those at the conclusion of the previous load step are calculated by:

$$\{\delta\}_i^{j=1} = \{\delta\}_{i-1} - \{\Delta\delta\}_i^{j=1} \quad (3.46)$$

$$\lambda_i^{j=1} = \lambda_{i-1} + \Delta\lambda_i^{j=1} \quad (3.47)$$

where λ is a scalar to be multiplied with the reference external load vector to obtain the external force vector (F_{ext}).

$$\{F_{ext}\}_i^{j=1} = \lambda_i^{j=1} \{F_I\}_i \quad (3.48)$$

While the external load vector is calculated from Equation 3.48, the internal force vector is calculated from the stresses developing in each model element (as described in Section 3.3). The next step is to compute the unbalanced force between external and internal force vectors. Calculation of the unbalanced force vector is expressed in Equation 3.41.

$$\{F_{umb}\}_i^{j=1} = \{F_{int}\}_i^{j=1} - \{F_{ext}\}_i^{j=1} \quad (3.49)$$

In nonlinear analysis, this unbalanced force vector incorporates terms larger than a specified tolerance, which means iterations "j" are necessary within the same load step "i", to reach equilibrium of the model. For commencement of the equilibrium iterations, the residual displacement increment can be calculated as:

$$\{\Delta\delta_R\}_i^j = \frac{\{F_{umb}\}_i^{j-1}}{[K_I]_i} \quad (3.50)$$

The incremental external force multiplier and nodal displacement vector can now be calculated from the residual displacement vector as:

$$\Delta\lambda_i^j = \frac{-\{b_n\}^T \{\Delta\delta_R\}_i^j}{\{b_n\}^T \{\delta_I\}_i} \quad (3.51)$$

$$\{\Delta\delta\}_i^j = \Delta\lambda_i^j \{\delta_I\}_i + \{\Delta\delta_R\}_i^j \quad (3.52)$$

After calculation of the load and displacement increments,, the nodal displacement vector and external force multiplier at the end of the current iteration cycle can be calculated as:

$$\{\delta\}_i^j = \{\delta\}_i^{j-1} + \{\Delta\delta\}_i^j \quad (3.53)$$

$$\lambda_i^j = \lambda_i^{j-1} + \Delta\lambda_i^j \quad (3.54)$$

In the next step, as was done in the load incrementation stage, the external force vector F_{ext} and the internal force vector F_{int} are recalculated, and the unbalanced (residual) force is defined as the difference between these two as:

$$\{F_{ext}\}_i^j = \lambda_i^j \{F_I\}_i \quad (3.55)$$

$$\{F_{unb}\}_i^j = \{F_{int}\}_i^j - \{F_{ext}\}_i^j \quad (3.56)$$

If terms in the unbalanced force vector are again larger than a specified tolerance, the equilibrium cycles are repeated until the external and internal forces are balanced, within the specified magnitude of tolerance. When this condition is satisfied, the load step is assumed converged, and the strategy is commenced for a new load step with a new incrementation cycle.

Graphical representations of the nonlinear analysis solution strategy described are illustrated in Figures 3.14 and 3.15 Further information on the solution strategy can be found in Clarke and Hancock (1990) and Simons and Powell (1982).

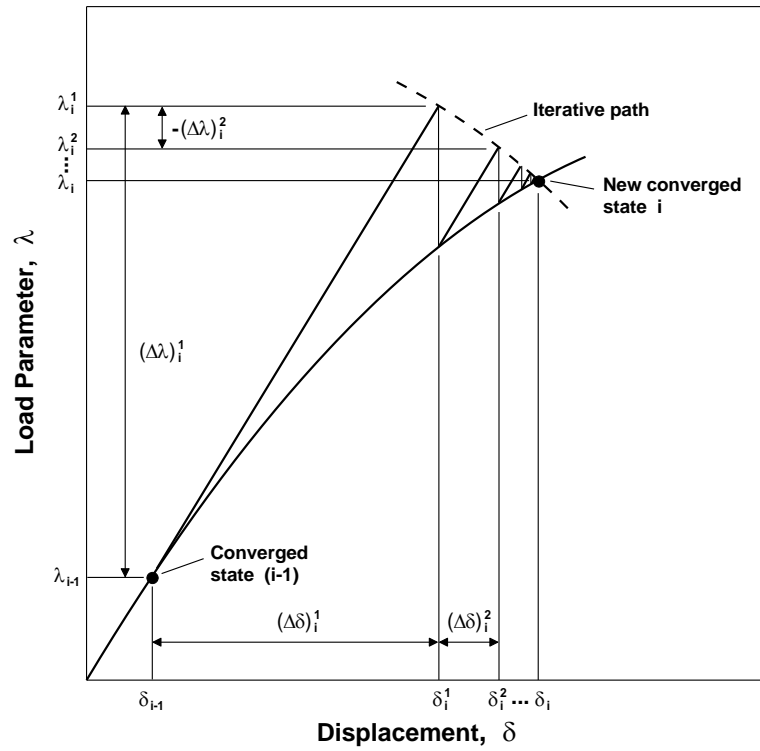


Figure 3.14. Representation of the nonlinear analysis solution strategy for a single degree of freedom system (Clarke and Hancock, 1990).

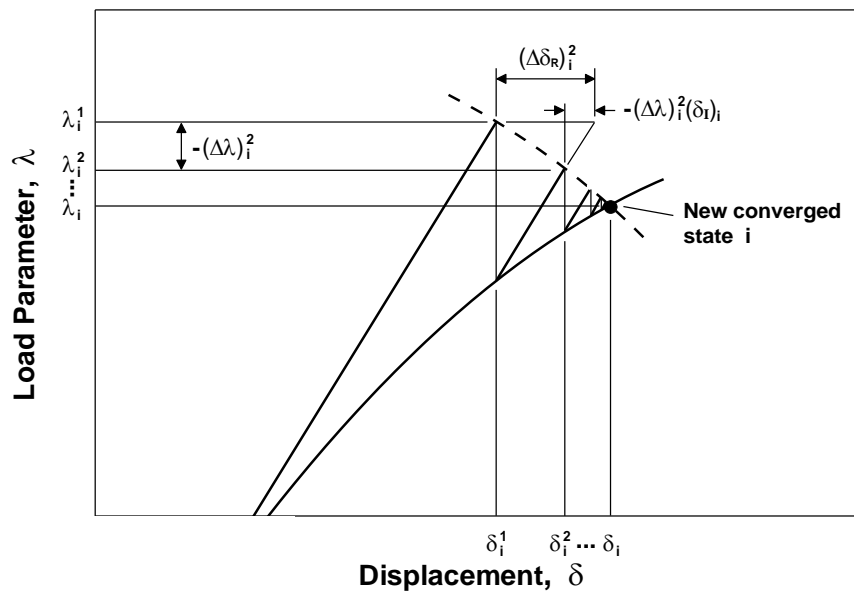


Figure 3.15. Iterative strategy and residual displacements (Clarke and Hancock, 1990).

4. EXPERIMENTAL CALIBRATION AND VALIDATION OF THE MODEL

The model formulation and the nonlinear analysis solution strategy described in the previous chapter were implemented in Matlab for conducting displacement-controlled analysis of actual RC walls, using the proposed finite element modeling approach. This chapter presents information on experimental calibration of the proposed model and detailed comparison of the model results with experimental results obtained from the literature for a relatively slender RC structural wall. Results of the parametric sensitivity studies performed using the proposed model are also presented.

4.1. Description of Experimental Program

For calibration and experimental verification of the analytical model, the rectangular wall specimen RW2 tested by Thomsen and Wallace (1995, 2003) was used. A brief overview of experimental study is provided in this section. More detailed information on the experimental program, can be found in the papers by Thomsen and Wallace (1995, 2003).

The rectangular wall specimen RW2 used for assessment of the model was 3.66 m tall and 102 mm thick, with web length of 1.22 m (Figure 4.1).

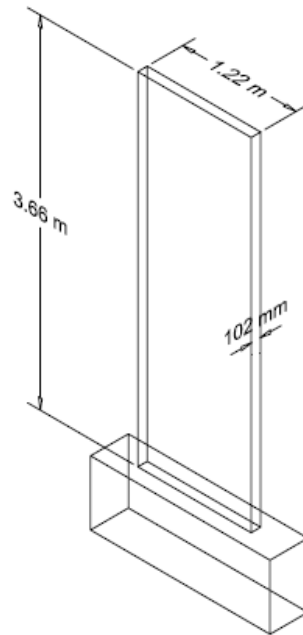


Figure 4.1. RC wall specimen tested by Thomsen and Wallace (1995).

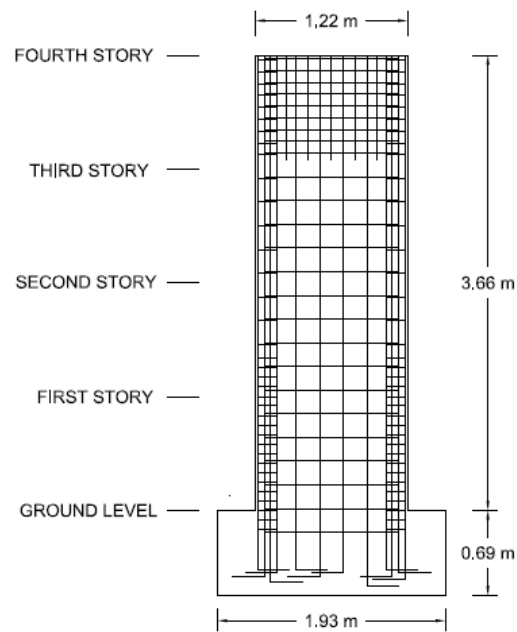


Figure 4.2. Profile view of specimen RW2 showing placement of reinforcement (Thomsen and Wallace, 1995).

At boundaries of the wall specimen, 8 - #3 ($d_b = 9.53$ mm) bars were used while for the web reinforcement #2 ($d_b = 6.35$ mm) bars were uniformly distributed in both transverse and longitudinal directions (Figure 4.3). 4.76 mm annealed smooth wires having the same material properties with #3 and #2 deformed bars were used as transverse reinforcement at wall boundaries.

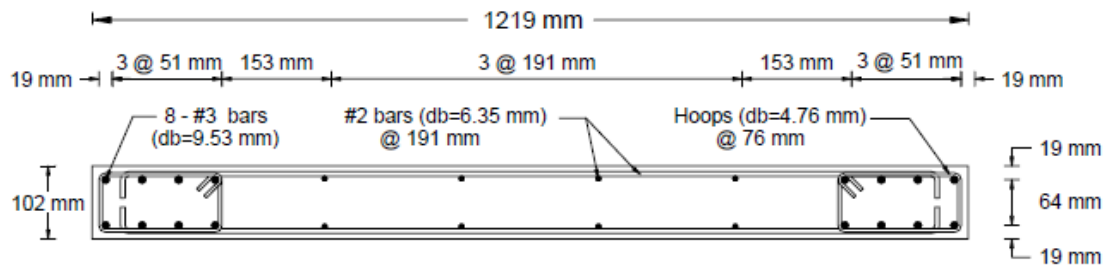


Figure 4.3. Cross-sectional view of the test specimen RW2 (Thomsen and Wallace, 1995).

A prototype building was used for design of the test specimen and strength requirements were taken from Uniform Building Code (1994), whereas a displacement-based design approach presented by Wallace (1994, 1995) was utilized for the detailing requirements at the boundaries of the wall.

During the design of the walls, concrete having the compressive strength of 27 MPa was specified. However, during the testing, measured compressive strengths ranged from 28.7 to 58.4 MPa. For specimen RW2, the mean value of concrete compressive strength was 42.8 MPa. Figure 4.4 displays the concrete stress-strain relationships which were measured via testing standard cylinder specimens having dimensions of 152 mm x 304 mm.

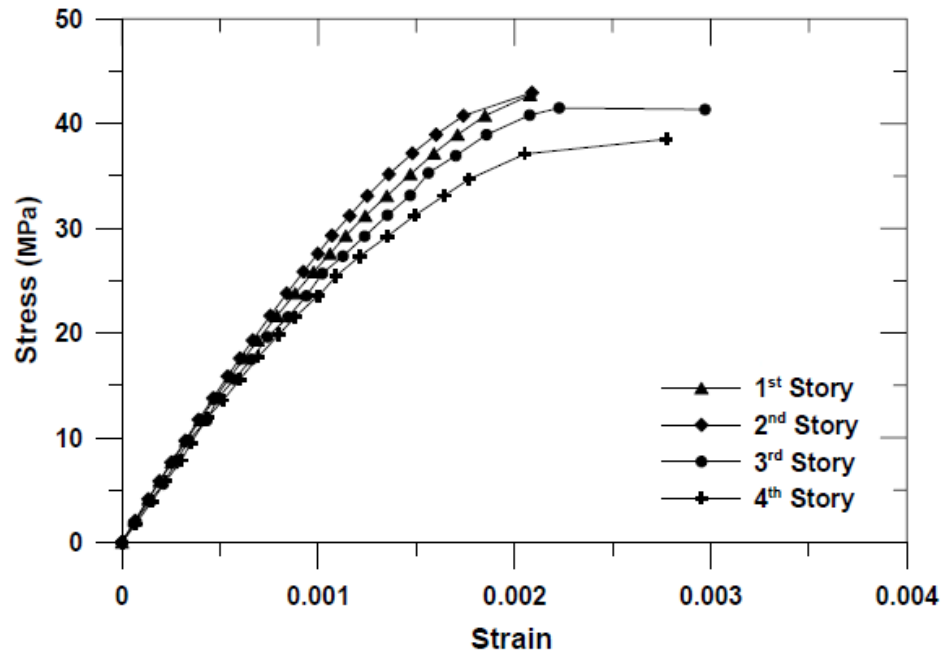


Figure 4.4. Measured concrete stress-strain relationship for RW2 (Thomsen and Wallace, 1995).

Three types of reinforcing steel with different diameters and stress-strain behaviors were used in construction of the wall specimen. The #3 ($d_b = 9.53$ mm) deformed bars used for the longitudinal reinforcement at boundaries had a yield stress of 414 MPa (Grade 60) while the #2 ($d_b = 6.35$ mm) deformed bars used for the longitudinal and transverse reinforcement at the wall web had a yield stress of approximately 448 MPa. On the other hand, the 4.76 mm smooth wire used as the transverse reinforcement at boundaries had a yield stress of approximately 552 MPa, which was later annealed to decrease the yield stress to 448 MPa. Yield strength of these reinforcing steel bars were made similar, while the measured stress-strain behavior of the three types were moderately different (Figure 4.5).

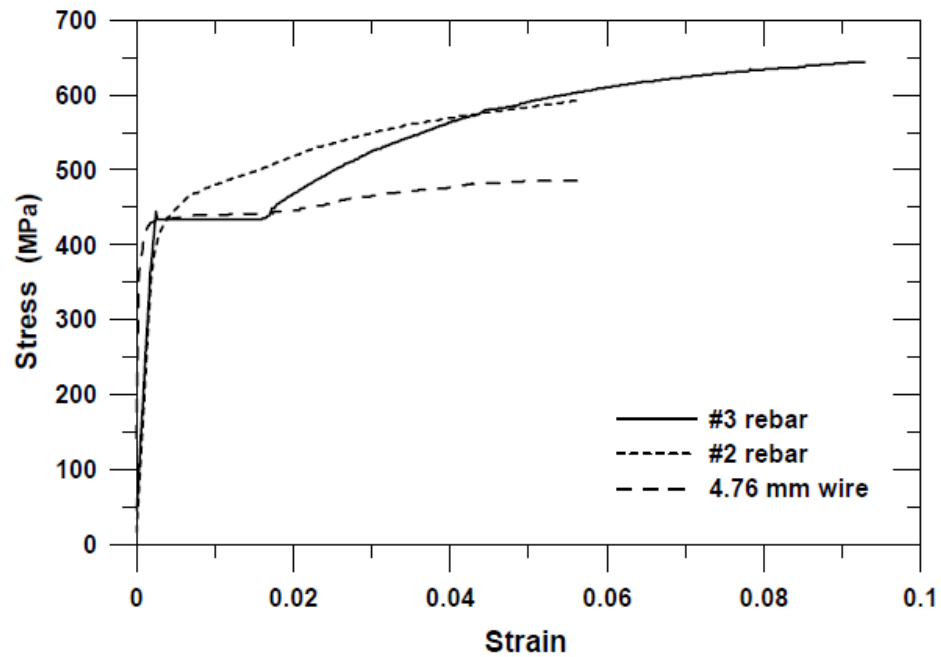


Figure 4.5. Measured reinforcement stress-strain relationship for #3, #2 and 4.76 mm annealed wire (Thomsen and Wallace, 1995).

The wall specimen was tested in an upright position in the Structural Engineering Research Laboratory (SERL) at Clarkson University. A schematic test setup is shown in Figure 4.6. In Figure 4.7, a photograph of the set up is presented. The wall specimen was cast monotonically with a pedestal and 32 mm diameter high-strength steel tie-down rods were used to affix the pedestal rigidly to the strong floor.

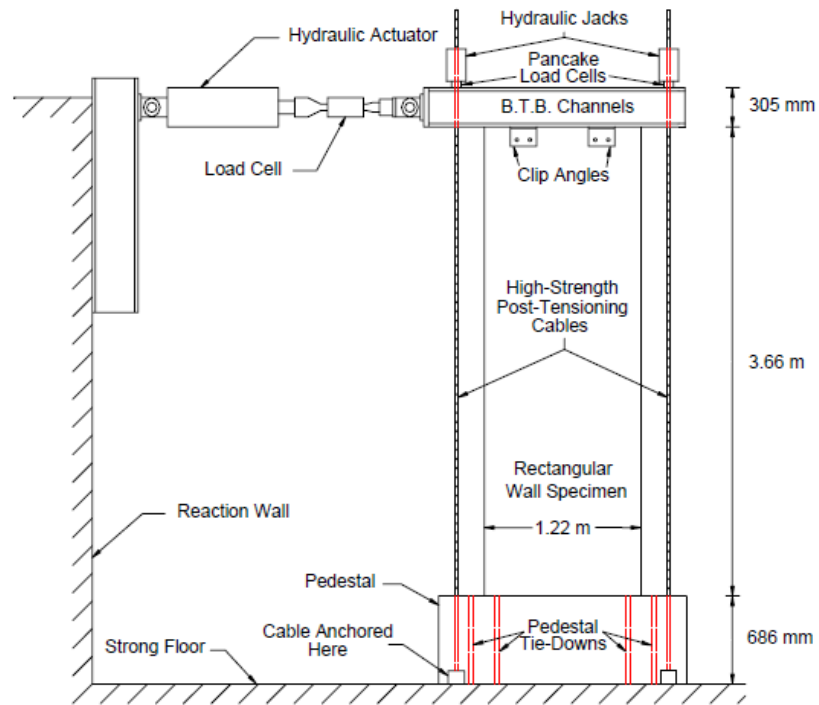


Figure 4.6. Schematic of the test setup (Thomsen and Wallace, 1995).



Figure 4.7. A photograph of the test setup (Thomsen and Wallace, 1995).

In order to transfer the lateral and axial load imposed at the top of the specimen, a specially fabricated steel profile was used. This profile was anchored at the top of the RW2 by using 25 mm diameter rods which had been cast integrally with the fourth story of the specimen. In Figure 4.8, the fabricated profile, together with axial and lateral load setup is shown. An axial stress of approximately $0.10 A_g f'_c$ was maintained throughout the duration of the test. Out-of-plane displacement of the specimen was prevented by using a steel truss system connected to the top of the specimen. Hence, torsional twisting of the wall specimen was also prevented.

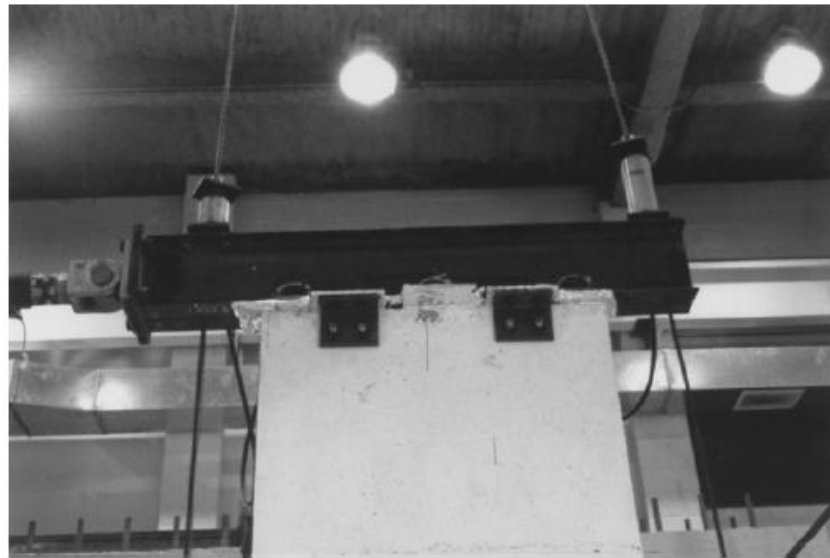


Figure 4.8. A photograph of load transfer assembly (Thomsen and Wallace, 1995).

As shown in Figure 4.9, an extensive instrumentation setup was used to measure displacements, loads, and strains at critical locations for the wall specimen. In order to measure displacements for each loading step, wire potentiometers, linear potentiometers, and linear variable differential transducers (LVDTs) were used while load cells were used to measure axial and lateral loads, and strain gauges were used to measure strains in the concrete and the reinforcing steel. To observe the pedestal slip from the ground level, linear potentiometer placed horizontally were used, while two vertical potentiometers were utilized to measure vertical displacement of the pedestal (Figure 4.10).

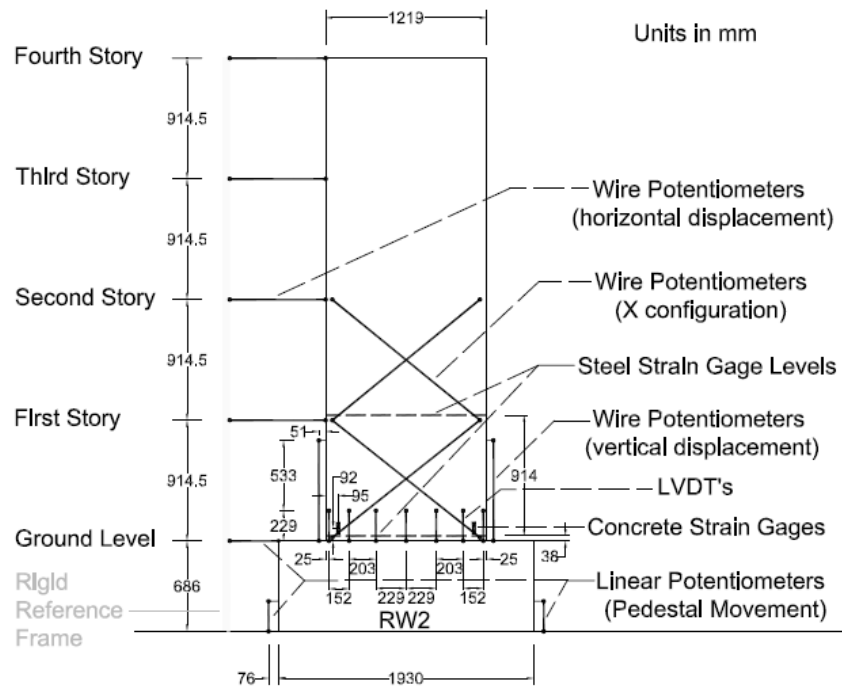


Figure 4.9. Instrumentation on RW2.

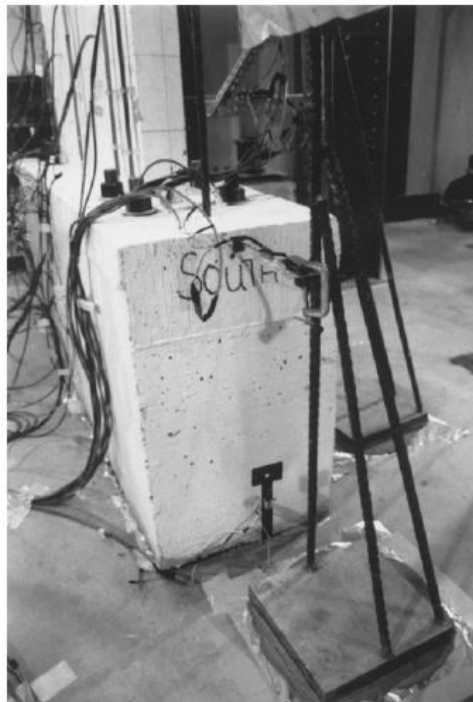


Figure 4.10. A photograph of instrumentation used to measure pedestal movement (Thomsen and Wallace, 1995).

Figure 4.11 shows the wire potentiometers used to measure shear deformations on the specimen. These wire potentiometers were placed in an X configuration. Besides, two vertical wire potentiometers placed at the boundaries of the specimen were used to measure flexural rotations (Figure 4.9).

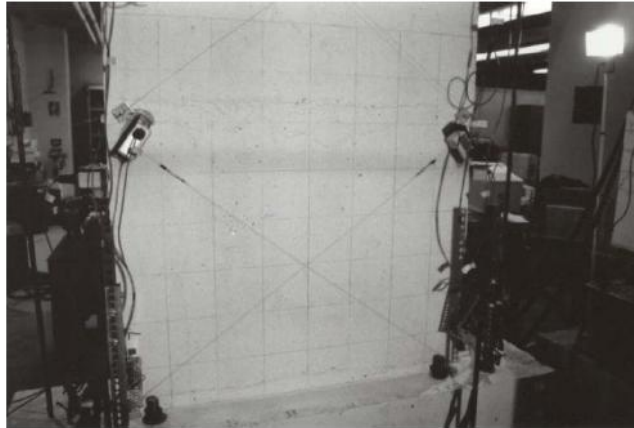


Figure 4.11. A photograph wire potentiometers used to measure shear deformations (Thomsen and Wallace, 1995).

After the experimental setup was prepared, testing of the specimen started with applying axial load, which continued until reaching the specified axial load (approximately $0.10 A_g f'_c$). Load cells and pressure gages were used to monitor the axial load history on the specimen, which was applied using hand pumps. After reaching the specified axial load, drift-controlled reversed-cyclic loads were applied on the specimen. A total of 20 full cycles were performed during the test (Figure 4.12).

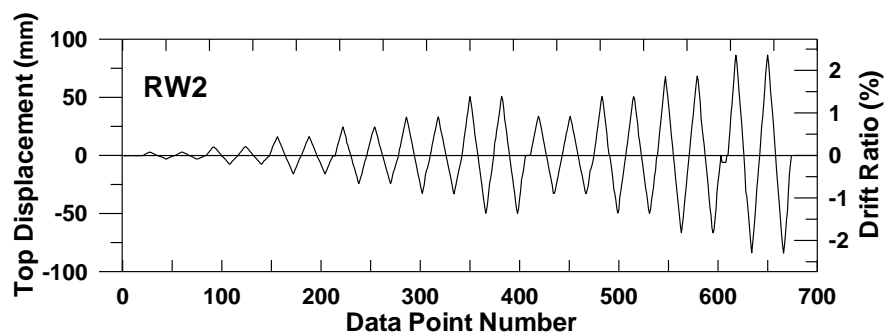


Figure 4.12. Lateral drift history for specimen RW2.

4.2. Model Calibration

The analytical model proposed in this study was calibrated to represent the geometric properties, reinforcement amount, and material characteristics of wall specimen RW2. Calibration of the analytical model consists of two processes: calibration of the model geometry and calibration of the constitutive material model parameters. In this section, details of the calibration process are presented.

As shown in Figure 4.13, in the model formulation, specimen RW2 was divided into 6 segments ($m=6$) in horizontal direction and into 20 segments ($n=20$) in the vertical direction, resulting in a total of 120 rectangular model elements. The criteria for model discretization was to make the model elements have approximately equal width and height, and capture the locations where displacement sensors were attached for measurement of local deformations, so that model results can be compared with test measurements also at local response levels.

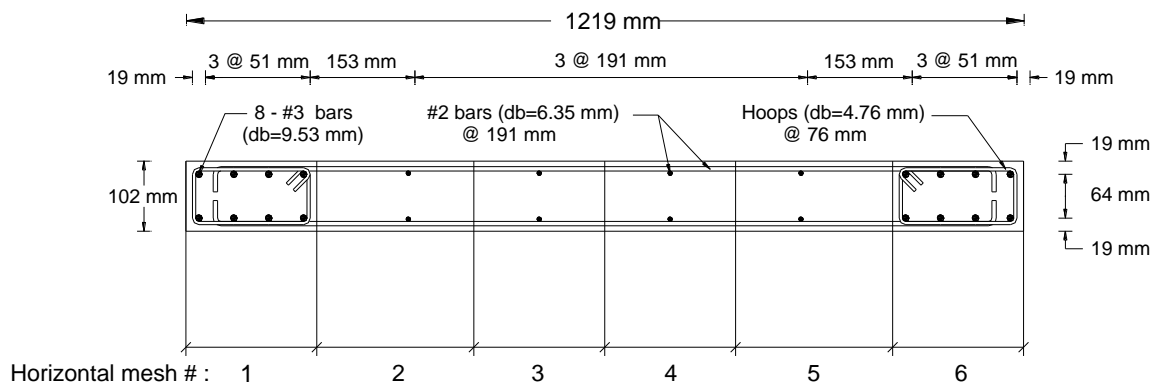


Figure 4.13. Geometric calibration for specimen RW2.

Material calibration was performed by calibration of the constitutive model parameters for concrete and reinforcing. For the reinforcing steel stress-strain relationship, the Menegotto and Pinto (1977) was calibrated to represent experimentally-observed results for the reinforcing bars (Figure 4.14). Depending on the test results conducted on the #3 ($d_b = 9.53$ mm) and #2 ($d_b = 6.35$ mm) deformed bars, a modulus of elasticity $E_c =$

200 GPa was determined. Tensile yield strengths of $\sigma_y = 434$ MPa and $\sigma_y = 448$ MPa, and a strain-hardening ratio of $b = 0.02$ were assigned for the bare #3 and #2 bars, respectively. These parameters were used to define the compression behavior of reinforcing steel bars. However, for tension, the yield strength (σ_y) and strain-hardening (b) parameters were modified to include the effects of tension stiffening based on the empirical relation proposed by Belarbi and Hsu (1994).

For the calibration of cyclic Bauschinger's effect parameters in the constitutive model for reinforcing steel, namely parameters, R_0 , a_1 , and a_2 , previous recommendations were used. Values of $R_0 = 20$, $a_1 = 18.5$, $a_2 = 0.0015$ were assigned to the parameters, as recommended by Elmorsi *et al.* (1998) were assigned.

As shown in Figure 4.15, the Chang and Mander (1994) model was calibrated to represent the experimentally-measured behavior of concrete cylinder samples. Concrete compressive strength of $f'_c = 42.8$ MPa was assigned, at the compressive strain value of $\varepsilon'_c = 0.0021$. The initial tangent modulus (elastic modulus) of concrete was assigned a value of $E_c = 31026$ MPa. In the compression zone, parameter r , which is used for determining the shape of envelope curve, is assigned a value equal to 7.0. Concrete tensile strength f_t was calculated as 2.03 MPa, based on Equation 4.1. Tensile strain value at peak monotonic tensile stress was set equal to $\varepsilon_t = 0.00008$. The initial tangent modulus in tension was selected to be the same as in compression, which was $E_c = 31026$ MPa. Unlike the compression envelope, the r value for tension was set equal to 1.2, to represent the effects of tension stiffening in the shape of tension envelope curve, as proposed by Belarbi and Hsu (1994),

$$f_t = 0.31\sqrt{f'_c} \quad (4.1.)$$

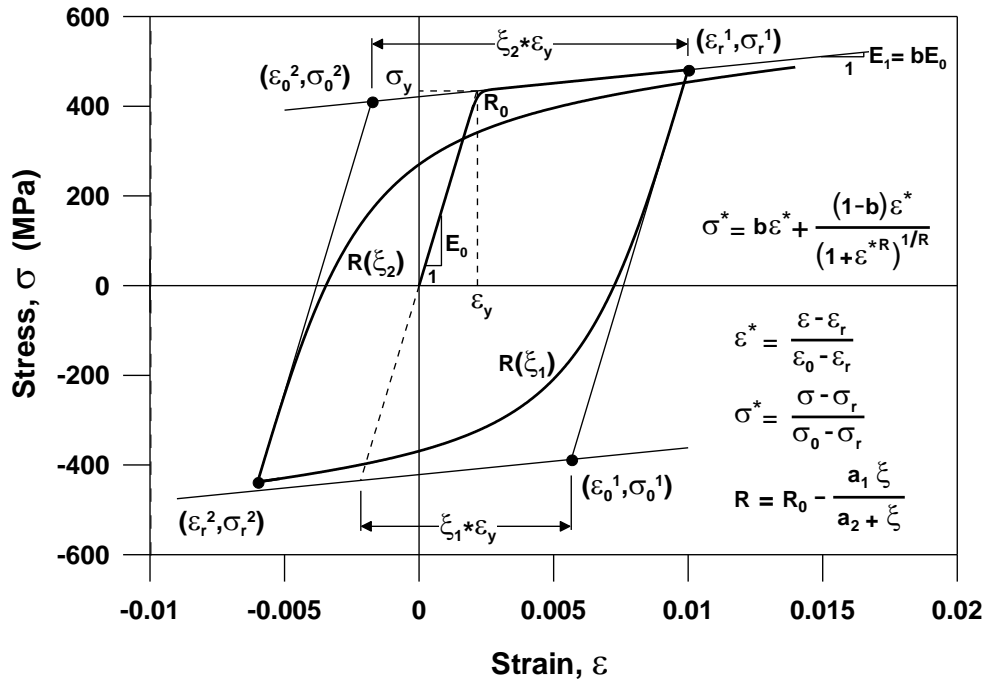


Figure 4.14. Constitutive material model for reinforcing steel and parameters for calibration (Orakcal, 2004).

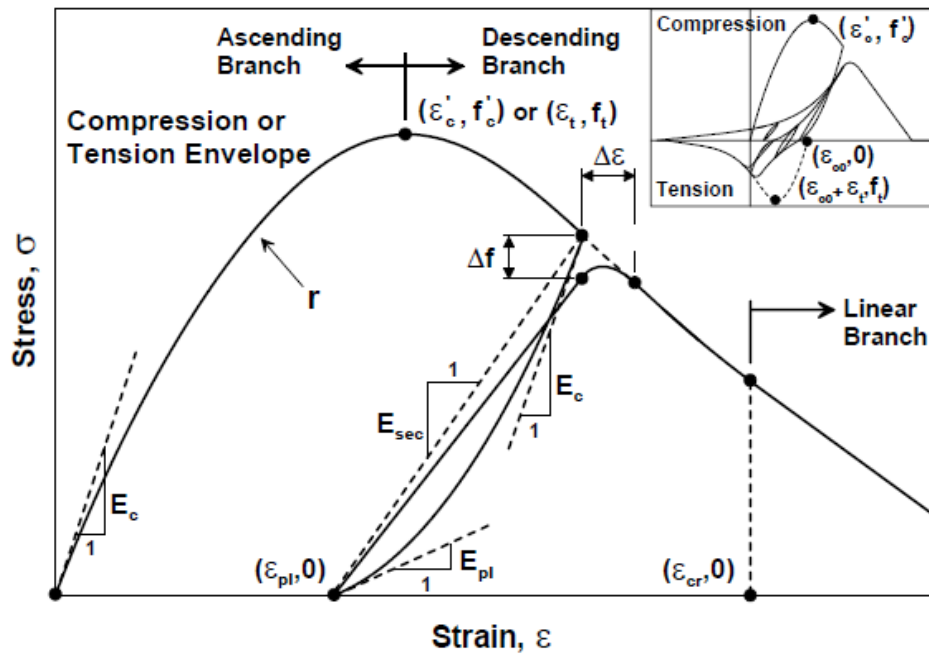


Figure 4.15. Constitutive material model for concrete and parameters for calibration (Orakcal, 2004).

Confined concrete in the boundary regions was calibrated based on the confinement model by Mander *et al.* (1988). As shown in Figure 4.16, in order to observe the consistency in considering the confinement effect, the model by Mander *et al.* (1998) was compared with the confinement model by Saatcioglu and Ravzi (1992). An overall summary of the calibrated constitutive material parameters is presented in Table 4.1 and Table 4.2 for concrete and reinforcing steel bars, respectively.

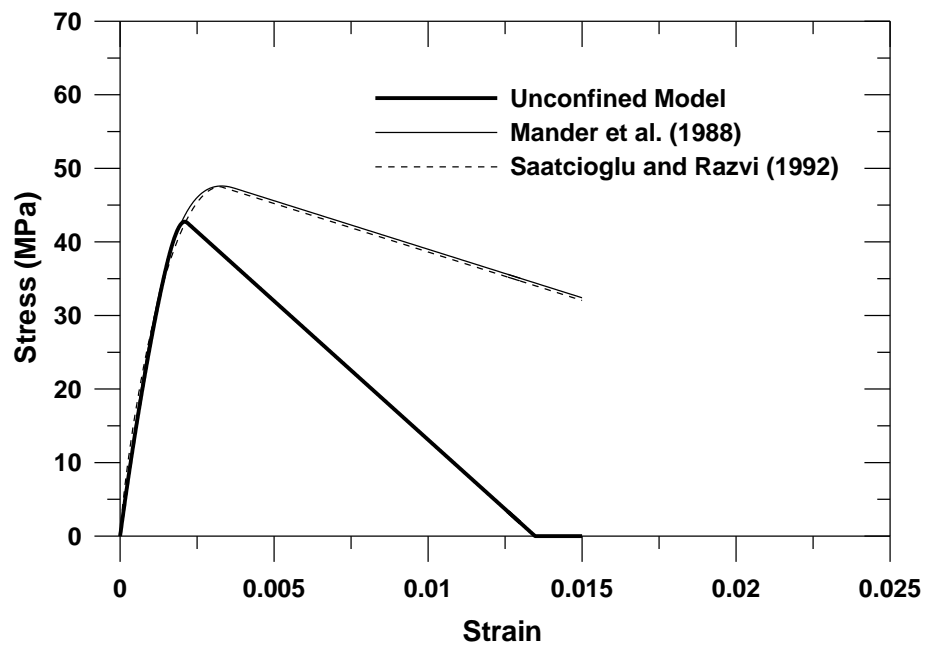


Figure 4.16. Comparison of the confinement models.

Table 4.1. Calibrated constitutive parameters for concrete.

Concrete in Compression			Concrete in Tension	
Parameter	Boundary (Confined)	Web (Unconfined)	Parameter	Boundary & Web (Confined & Unconfined)
f_c' (Mpa)	47.6	42.8	f_t (Mpa)	2.03
E_c (MPa)	31026	31026	E_t (MPa)	31026
ϵ_c'	0.0033	0.0021	ϵ_t	0.00008
ϵ_{cr}	0.0037	0.0022	ϵ_{cr}	∞
r	1.90	7.00	r	1.2

Table 4.2. Calibrated constitutive parameter for reinforcing steel.

Rebar in Compression			Rebar in Tension		
Parameter	#3 Rebar	#2 Rebar	Parameter	#3 Rebar	#2 Rebar
σ_y (MPa)	434	448	σ_y (MPa)	395	336
E_0 (MPa)	200000	200000	E_0 (MPa)	200000	200000
b	0.02	0.02	b	0.0185	0.035

Compression softening effects were taken into account based on the model parameters proposed by Vecchio and Collins (1993), as presented in Section 2.3.3. The biaxial damage formulation proposed by Mansour and Hsu (2002) was implemented into Fixed Strut Angle Model for the simulation of the biaxial damage effects, as mentioned in Section 2.3.5. The shear aggregate interlock model explained in Section 2.3.6 was also incorporated in the calibration. The linear unloading/reloading slope of the interlock shear stress-strain relationship along the cracks was taken as $0.4E_c$, and a value of 1.1 was used for the friction coefficient.

4.3. Model Results and Comparison with Experimental Results of Specimen RW2

The calibrated analytical model implemented in Matlab was used to compare the experimentally-observed results with analytical model predictions. As explained in Section 4.1, the instrumentation setup established during the tests allowed local deformation measurements at various locations on the wall specimen, which were also compared with analytical model results. Analysis of the specimen RW2 was performed with the calibrated parameters defined in the previous section to validate the accuracy of the analytical model. The analysis was conducted using the displacement-controlled nonlinear analysis solution strategy described previously. The top displacement history applied to the wall specimen, included unwanted displacement components resulting from sliding and uplift of the pedestal. Hence, the analytical model was subjected to a corrected top displacement history, which was processed by subtracting the unwanted pedestal displacement effects (Figure 4.17). After applying the modified top displacement history to the analytical model, comparison of the experimentally-measured and analytically-predicted lateral load

vs. top displacement response of the wall specimen is presented in Figure 4.18. The nominal lateral drift levels listed in Table 4.3, which corresponded to peak points of each lateral drift level, were used for local deformation (e.g., concrete strain profile) comparisons.

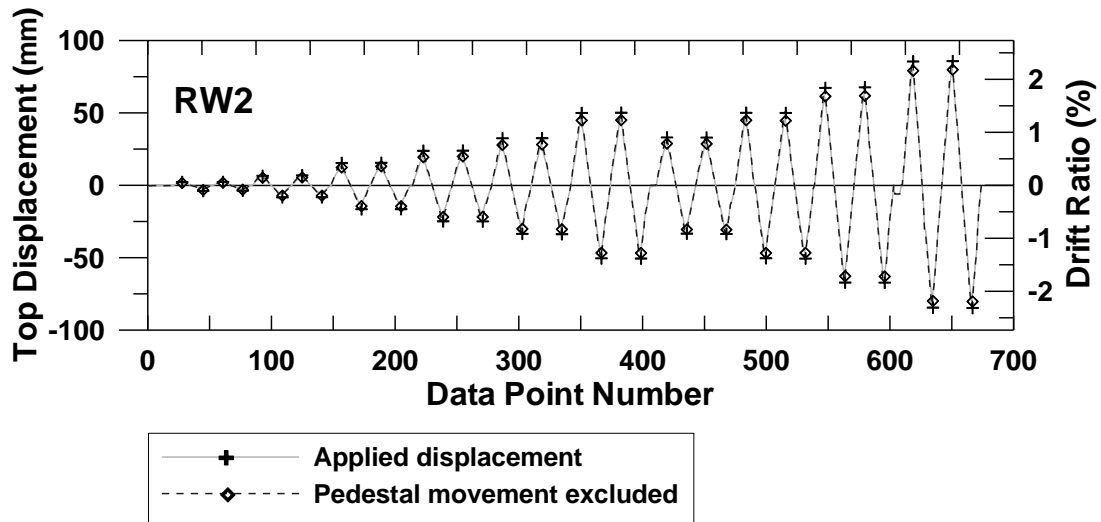


Figure 4.17. Comparison of applied and corrected drift histories for specimen RW2.

Table 4.3. Lateral displacement values at peak drift points for specimen RW2.

Load Direction	Load Type	Lateral Drift (%)							
		0.10%	0.25%	0.50%	0.75%	1.00%	1.50%	2.00%	2.50%
Positive	Top displacement applied during testing (mm)	2.9	7.2	16.1	24.5	33.1	50.6	67.9	86.2
	Top displacement with pedestal movement contribution subtracted (mm)	2.3	5.9	13.0	20.1	28.5	45.5	62.1	79.8
Negative	Top displacement applied during testing (mm)	-3.2	-7.6	-15.9	-24.2	-32.8	-49.8	-66.5	-83.8
	Top displacement with pedestal movement contribution subtracted (mm)	-2.6	-6.5	-13.7	-21.2	-29.4	-46.0	-62.1	-79.2

The finite element model captures, with reasonable accuracy, the experimentally-observed lateral load-displacement response of specimen RW2 (Figure 4.18). The analysis

was conducted by applying the corrected top displacement history under a constant axial force of 378 kN. The analytically-predicted lateral load vs. displacement response reasonably represents the experimentally-observed cyclic response characteristics of the wall, including lateral load capacity, stiffness degradation, hysteretic shape, plastic (residual) displacements, ductility, and pinching behavior. Overall, the analytical model provides an accurate prediction of the global lateral load behavior of the wall specimen.

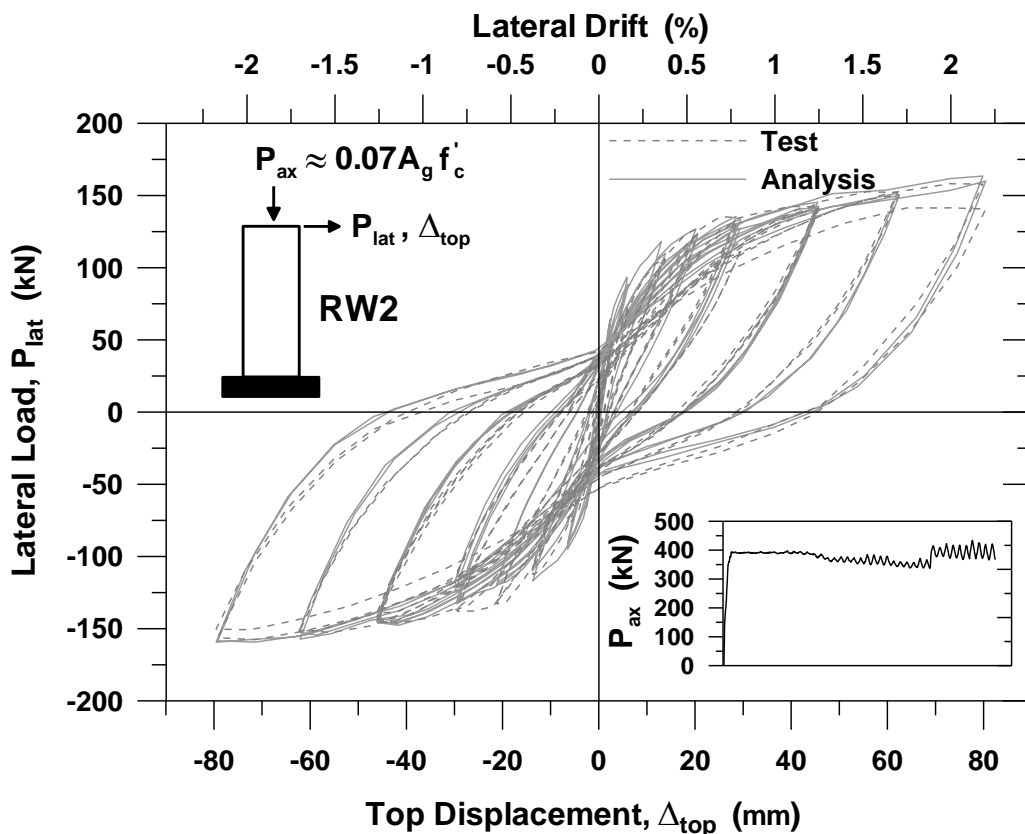


Figure 4.18. Comparison of the measured and calculated lateral load vs. displacement responses for wall specimen RW2.

Figure 4.19 presents the comparison of the experimental and analytical lateral displacement profiles of the wall, which were recorded during the test using WPs connected to the specimen at story levels. It must be mentioned that the results compared here are the corrected lateral displacement magnitudes, meaning pedestal movement contributions were subtracted. In the positive loading direction, the model gives reasonable results at the drift levels of 1.5%, 2.0% and 2.5%, whereas in the negative direction, model

predictions are more accurate at the drift levels smaller than 2.0%. Overall, the model adequately represents the distribution of lateral displacements along wall height, and concentration of nonlinear deformations along the first story height of the wall.

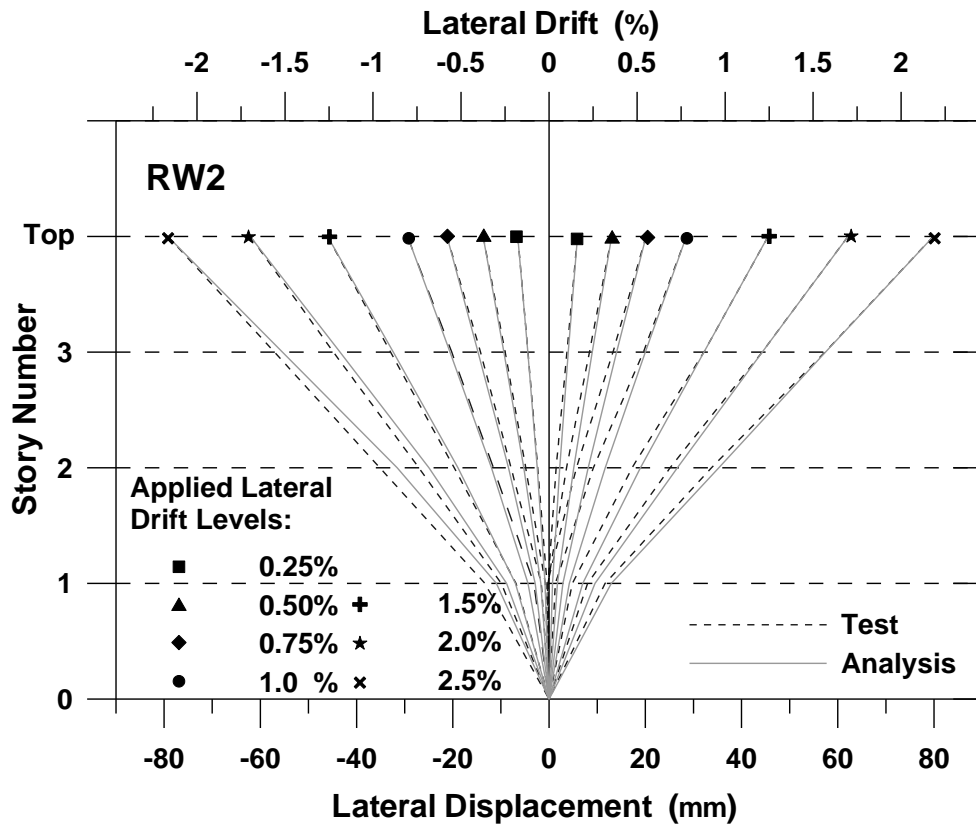


Figure 4.19. Comparison of the measured and predicted lateral displacement profiles.

Figure 4.20 compares the analytically-calculated lateral displacement and rotation time histories developing along the first story height of the wall, with the experimental measurements. In the test results, rotations over the first story were calculated by dividing the relative displacements at the end points of the wire potentiometers attached to the boundaries of the specimen by the distance between the potentiometers. The analytical predictions are accurate enough to state that the analytical model reasonably predicts the nonlinear deformations developing within plastic hinge zone of the wall.

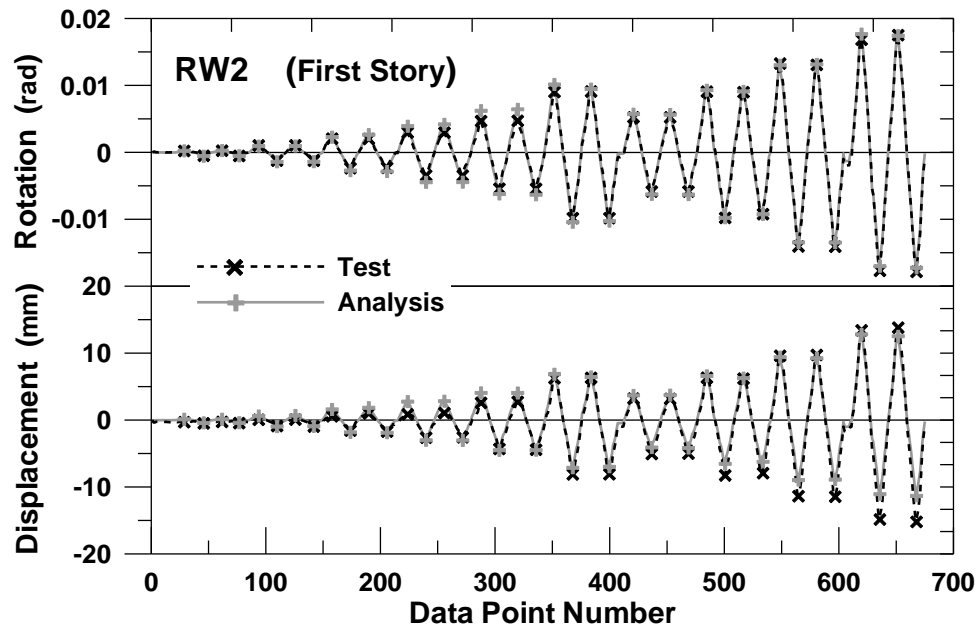


Figure 4.20. Comparison of measured and predicted lateral displacement and rotation time histories at the first story level.

Figures 4.21 and 4.22 compare the measured and predicted concrete strain values at specific locations and at peak points corresponding to selected drift levels. The measurements were obtained from the seven linear variable differential transducers (LVDTs) mounted at the base of the specimen, as shown in Figure 4.9. While evaluating the analytical results, obtained vertical displacement values at model DOFs were divided by the vertical length of the model elements to calculate the average strain values. Results were compared at peak drift levels shown in Figures 4.21 and 4.22. As revealed in the comparisons, average concrete profiles are similar especially in the tensile region of the wall cross-section. As can be obviously seen in the figure, unlike in fiber models, plane sections do not necessarily remain plane in the implemented FEM, which is more consistent with the experimentally-measured strain profiles. Accurate predictions are also obtained with the model for the depth of the neutral axis. In the compression region of the wall cross-section, the model seems to underestimate average compressive strains in concrete. This may be due to the fact that the LVDTs used to measure these strains were affixed to wooden blocks glued to the surface of the wall. Therefore, the experimental measurements may not reliably represent the compressive strains experienced by the

confined core concrete in the boundary regions. Similar results were obtained for this specimen, using fiber modeling approaches.

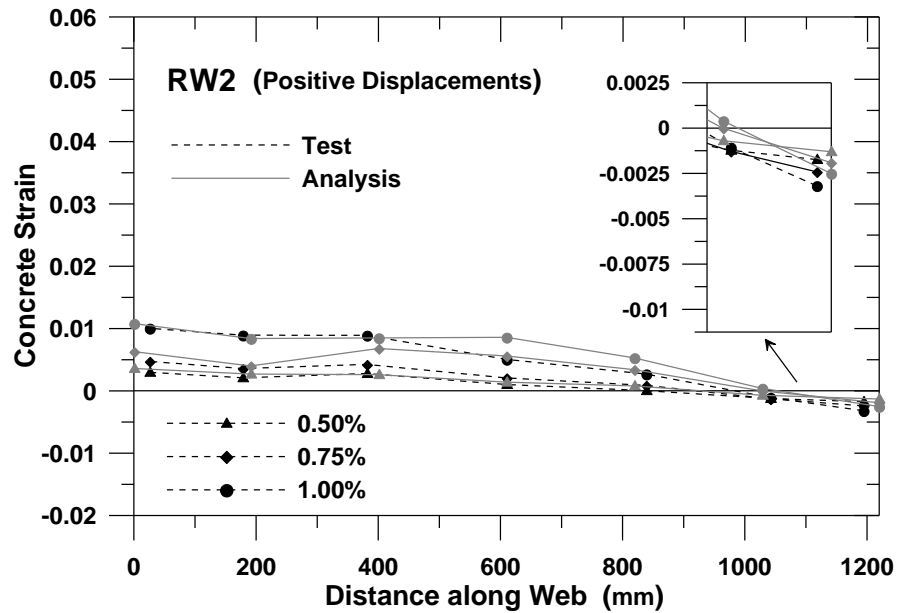


Figure 4.21. Comparison of the average concrete strain profiles along wall length at small drift levels.

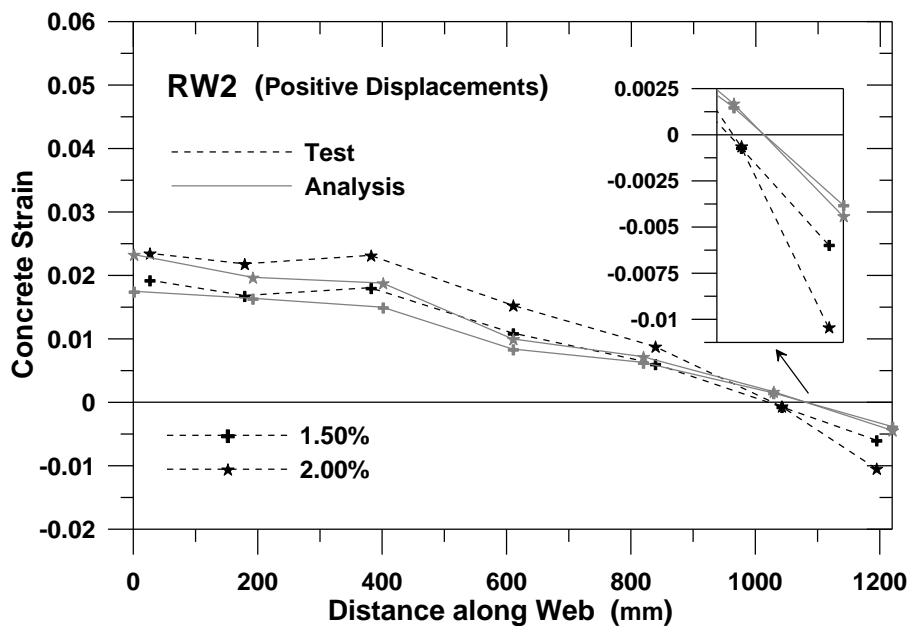


Figure 4.22. Comparison of the average concrete strain profiles along wall length at large drift levels.

Figures 4.23 and 4.24 show the comparison of the measured and predicted average strain histories in the vertical direction at the two boundaries (north and south) at the base of the wall specimen. Again, the test data was recorded by the LVDTs mounted at the base of the wall. As discussed for Figures 4.21 and 4.22, the analytical model accurately captures the average tensile strains in concrete, but underestimates compressive strains to as low as approximately half of measured values. However, reasonable compressive strain predictions are obtained at earlier stages during loading, corresponding to smaller drift levels. As well, as discussed later in Section 4.4, compressive strain predictions of the model may be influenced by the number of model elements used along the height of the wall, possibly resulting in improved correlations between analytical and experimental results.

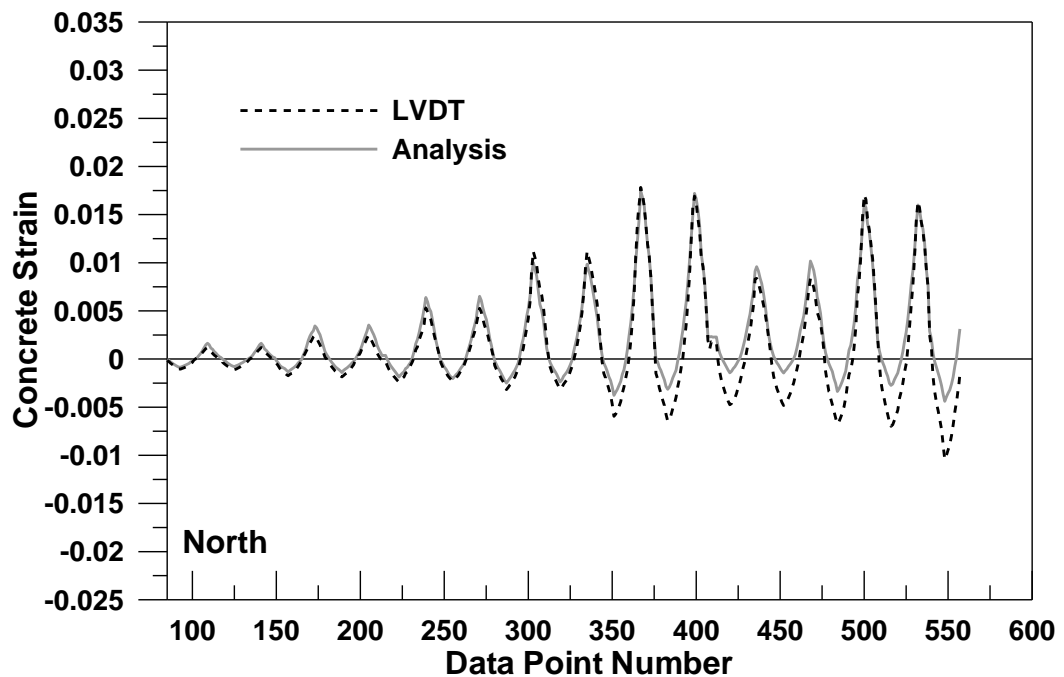


Figure 4.23. Comparison of the vertical strain histories at the north boundary of the wall at base level.

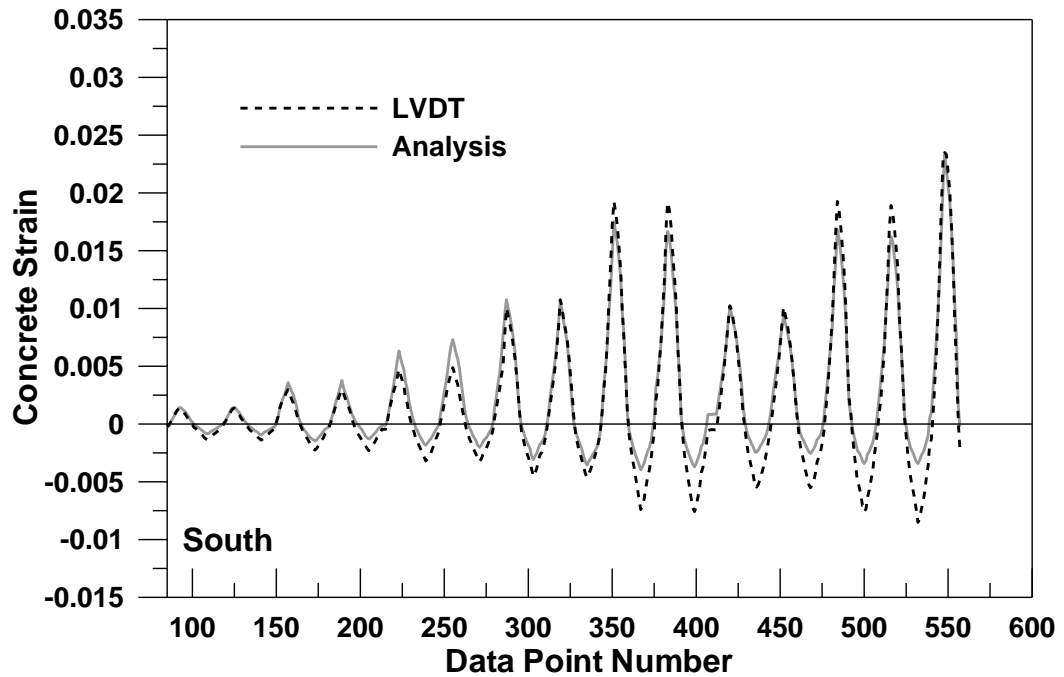


Figure 4.24. Comparison of the vertical strain histories at the south boundary of the wall at base level.

Shear distortion of the wall specimen RW2 was measured along the first and second story heights, by using diagonally-mounted wire potentiometers. Wire potentiometers were mounted as shown in Figure 4.9, in an X configuration along the first and second stories of the specimen. Based on measurements of these sensors and using the procedure proposed by Thomsen and Wallace (1995), shear distortions along the first and second stories of the wall were calculated and compared with the model predictions. Measured and predicted lateral load vs. shear distortion responses along the first and second story heights of the specimen are compared in Figures 4.25 and 4.26. In the analytical model results, significant nonlinear shear deformation response was observed along the first story, similarly to the experimental results; however, maximum shear deformation values were underestimated (Figure 4.25). It is anticipated that improving the shear aggregate interlock model in future studies will help capture the measured maximum shear deformation values.

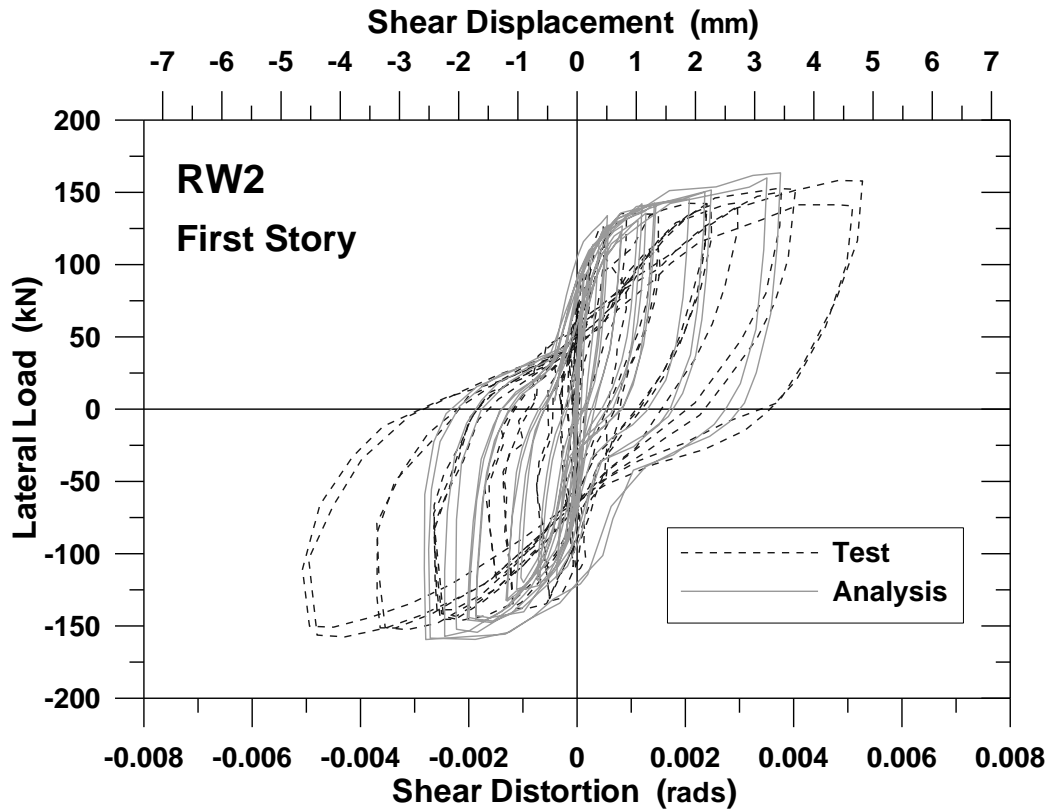


Figure 4.25. Comparison of measured and predicted lateral load vs. first story shear deformation responses.

Figure 4.26 compares the shear deformation responses along the second story. In both analytical and experimental results, the lateral load vs. shear distortion response along the second story is more linear elastic in nature, with considerably smaller deformations compared to the first story. The analytical model reasonably captured the experimentally-observed shear deformations in the second story. The shear stiffness characteristics were not duplicates; however, they showed similar trends. Since shear deformations along the third and fourth stories of the wall were not experimentally measured, shear response comparisons could not be made in these regions.

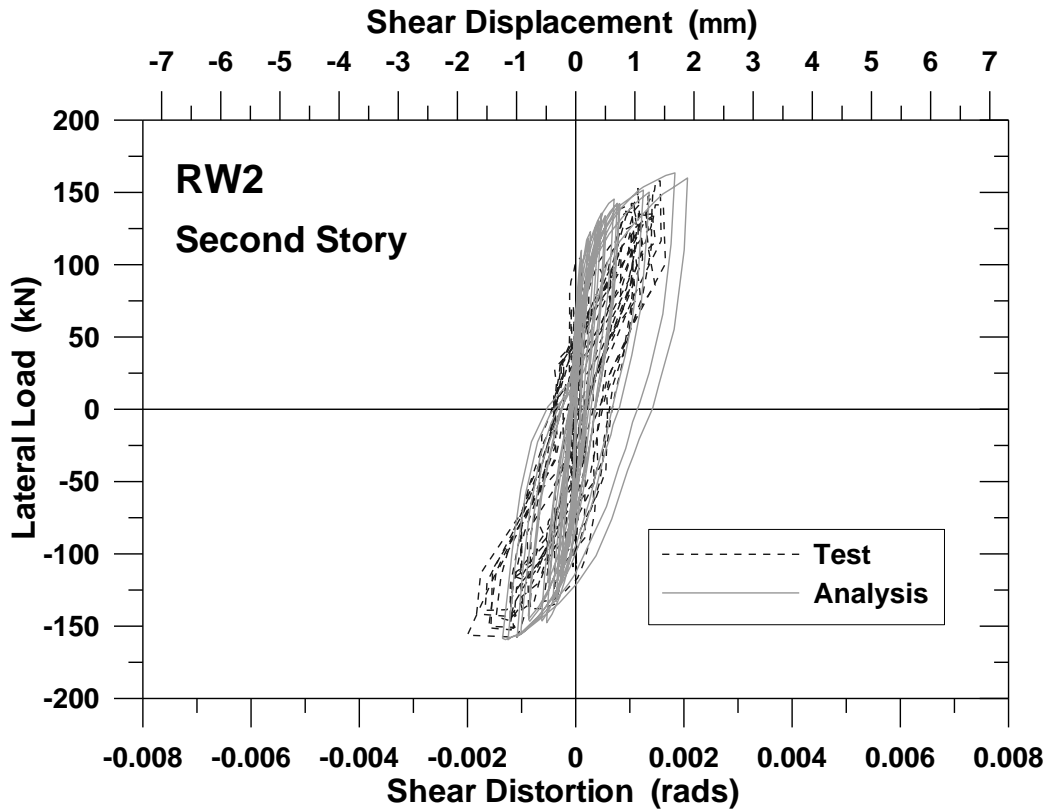


Figure 4.26. Comparison of measured and predicted lateral load vs. second story shear deformation responses.

However, Figure 4.27 compares only the analytically-predicted shear deformation responses obtained along all four stories of the wall specimen. As can be observed in the analytical results, shear deformation magnitudes decrease from the bottom to the top floors of the wall. The first story experiences the most nonlinear shear response, while the response along the second story shows less nonlinearity, and third and fourth stories demonstrate almost linear elastic responses. Significant nonlinearity in the shear response of the first story implies that shear yielding and nonlinear shear deformations in the wall were concentrated along the plastic hinge region of the wall, where nonlinear flexural deformations are also concentrated. This demonstrates the model's capability of capturing shear-flexure interaction effects even in a relatively slender wall, and coupling of nonlinear shear and flexural deformations throughout the cyclic loading history. This is a significant advantage of the finite element modeling approach proposed in this study, over conventional fiber models that do not consider coupling of shear and flexural responses.

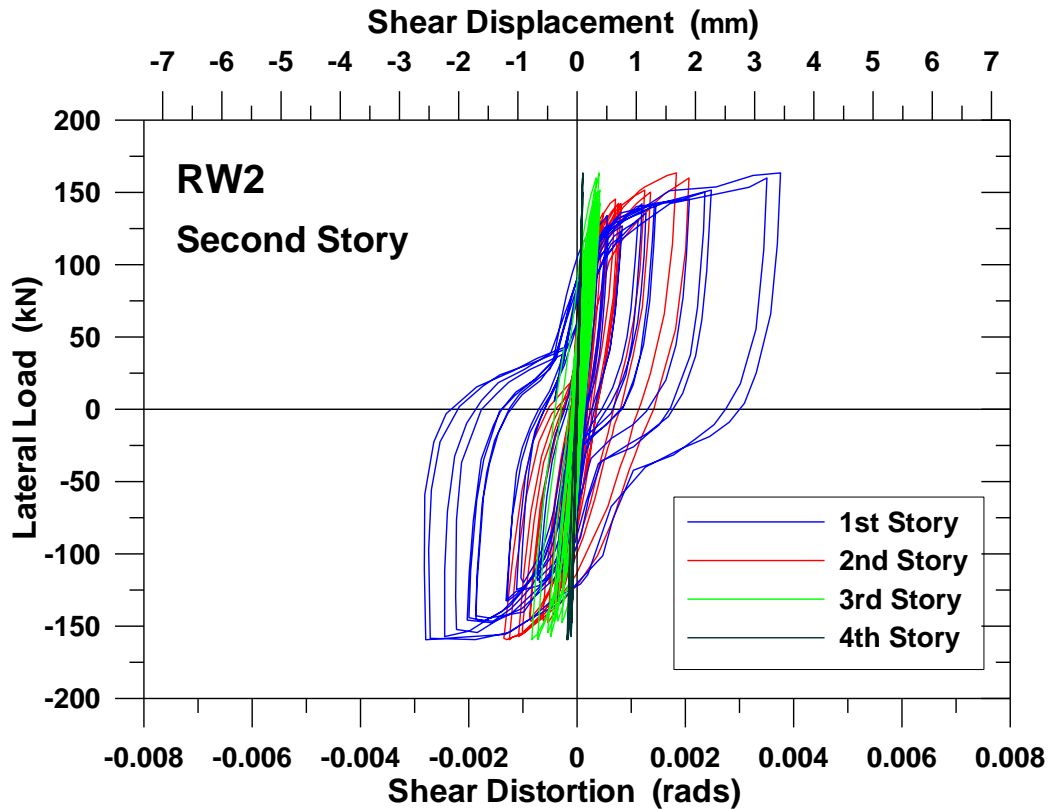


Figure 4.27. Comparison of analytical lateral load vs. story shear deformation responses.

4.4. Parametric Sensitivity Studies

Within the scope of this study, parametric studies were also performed to investigate the sensitivity of the model results to important parameters related to the response of structural walls. Parametric sensitivity studies were conducted for the number of model elements used along the height of a wall, the wall aspect ratio, the axial load level applied on the wall, and the web reinforcement ratio of a wall.

In the first sensitivity study, the number of model elements (n) used along the height of the wall specimen RW2 was modified. Analytical results were obtained for three different n values of 12, 20, and 36. 20 model elements were used in calibration of the original model used in Section 4.3. The analytical lateral load vs. top displacement responses obtained for the three different n values are compared in Figure 4.28. As shown in the figure, using a different number of model elements along wall height does not significantly influence the global response prediction of the analytical model, as long as a

reasonable number of model elements are used. However, this may not necessarily be the case for the local deformation predictions, as depicted in Figure 4.29. Figure 4.29 compares of the analytical average strain histories in the vertical direction at the boundary of the wall specimen at the base, for the three different n values. As shown in the figure, the average tensile strains are not significantly sensitive to the number of model elements used along the height of the wall, which is a positive aspect since the tensile strains were predicted accurately by the original model configuration. On the other hand, the compressive strain predictions, which were underestimated by the original model, are considerably different when 36 model elements are used along wall height. This indicates that compressive strain predictions of the model are sensitive to the number of model elements, which is promising for obtaining improved compressive strain predictions with a more refined analytical model configuration.

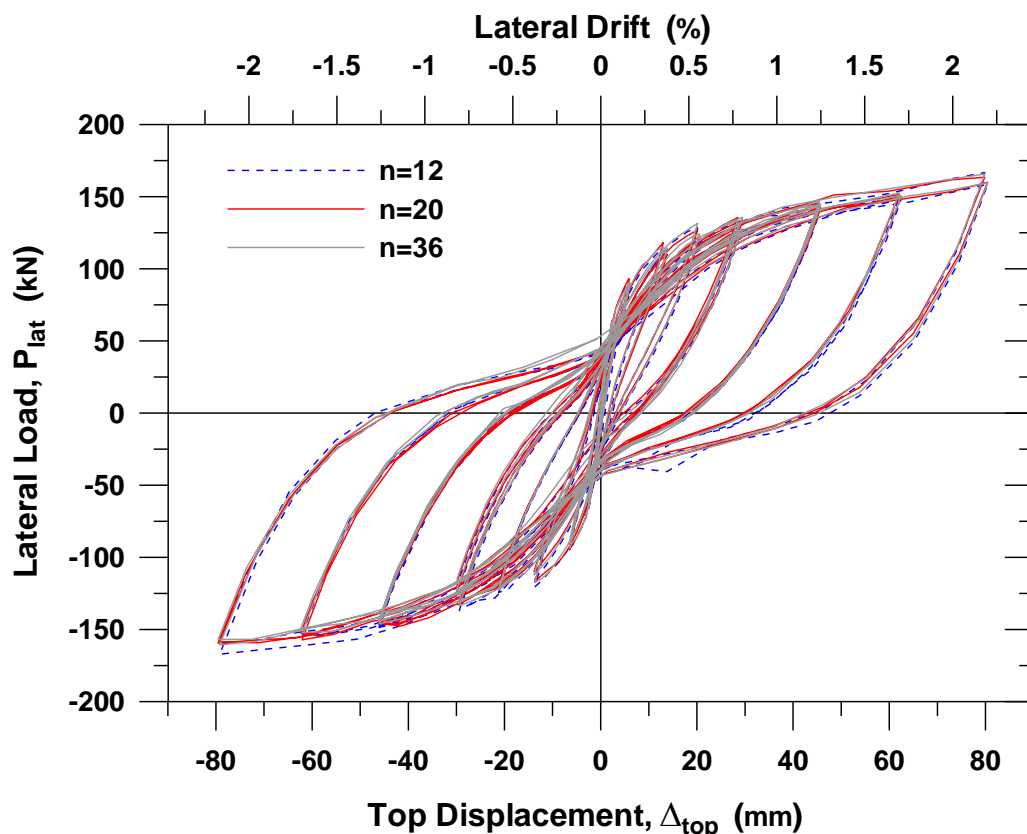


Figure 4.28. Analytical lateral load vs. top displacement responses for different n values.

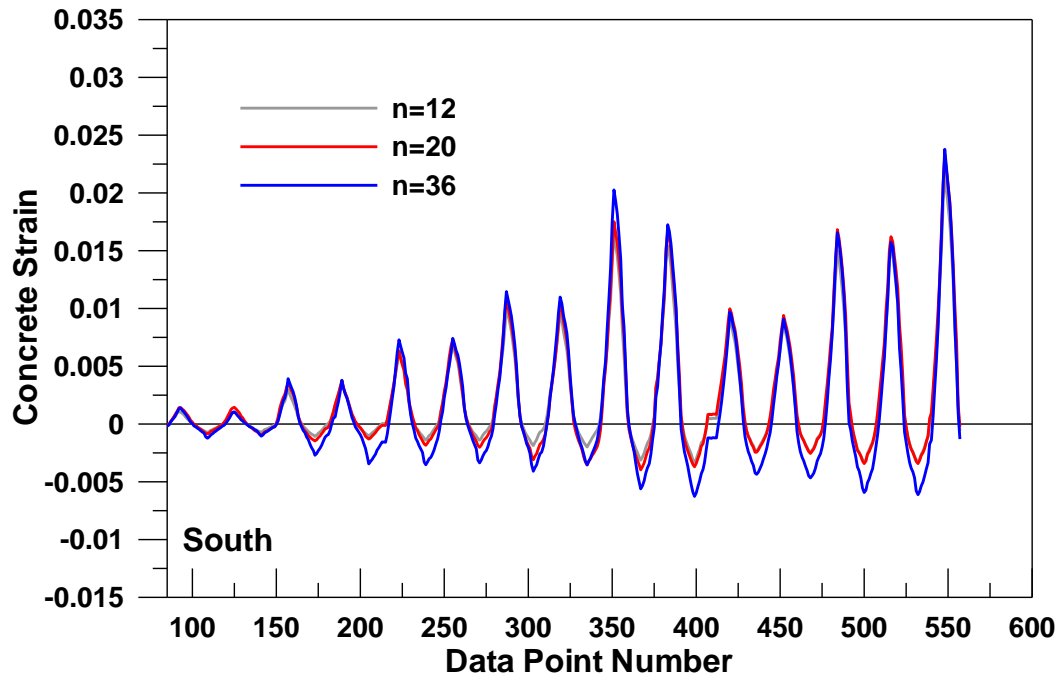


Figure 4.29. Analytical vertical strain histories at the boundary of the wall at base level for different n values.

Changing the aspect ratio, which is the height-over-width ratio of the wall, is the second parametric study that was conducted to assess the sensitivity of the proposed model. Figures 4.30 and 4.31 show the influence of different wall aspect ratios on the analytical lateral load vs. displacement response of the wall. As can be observed in the figures, smaller aspect ratios result in global load-displacement responses with increased lateral load capacity and stiffness. However, a very small aspect ratio such as 1.0 changes the predicted response of the wall from the ductile flexural-dominated behavior that is typical of slender walls, into a brittle shear-dominated behavior (with significant strength degradation at low drift levels) expected for low-rise walls. Comparison of the results demonstrates that the proposed analytical model capable of simulating different modes of behavior based on the aspect ratio of a wall.

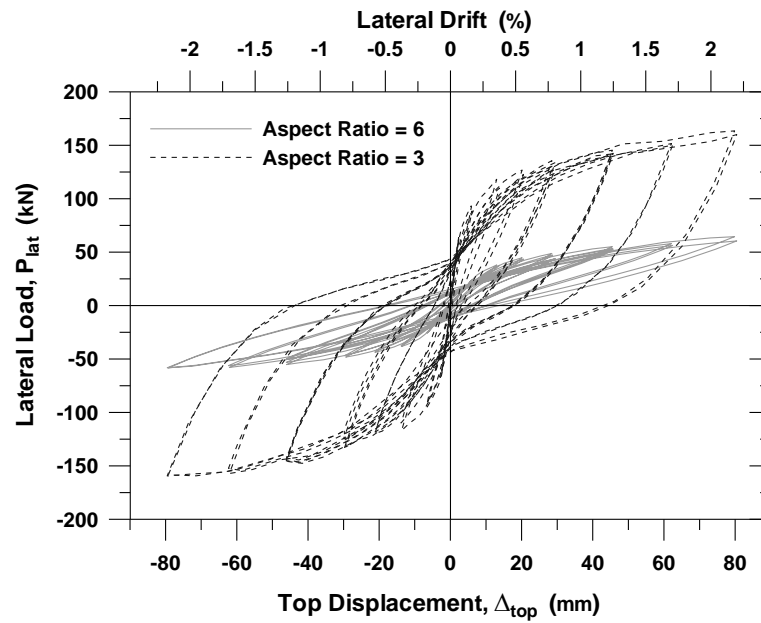


Figure 4.30. Analytical lateral load vs. top displacement responses for different wall aspect ratios.

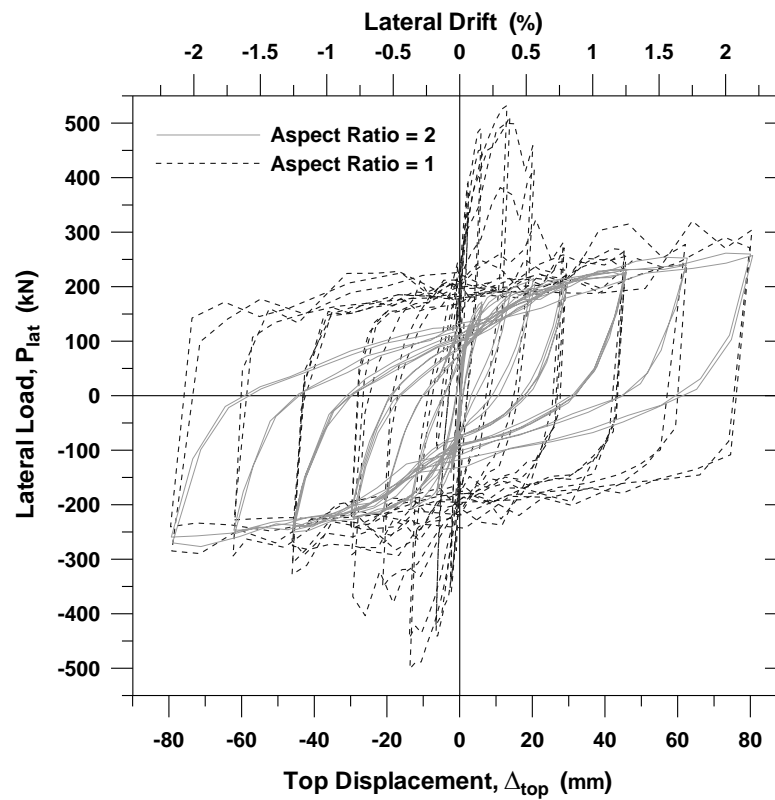


Figure 4.31. Analytical lateral load vs. top displacement responses for different wall aspect ratios.

Another sensitivity study of the model results was performed by changing the axial load level applied on the wall. As depicted in Figure 4.32, changing the axial load on the wall value from the original value of 378 kN to values of 179 kN and 756 kN obviously influences the analytical lateral load vs. displacement response of the wall. Larger axial load levels result in increased predictions for the lateral load capacity and the lateral stiffness of the wall, as expected for RC walls and columns designed to yield in flexure. The analytical model clearly incorporates the significant influence of axial load on the response predictions.

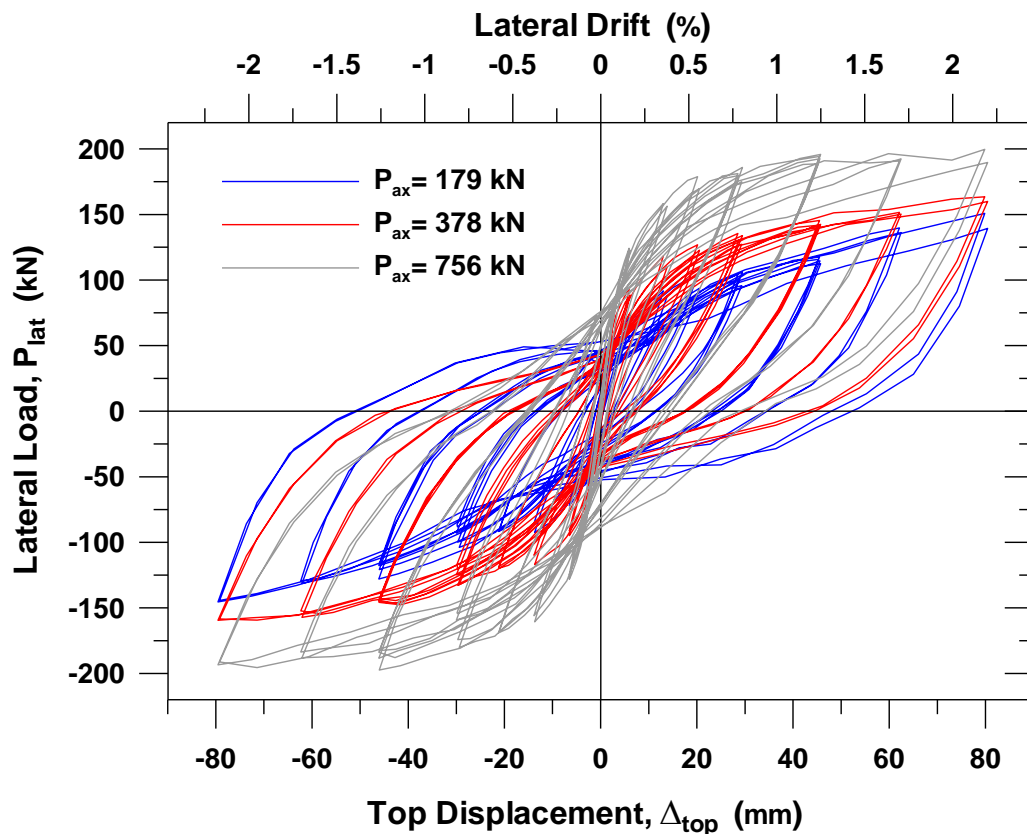


Figure 4.32. Analytical lateral load vs. top displacement responses for different axial load levels.

The last sensitivity study conducted in this study is reduction of the web reinforcement ratio of the wall, from the original value of 0.0033 to a superficial value of 0.001, which is below minimum code requirements. Reducing the web reinforcement ratio in a wall decreases its design shear strength. Therefore, the aim of this parametric study is

to observe the change in the lateral load vs. displacement response predicted by the analytical model, as well as the amount of nonlinear shear deformations developing in the wall model, when the shear capacity of the wall is reduced. Figure 4.33 shows the influence of decreasing the web reinforcement ratio on the lateral load vs. displacement response of the wall, whereas Figures 4.34 and 4.35 illustrate the effects of reduced web reinforcement to the amount of nonlinear shear deformations developing along the first story and second stories of the wall, respectively. As depicted in the figures, decreasing the web reinforcement ratio of the wall results in a reduced lateral load capacity prediction for the wall, and a larger maximum shear deformation prediction. Therefore, the analytical model successfully considers the influence of the amount of wall shear reinforcement on the global response of the wall, as well as the magnitude of nonlinear shear deformations developing in the wall.

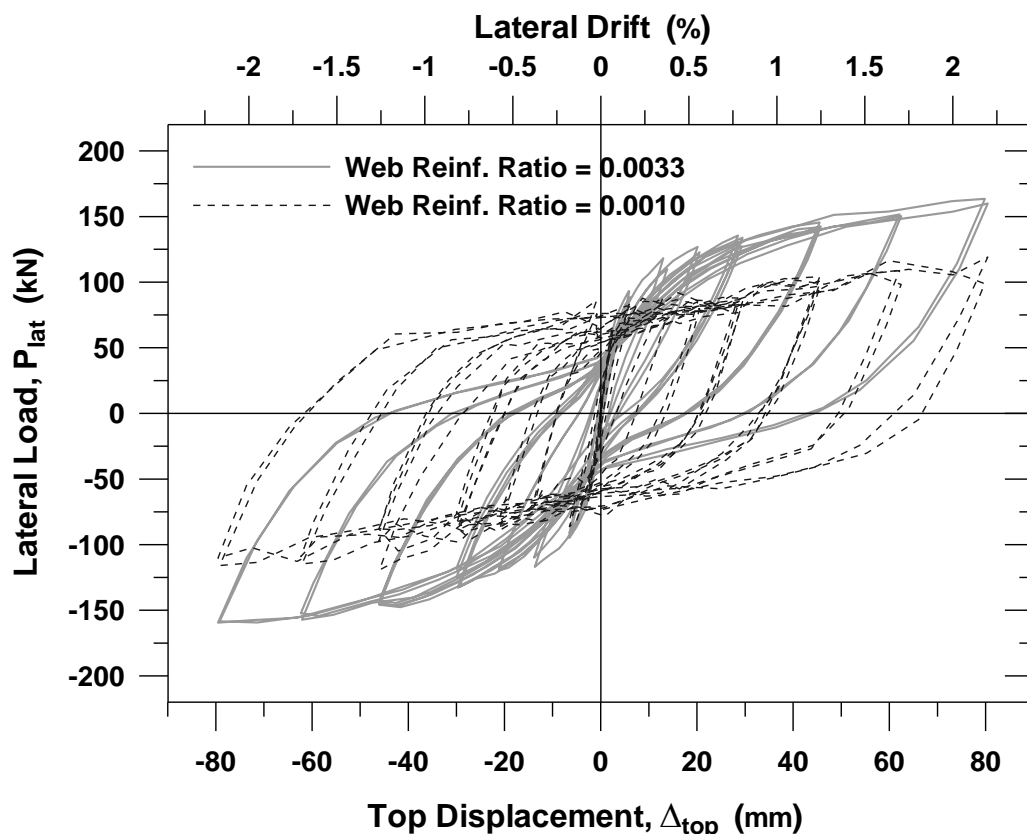


Figure 4.33. Analytical lateral load vs. top displacement responses for different web reinforcement ratios.

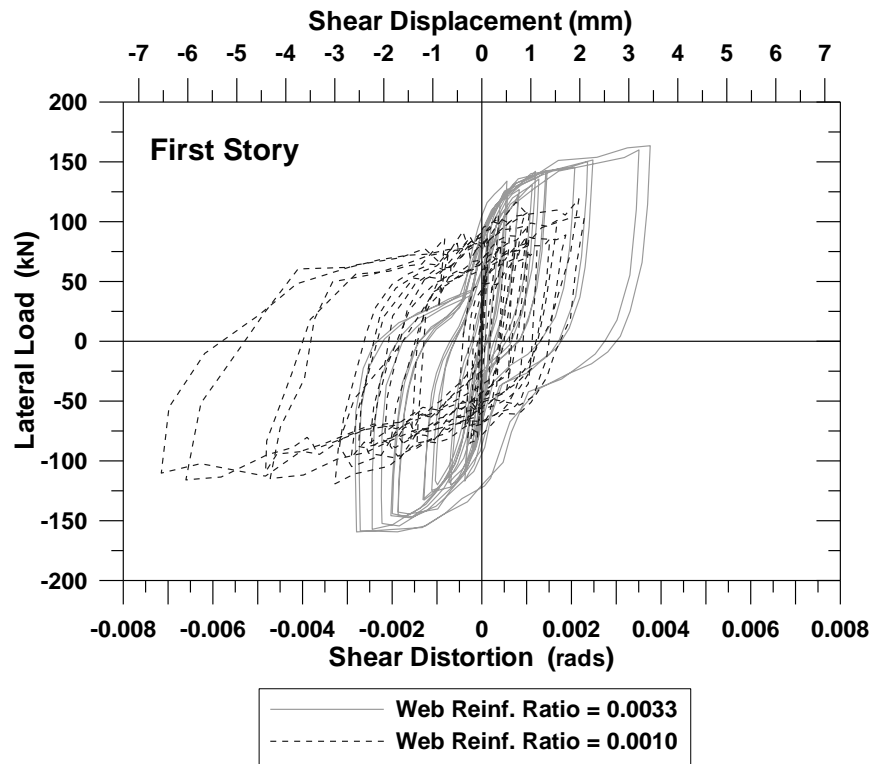


Figure 4.34. Effect of web reinforcement ratio to shear deformations along first story.

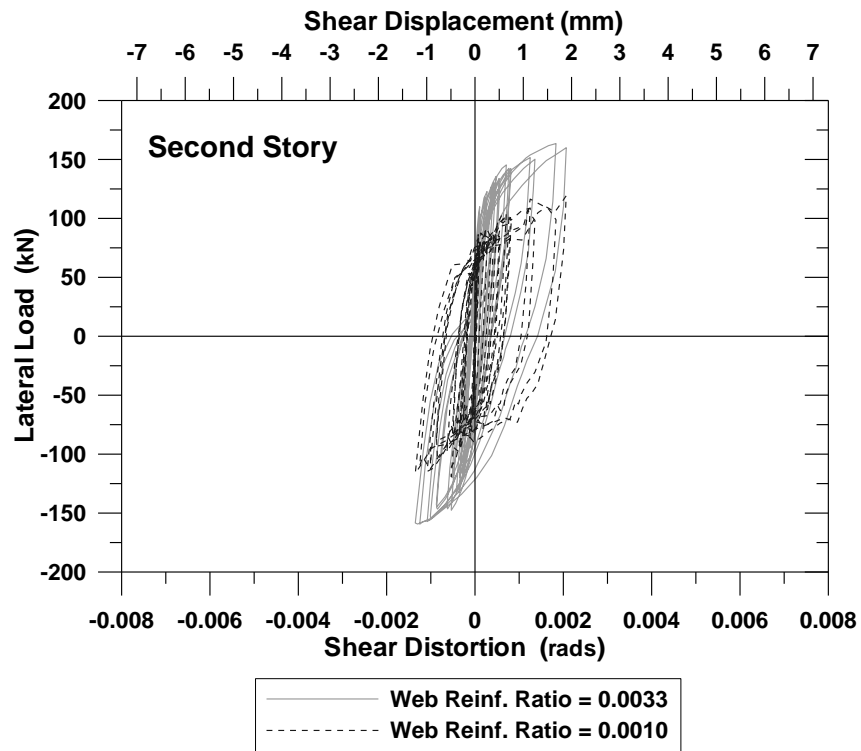


Figure 4.35. Effect of web reinforcement ratio to shear deformations along second story.

4.5. Discussion of Results

This chapter covered the description of the experimental study conducted on wall specimen RW2, geometric and material calibration of the proposed model for the wall specimen, and comparison of analytical and experimental results for the specimen at various response levels. Parametric sensitivity studies performed using the wall model were also presented in this chapter.

Based on comparison of the experimentally-measured results and model predictions, the proposed finite element modeling approach, incorporating the fixed-strut-angle panel model, can be deemed to represent the nonlinear hysteretic behavior of relatively slender RC walls reasonably well. The analytical model demonstrates reasonable levels of accuracy in predicting both the global response and local deformation characteristics of the wall specimen investigated. Average strain profiles along the length of the wall are mostly well represented, and tensile strains are well predicted, although compressive strain predictions are subject to improvement. Contrary to commonly-applied fiber models, the proposed finite element model formulation does not enforce the plain-sections-remain-plane condition along the length of the wall, which was found to be consistent with the experimentally-measured strain profiles. Another advantage of the proposed finite element model over a fiber model is that nonlinear shear deformations and coupling of nonlinear shear and flexural responses can be simulated by the proposed model, even for a slender wall designed to yield in flexure before reaching shear capacity. Nonlinear shear response predictions of the model can be improved upon incorporating better constitutive relationships representing the shear transfer mechanism across cracks.

Results of the parametric sensitivity studies conducted within the scope of this study showed that the proposed analytical model is sensitive to variation in important geometric and material characteristics of a wall. Increasing the number of model elements along wall height improves the model predictions for average strains in concrete, although not as influential on the lateral load vs. displacement response of a wall. The model capable of simulating different (flexural vs. shear) behavior modes based on the wall aspect ratio, which also influences the amount of shear deformations. Change in the axial load level directly influences the lateral load capacity and lateral stiffness predictions of the model,

which is a well-known behavioral aspect of RC members. The analytical model results are also sensitive to the web reinforcement ratio of a wall, which significantly influences the lateral load capacity and nonlinear shear deformation predictions of the model. Overall, results of the sensitivity studies indicate that the analytical model predictions are consistent, both mechanically and behaviorally.

5. SUMMARY AND CONCLUSIONS

5.1. Overview

A nonlinear finite element model for RC walls, incorporating a fixed-strut-angle constitutive panel formulation, was developed in this thesis. The aim was to simulate the nonlinear hysteretic response of RC structural walls under reversed-cyclic in-plane loading conditions. An overview of the flexural and shear-flexure interaction modeling approaches for RC walls, constitutive modeling methodologies for RC panels, and experimental studies on RC walls in the literature was provided. A new finite element modeling approach was then proposed for improved response prediction of RC walls.

The constitutive Fixed-Strut-Angle Panel model developed by Ulugtekin (2010), was implemented into the FEM formulation proposed in this thesis. Formulation and assembly of the proposed FEM model, which is the baseline computational aspect of this study, was described in detail. Generation of local stiffness matrices and internal force vectors, and their assembly for determination of the global stiffness matrix and internal force vector of the model were illustrated. Implementation of support restraints at the wall base level and the rigid body constraint at the top of the wall were also described.

After formulation of proposed FEM was completed, a drift-controlled nonlinear analysis solution strategy was incorporated for conducting hysteretic lateral load analyses using the analytical model. The model was experimentally calibrated and validated against cyclic test results reported by Thomsen and Wallace (1995) on a relatively-slender rectangular wall specimen designed to yield in flexure. Comparison of the response predictions of analytical model and the experimentally-obtained results were made at various response levels and various locations on the wall where measurements had been recorded. In order to demonstrate the sensitivity of the analytical model results to important parameters, parametric sensitivity studies were also carried out and consistency of the model results was evaluated.

5.2. Conclusions

The following conclusions can be drawn on the basis of the results obtained using the analytical model developed in this study:

- The proposed FEM demonstrated a reasonable level accuracy in predicting the nonlinear hysteretic response of RC structural walls under in-plane reversed-cyclic loading conditions. Accurate predictions were obtained for the experimentally-observed cyclic response characteristics of the wall investigated, including its lateral load capacity, stiffness degradation, hysteretic shape, plastic (residual) displacements, ductility, and pinching behavior. The model also provided reasonably accurate predictions of nonlinear flexural deformations developing in the plastic hinge region of the wall.
- Average concrete strain profiles along the base of the wall were reasonably predicted by the analytical model, especially in the tensile region of the wall cross-section. Unlike in fiber models, plane sections do not necessarily remain plane in the proposed FEM formulation, which was observed to be more consistent with the experimentally-measured strain profiles. Accurate predictions were also obtained with the model for the depth of the neutral axis. Compressive strains in concrete were underestimated; however, it was shown that compressive strain predictions of the model may be influenced by the number of model elements used along the height of the wall, possibly resulting in improved correlations between analytical and experimental results.
- An important result obtained from this study is related to simulation of nonlinear shear responses. The analytical model, with a new shear aggregate interlock model formulation proposed by this study, provided reasonable estimates for the nonlinear shear deformations developing along the first story height of the wall specimen, where nonlinear flexural deformations were also concentrated. The magnitude of the predicted nonlinear shear deformations decreased along the height of the wall, which was consistent with the experimental measurements. This demonstrated the model's capability of capturing nonlinear shear-flexure interaction effects in a wall. This is a

significant advantage of the finite element modeling approach proposed in this study, over conventional fiber models that do not consider coupling of shear and flexural responses.

- It was observed that changing the number of model elements along wall height did not significantly influence prediction of the model for the lateral load vs. top displacement response of the wall; however, increasing the number of model elements resulted in improved average concrete strain predictions at the base of the wall. On the other hand, the global load vs. displacement response prediction of the model was considerably sensitive to the axial load applied on the wall, which is expected for RC members designed to yield in flexure.
- It was also demonstrated that the proposed analytical model was capable of simulating different modes of behavior, based on the aspect ratio of a wall. Decreasing the wall aspect ratio changes the predicted response of the wall from the ductile flexural-dominated behavior that is typical of slender walls, into a brittle shear-dominated behavior expected for low-rise walls. As well, the model was shown to successfully represent the influence of the amount of web (shear) reinforcement on the global load vs. displacement response of a wall, as well as the magnitude of nonlinear shear deformations experienced by the wall.

5.3. Recommendations for Future Studies

The following recommendations can be made for future studies related with the scope of this thesis:

- Linear shape functions and Gauss integration points can be implemented into the formulation of the proposed finite element model for a more refined description of the strain and stress fields acting on the model elements.
- The simple constitutive shear aggregate relationship implemented in the model formulation can be improved to represent a better shear stress transfer mechanism

across the cracks. A constitutive model representing dowel action in reinforcing bars can also be incorporated in the formulation.

- The analytical model should also be validated experimentally for squat (low-rise) walls, the behavior of which is governed by nonlinear shear deformations.
- Future studies should also focus on implementation of the proposed modeling approach for structural walls having non-rectangular cross-section geometries (e.g., T-shaped or U-shaped walls).

REFERENCES

- ACI Committee 318, 2008, *Building Code Requirements for Structural Concrete (ACI - 318) and Commentary*, American Concrete Institute, Farmington Hills, MI.
- Belarbi, A. and T. C. Hsu, 1994, "Constitutive Laws of Concrete in Tension and Reinforcing Bars Stiffened By Concrete", *ACI Structural Journal*, Vol. 91, No. 4, pp. 465-474.
- Beyer, K., A. Dazio and M. J. N. Priestly, 2011, "Shear Deformations of Slender Reinforced Concrete Walls under Seismic Loading", *ACI Structural Journal*, Vol. 108, No. 2, pp. 167-177.
- Chang, G. A. and J. B. Mander, 1994, *Seismic Energy Based Fatigue Damage Analysis of Bridge Columns: Part I-Evaluation of Seismic Capacity*, NCEER Report No. 94-0006, National Center for Earthquake Engineering Research.
- Clarke, M. J. and G. J. Hancock, 1990, "A Study of Incremental-Iterative Strategies for Non-Linear Analyses", *International Journal for Numerical Methods in Engineering*, Vol. 29, pp. 1365-1391.
- Elmorsi, M., M. R. Kianush and W. K. Tso, 1998, "Nonlinear Analysis of Cyclically Loaded Reinforced Concrete Structures", *ACI Structural Journal*, Vol. 95, No. 6, pp. 725-739.
- Fajfar, P. and M. Fischinger, 1990, "Mathematical Modeling of RC Structural Walls for Nonlinear Seismic Analysis", *Proceedings, European Conference on Structural Dynamics*, Vol. 2, Bochum, Germany, pp. 471-478.

- Filippou, F. C., E. G. Popov and V. V. Bertero, 1983, *Effects of Bond Deterioration on Hysteretic Behavior of Reinforced Concrete Joints*, EERC Report No. UCB/EERC-83/19, University of California, Berkeley.
- Fischinger, M., K. Rejec and T. Isakovic, 2012, "Modeling Inelastic Shear Response of RC Walls", *Proceedings, 15th World Conference on Earthquake Engineering*, Lisbon, Portugal, No. 2120.
- Fischinger, M., T. Vidic and P. Fajfar, 1992, "Nonlinear Seismic Analysis of Structural Walls Using the Multiple-Vertical-Line-Element Model", in H. Krawinkler and P. Fajfar (eds.), *Nonlinear Seismic Analysis of RC Buildings*, Elsevier Science Publishers Ltd., London and New York, pp. 191-202.
- Fischinger, M, T. Vidic, J. Selih, P. Fajfar, H.Y. Zhang and F.B. Damjanic, 1990, "Validation of a Macroscopic Model for Cyclic Response Prediction of RC Walls", in N.B. Bicanic and H. Mang (eds.), *Computer Aided Analysis and Design of Concrete Structures*, Vol. 2, Pineridge Press, Swansea, pp. 1131-1142.
- Gérin, M. and P. Adebar, 2009, "Simple Rational Model for Reinforced Concrete Subjected to Seismic Shear", *ASCE Journal of Structural Engineering*, Vol. 135, No. 7, pp. 753-761.
- Gopalaratnman, V. S. and S. P. Shah, 1985, "Softening Response of Plain Concrete under Direct Tension", *Journal of the American Concrete Institute*, Vol. 82, No. 3, pp. 310-323.
- Hsu, T. C., 1988, "Softened Truss Model Theory for Shear and Torsion", *ACI Structural Journal*, Vol. 85, No. 6, pp. 624-635.
- Hsu, T. C. and R. H. Zhu, 2002, "Softened Membrane Model for Reinforced Concrete Elements in Shear", *ACI Structural Journal*, Vol. 99, No. 4, pp. 460-469.

- Kabeyasawa, T., 1997, "Design of RC Shear Walls in Hybrid Wall System", *Proceedings, The Fourth Joint Technical Coordinating Committee, U.S.-Japan Cooperative Seismic Research on Composite and Hybrid Structures*, Monterey.
- Kabeyasawa, T., H. Shiohara, S. Otani and H. Aoyama, 1983, "Analysis of the Full-Scale Seven-Story Reinforced Concrete Test Structure", *Journal of the Faculty of Engineering*, The University of Tokyo (B), Vol. 37, No. 2, pp. 431-478.
- Kolozvari, K., T. Tran, J. W. Wallace and K. Orakcal, 2012, "Modeling of Cyclic Shear-Flexure Interaction in Reinforced Concrete Structural Walls", *Proceedings, 15th World Conference on Earthquake Engineering*, Lisbon, Portugal, No. 2471.
- Mander, J. B., M. J. N Priestley and R. Park, 1988, "Theoretical Stress-Strain Model for Confined Concrete", *ASCE Journal of Structural Engineering*, Vol. 114, No. 8, pp. 1804-1826.
- Mansour, M. Y., T. C. Hsu and J.Y. Lee, 2002, "Pinching Effect in Hysteretic Loops of R/C Shear Elements", *ACI Special Publications*, Vol. 205, pp. 293-321.
- Mansour, M. Y. and T. C. Hsu, 2005, "Behavior of Reinforced Concrete Elements under Cyclic Shear", *ASCE Journal of Structural Engineering*, Vol. 131, No. 1, pp. 44-53.
- Massone, L. M., 2006, *Analytical and Experimental with Shear - Flexure Interaction in RC Walls*, Ph.D. Thesis, University of California.
- Massone, L. M., and J. W. Wallace, 2009, *RC Wall Shear-Flexure Interaction: Analytical and Experimental Responses*, UCLA-SGEL-2009/2, Structural & Geotechnical Engineering Laboratory, Department of Civil & Environmental Engineering, University of California-Los Angeles, Los Angeles, CA.
- Matlab v.7.6.0.324 (R2008a), 2008, The Math-Works, Inc., Massachusetts USA.
- Mau, S. T. and T. C. Hsu, 1986, "Shear Design and Analysis of Low-Rise Structural Walls", *ACI Structural Journal*, Vol. 83, No. 2, pp. 306-315.

- Menegotto, M. and E. Pinto, 1973, "Method of Analysis for Cyclically Loaded Reinforced Concrete Plane Frames Including Changes in Geometry and Non-Elastic Behavior of Elements under Combined Normal Force and Bending", *Proceedings, IABSE Symposium on Resistance and Ultimate Deformability of Structures Acted on by Well-Defined Repeated Loads*, Lisbon, Portugal.
- Mitchell, D. and M. P. Collins, 1974, "Diagonal Compression Field Theory – A Rational Model for Structural Concrete in Pure Torsion", *ACI Structural Journal*, Vol. 71, No. 8, pp. 396-408.
- Ohmori, N., T. Takahashi, N. Inoue, K. Kurihara and S. Watanabe, 1989, "Experimental Studies on Nonlinear Behaviors of Reinforced Concrete Panels Subjected to Cyclic in-plane Shear", *Trans AIJ*, Vol. 403, pp. 105-117.
- Orakcal, K., 2004, *Nonlinear Modeling and Analysis of Slender Reinforced Concrete Walls*, Ph.D. Thesis, University of California.
- Orakcal, K., D. Ulugteking and L. M. Massone, 2012, "Constitutive Modeling of Reinforced Concrete Panel Behavior under Cyclic Loading" *Proceedings, 15th World Conference on Earthquake Engineering*, Lisbon, Portugal, No. 3573.
- Orakcal, K., J. W. Wallace and J. P. Conte, 2004, "Flexural Modeling of Reinforced Concrete Walls – Model Attributes", *ACI Structural Journal*, Vol. 101, No. 5, pp. 688-699.
- Orakcal, K. and J. W. Wallace, 2006, "Flexural Modeling of Reinforced Concrete Walls – Model Calibration", *ACI Structural Journal*, Vol. 103, No. 2, pp. 196-206.
- Orakcal, K., L. M. Massone, and J. W. Wallace, 2006, *Analytical Modeling of Reinforced Concrete Walls for Predicting Flexural and Coupled - Shear - Flexural Responses*, PEER Report No. EEC-9701568, Pacific Earthquake Engineering Research, Berkeley.

- Palermo, D. and F. J. Vecchio, 2003, "Compression Field Modeling of Reinforced Concrete Subjected to Reversed Loading: Formulation", *ACI Structural Journal*, Vol. 100, No. 5, pp. 616-625.
- Panagiotou, M., J. Restrepo, M. Schoettler and K. Geonwoo, 2011, "Nonlinear Cyclic Model for Reinforced Concrete Walls", *ACI Structural and Materials Journal*, Vol. 109, No. 2, pp. 205-214.
- Pang, D. and T. C. Hsu, 1995, "Behavior of Reinforced Concrete Membrane Elements in Shear", *ACI Structural Journal*, Vol. 92, No. 6, pp. 665-677.
- Pang, D. and T. C. Hsu, 1996, "Fixed Angle Softened Truss Model for Reinforced Concrete", *ACI Structural Journal*, Vol. 93, No. 2, pp. 197-207.
- Petrangeli, M., P. E. Pinto and V. Ciampi, 1999, "Fiber Element for Cyclic Bending and Shear of RC Structures. I: Theory", *Journal of Engineering Mechanics*, ASCE, Vol. 125, No. 9, pp. 994-1001.
- Saatçioğlu, M. and S. Razvi, 1992, "Strength and Ductility of Confined Concrete", *ASCE Journal of Structural Engineering*, Vol. 118, No. 6, pp. 1590-1607.
- Standards, Turkey, 2007, *Specification for Buildings to be Built in Seismic Zones*, Ministry of Public Works and Settlement Government of Republic of Turkey, Turkey.
- Stevens, N. J., 1987, *Analytical Modeling of Reinforced Concrete Subjected to Monotonic and Reversed Loadings*, Ph.D. Thesis, University of Toronto.
- Stevens, N. J., M. Uzumeri and M.P. Collins, 1991, "Reinforced concrete subjected to reversed cyclic shear-Experiments and constitutive model", *ACI Structural Journal*, Vol. 88, No. 2, pp. 135-146.
- Thomsen, J. H. and J. W. Wallace, 1995, *Displacement-Based Design of Reinforced Concrete Structural Walls: An Experimental Investigation of Walls with Rectangular*

- and T-Shaped Cross-Sections*, Report No. CU/CEE-95/06, Department of Civil Engineering, Clarkson University, Postdam, New York.
- Tran, T. A. and J. W. Wallace, 2012, “Experimental Study of Nonlinear Flexural and Shear Deformations of Reinforced Concrete Structural Walls”, *Proceedings, 15th World Conference on Earthquake Engineering*, Lisbon, Portugal, No. 3913.
- Ulugtekin, D., 2010, *Analytical Modeling of Reinforced Concrete Panel Elements under Reversed Cyclic Loadings*, MS. Thesis, Boğaziçi University.
- Vecchio F. J., 2000, “Disturbed Stress Field Model for Reinforced Concrete: Formulation”, *ASCE Journal of Structural Engineering*, Vol. 126, No. 9, pp. 1070-1077.
- Vecchio, F. J. and M. P. Collins, 1986, “The Modified Compression-Field Theory for Reinforced Concrete Elements Subjected to Shear”, *ACI Structural Journal*, Vol. 83, No. 2, pp. 219-231.
- Vecchio, F. J. and M. P. Collins, 1993, “Compression Response of Cracked Reinforced Concrete”, *ASCE Journal of Structural Engineering*, Vol. 83, No. 2, pp. 219-231.
- Vulcano, A., V. V. Bertero and V. Colotti, 1988, “Analytical Modeling of RC Structural Walls”, *Proceedings, 9th World Conference on Earthquake Engineering*, Vol. 6, Tokyo-Kyoto, Japan, pp. 41-46.
- Yankelevsky, D. Z. and H. W. Reinhardt, 1987, “Response of Plain Concrete to Cyclic Tension”, *ACI Materials Journal*, Vol. 84, No. 5, pp. 365-373.
- Zienkiewicz, O. C. and R. L. Taylor, 2000, *The Finite Element Method*, 5th Edition, Butterworth Heineman, London.